FRICTIONAL AND VIBRATIONAL PROPERTIES OF NANOSTRUCTURES

A DISSERTATION SUBMITTED TO
MATERIALS SCIENCE AND NANOTECHNOLOGY PROGRAM
OF THE GRADUATE SCHOOL OF ENGINEERING AND SCIENCE
OF BILKENT UNIVERSITY
IN PARTIAL FULFILLMENT OF THE REQUIREMENTS
FOR THE DEGREE OF
DOCTOR OF PHILOSOPHY

By
Seymur Cahangirov
April, 2012

I certify that I have read this thesis and that in my opinion it is fully adequate, in scope and in quality, as a dissertation for the degree of doctor of philosophy.

Prof. Dr. Salim Çıracı (Advisor)

I certify that I have read this thesis and that in my opinion it is fully adequate, in scope and in quality, as a dissertation for the degree of doctor of philosophy.

Prof. Dr. Atilla Erçelebi

I certify that I have read this thesis and that in my opinion it is fully adequate, in scope and in quality, as a dissertation for the degree of doctor of philosophy.

Assoc. Prof. Dr. Özgür Oktel

I certify that I have read this thesis and that in my opinion it is fully adequate, in scope and in quality, as a dissertation for the degree of doctor of philosophy.

Prof. Dr. Macit Özenbaş

I certify that I have read this thesis and that in my opinion it is fully adequate, in scope and in quality, as a dissertation for the degree of doctor of philosophy.

Assoc. Prof. Dr. Mehmet Bayındır

Approved for the Graduate School of Engineering and Science:

Prof. Dr. Levent Onural
Director of the Graduate School

ABSTRACT

FRICTIONAL AND VIBRATIONAL PROPERTIES OF NANOSTRUCTURES

Seymur Cahangirov
Ph.D.in Materials Science and Nanotechnology Program
Supervisor: Prof. Dr. Salim Çıracı
April, 2012

Frictional and vibrational properties of low-dimensional nanostructures have been investigated using the state-of-the-art ab-initio calculations.

Stringent test of stability based on calculation of phonon dispersions have been performed for various materials having important potential applications in nanoscience and nanotechnology. Silicene, a counterpart of graphene composed of silicon atoms, is one of such materials with its suitability to well established silicon technology together with eccentric electronic structure due to its honeycomb symmetry. Vibrational spectrum of silicene is found to be exempt from imaginary frequencies upon the puckering of atoms in adjacent sublattices while preserving the symmetry necessary for occurrence of massless Dirac Fermions. Analyses of vibrational properties of silicene nanoribbons and carbon atomic chains revealed new interesting physics like fourth acoustical mode and long-ranged interactions due to Friedel oscillations.

Basic concepts of friction science like dissipation phenomena, adiabatic and sudden processes together with several simple models of friction have been summarized. A new method for calculation of corrugation potential between layered lubricants under constant loading pressure is introduced. Transition from stick-slip to continuous sliding regime is quantified through definition of frictional figure of merit for layered lubricants. Using this measure tungsten oxide is proposed as an oxidation resistant material which can outperform molybdenum disulfide as a superlubricant. It was found that, the corrugation strengths of graphene layers sandwiched between Ni slabs decrease as the number of layers increase.

Keywords: phonon, stability, silicene, friction, dissipation, sudden process.

ÖZET

NANOMALZEMELERİN SÜRTÜNME VE TİTREŞİMSEL ÖZELLİKLERİ

Seymur Cahangirov
Malzeme Bilimi ve Nanoteknoloji, Ph.D.
Tez Yöneticisi: Prof. Dr. Salim Çıracı
Nisan, 2012

Düşük boyutlu nanomalzemelerin sürtünme ve titreşimsel özellikleri ilk prensiplere dayanan en gelişmiş hesaplama yöntemleriyle incelendi.

Fonon eğrilerinin hesaplanmasıyla nanobilim ve nanoteknolojide önemli uygulama potansiyeli taşıyan malzemelerin kararlılıkları test edildi. Bunlardan birisi grafin'in silisyum atomlarından oluşan analoğu olan silisen'dir. Silisen, günümüzün silikon teknolojisine uyumunun yanında, sahip olduğu eksantrik elektronik yapısıyla da önem taşımaktadır. Silisen'deki atomlar yukarı ve aşağı hareket ederek titreşimsel spektrumu sanal frekanslardan arındırmakta ve bununla birlikte kütlesiz Dirac Fermiyon'larının oluşumu için gerekli olan simetriyi korumaktadır. Silisen nanoşeritlerin ve atomik karbon zincirlerin titreşimsel özelliklerinin incelenmesi sonucu dördüncü akustik mod ve Friedel salınımlarından kaynaklı uzun mesafeli etkileşim gibi yeni fiziksel olgular ortaya konmuştur.

Sürtünme biliminin temel kavramları olan enerji yayımı, adiyabatik ve ani olgularla birlikte sürtünmenin anlaşılması için kullanılan birkaç basit model özetlenmiştir. Katmanlı yağlama malzemelerinin sabit basınç altında korugasyon potansiyelinin hesaplanması için yeni bir yöntem geliştirilmiştir. Bu malzemelerin yapışma-kayma rejiminden düzenli kayma rejimine geçişi sürtünmesel başarım katsayısının tanımlanmasıyla kantitatif hale getirilmiştir. Bu ölçüt kullanılarak, oksitlenmeye dayanıklı olan tungsten oksit malzemesinin süperyağlama malzemesi olarak molibden disulfat malzemesinden daha yüksek performans gösterebileceği öne sürülmüştür. Nikel yüzeyleri arasına konulan grafin tabakaların sürtünmeyi düşürdüğü ve bu etkinin tabaka sayısıyla birlikte arttığı gözlemlenmiştir.

Anahtar sözcükler: fonon, kararlılık, silisen, sürtünme, enerji yayımı, ani olgular.

Acknowledgement

I am inexpressibly grateful to my supervisor Prof. Salim Çıracı for his guidance and support during my masters and doctorate studies. His foresighted vision always boosted the impact of our work by orders of magnitude. I feel proud for being a member of his condensed matter school which stands on a nearly half century experience of intensive research.

I would like to thank my instructors Prof. Cemal Yalabık, Assoc. Prof. Özgür Oktel, Assoc. Prof. Mehmet Bayındır and Assoc. Prof. Ömer Ilday for their perfect teaching and for being outstanding examples as scientists. In particular I would like to acknowledge fruitful discussions with Prof. Cemal Yalabık and Assoc. Prof. Özgür Oktel which were very helpful in development of this thesis. I would like to thank visiting instructors Prof. Chin-Yao Fong and Prof. Rolf Gerhardts for teaching us so much in a very short time.

I would like to thank Dr. Engin Durgun, Dr. Haldun Sevinçli, Dr. Ethem Aktürk and Dr. Hakan Gürel for their close guidance during their presence in the group. I am sincerely grateful to my groupmates Mehmet Topsakal, Can Ataca, Hasan Şahin and Ongun Özçelik for their friendship and outstanding collaborations. This thesis would certainly be lifeless without their colorful contributions.

I am grateful for the privilege of meeting Dr. Mecit Yaman who rejuvenated my mind. I would like to thank all members of UNAM family for providing a multidisciplinary research atmosphere and for joyful friendships.

I would like to thank my mother, father, sister, brother and my best friend Esat Çetin Musabeyli for always being there for me.

This thesis is dedicated to my beloved wife Naide. There is no way to thank her for the love and care she has provided all these years for me and our little bundle of joy, Alim.

Contents

List of Figures

List of Tables

Chapter 1

Introduction

This thesis is based on three breakthroughs in physics. The first one is the formulation of the Density Functional Theory (DFT) by pioneering works of Walter Kohn and his collaborators in 1965.[1, 2] This theory provides a rigorous framework for calculation of material properties from first-principles. In this thesis, most of the calculations are performed using DFT.

The second breakthrough is the synthesis of graphene, the first two-dimensional material, by Andre Geim and Konstantin Novoselov in 2004.[3] Besides eccentric properties of graphene, like its electrons behaving as massless Dirac Fermions,[4] this was the first realization of a truly two-dimensional material. This thesis is mainly investigating the frictional and vibrational properties of two-dimensional honeycomb structures like graphene.

The third breakthrough is the invention of the scanning tunnelling microscope by Gerd Binnig and Heinrich Rohrer in 1981,[5] which can be considered as the predecessor of the atomic and friction force microscopes.[6] Having a resolution on the atomic scale, these microscopes boosted the development of the emerging field of nanoscience and nanotechnology. It had impact in most fields of physics including the science of friction and dissipation which is the main topic of this thesis.

All these breakthroughs won the Nobel Prize and preserve their importance in the nowadays research. In the forthcoming sections we present a brief information about these breakthroughs and our contributions in the field based on them.

1.1 Density Functional Theory

In 1926, Schrödinger published his pioneering paper which included his famous equation marking the beginning of wave mechanics.[7] Shortly after Schrödinger‘s equation for electronic wave function, Dirac declared that chemistry had come to an end since all its content was entirely contained in that powerful equation. In principle, all information about the system can be extracted by solving the many-body Schrödinger equation;

$$H\Psi_i(\mathbf{r},\mathbf{R}) = E_i\Psi_i(\mathbf{r},\mathbf{R}) \tag{1.1}$$

Unfortunately in almost all cases except for the simple systems like He or H, this equation was too complex to allow a solution. The first approximation to this kind of systems is to decouple the motion of electrons and nuclei. This can be done by considering the fact that mass of an ion is at least thousand times higher than mass of an electron while its velocity is thousand times lower. Due to this difference, electrons can arrange themselves according to ionic coordinates before they are changed. In Born-Oppenheimer approximation one can solve the electronic problem by assuming fixed ionic coordinates and then move ions according to the forces due to electronic and ionic distribution, as shown in Fig. 1.1. This leaves us with an electronic problem which is still very hard to solve.

In 1928, first approximation method to solve the electronic problem was proposed by Hartree.[8] It postulates that many-electron wave function can be written as product of one-electron wave functions each of which satisfies one-particle Schrödinger equation in an effective potential. In Hartree method, the effective potential itself is determined by one-electron wave functions and one has to perform iterative calculations until a self-consistent solution minimizing the total energy is reached. This method was then improved to include Pauli exclusion

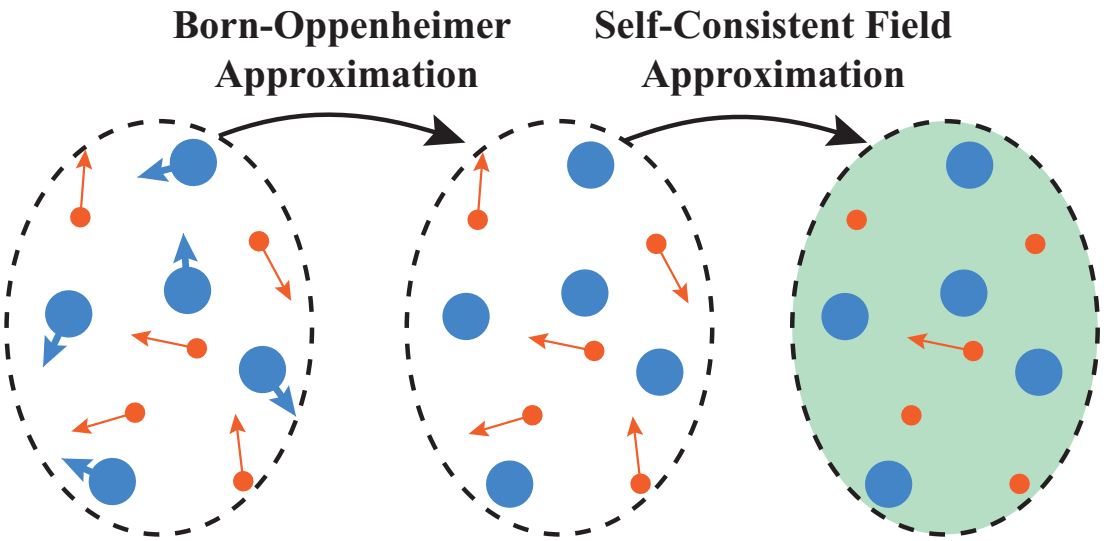

Figure 1.1: Born-Oppenheimer and Self-Consistent Field Approximations.

principle by writing the total wave function as Slater determinants.[9] The improved version is called the Hartree-Fock method and it includes the exchange terms in an exact manner while the many-body correlation terms are completely absent.[10] These kind of methods are in general called self-consistent field approximations where an electron is assumed to move under an external interaction field generated by other electrons and ions, as in Fig 1.1. Shortly after Schrödinger's paper, another method was developed by Thomas and Fermi.[11, 12] In Thomas-Fermi approximation the full electron density was taken as the fundamental variable of the many-body problem without referring to one-electron orbitals. This approximation did not include exchange-correlation terms and failed to sustain bound states but it set up a basis for Density Functional Theory (DFT).

In 1964, Hohenberg and Kohn introduced the foundation of DFT.[1] In this work they have shown that the full ground state electron density determines all information about the ground state properties of an electronic system. They also state that the total energy of the system can be minimized according to the total electron density instead of electronic wave-functions. This was very important because it is much simpler to deal with total electron density rather than

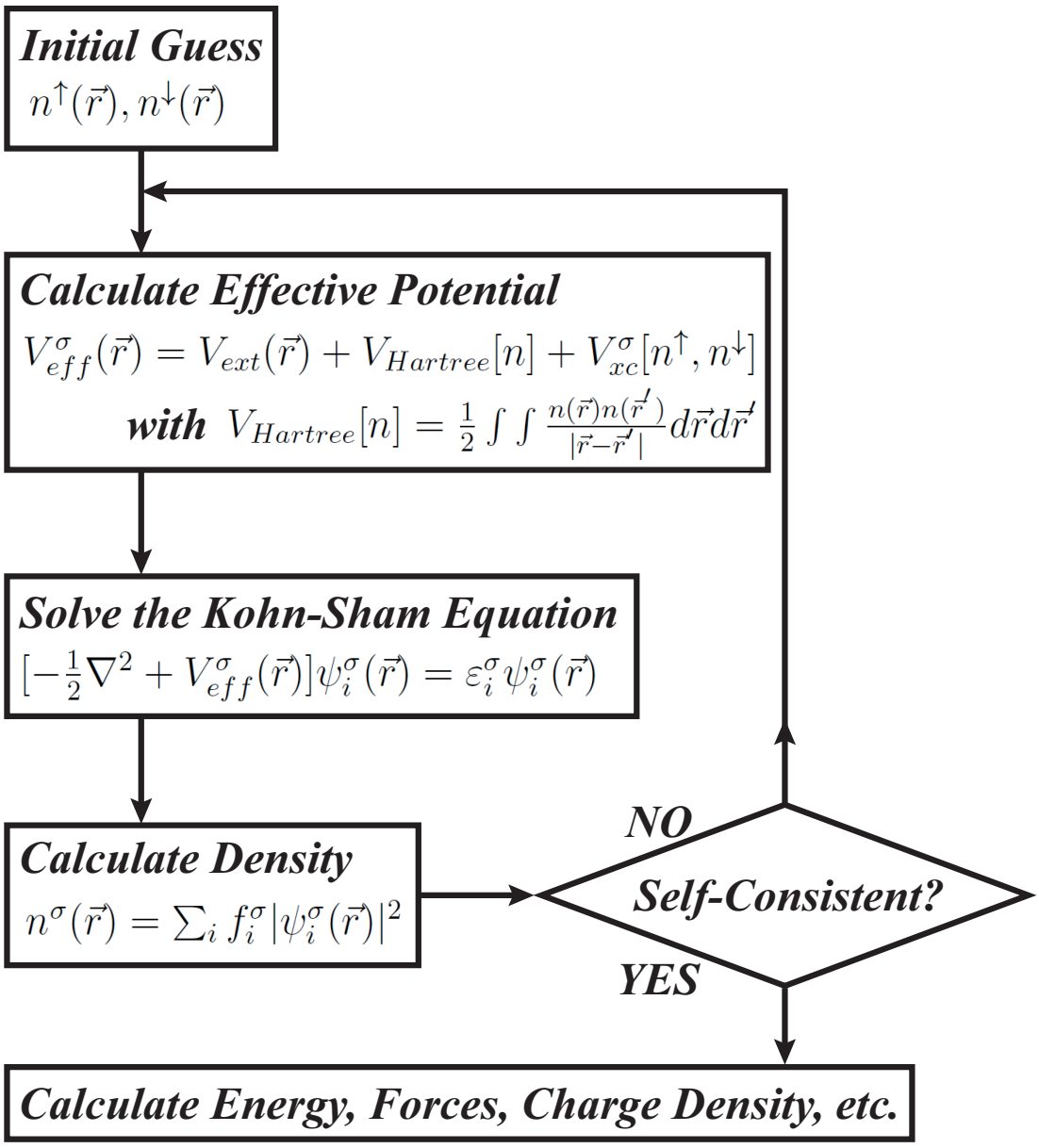

Figure 1.2: The scheme for self-consistent DFT calculation.

full electronic wave-function. In 1965, Kohn and Sham proposed the idea of replacing the kinetic energy of the interacting electrons with that of an equivalent non-interacting system.[2] This lead to construction of a mathematical object called Kohn-Sham orbitals which minimize the kinetic energy under fixed density constraint. The remaining exchange and correlation terms can be also expressed as a functional of the full electron density, but the exact representation is still not derived. There are two main approximation dealing with these terms. The local density approximation (LDA) and the generalized gradient approximation (GGA). The main idea of LDA is to consider the generally inhomogeneous electronic systems as locally homogeneous and then use the exchange correlation corresponding to the homogeneous electron gas.[13] LDA favors more homogeneous systems. It over-binds molecules and solids but the chemical trends are usually correct. GGA introduces the inhomogeneties of the density semi-locally, by expanding the exchange-correlation functional as a series in terms of the density and its gradients.[14] GGA improves binding energies, atomic energies, bond lengths and bond angles when compared to the ones obtained by LDA.

DFT calculations are performed self-consistently as shown in Fig 1.2. For a given configuration of ionic positions one starts with an initial guess of electron density. Then the effective potential corresponding to this density is calculated. The effective potential is then inserted into Kohn-Sham equations to calculate the Kohn-Sham orbitals. Sum of squares of these orbitals multiplied by the occupations gives the new electron density. Obtained new electron density is then compared with the electron density that is used in calculation of effective potential. According to Kohn-Sham ansatz the new and old electron densities should be equal. If their difference is below some acceptable value the self-consistency loop is stopped and one proceeds to the calculation of total energy, forces, charge densities and etc. If the difference is not in the acceptable range the loop is continued until the self-consistency is reached.

The most computationally expensive part of a self-consistent DFT calculation is solution of Kohn-Sham equations. Several numerical approximations are introduced here. To deal with the second order derivative in Kohn-Sham equations one can use the reciprocal space discretization.[15] To avoid the rapid oscillations of

wavefunction around the ionic singularities one can make use of pseudo-potentials or projector augmentized-wave approximations.[16, 17] Another approximation is expansion of wavefunctions in terms of basis sets which can be plane-waves, gaussians or atomic orbitals. In this thesis, we report DFT results obtained by VASP software which uses plane-waves as a basis set and requires use of periodic boundary condition.[18, 19]

1.2 The Rise of Graphene

Carbon is an element which has a central focus in both life and physical sciences. Due to its small core and four valence electrons it can form various types of bondings which result in materials with very different properties. By sp^3 hybridization C atoms form tetrahedral bonds which build up the diamond structure. In sp^2 hybridization which is slightly more energetic than sp^3, C atoms form graphite, fullerene, nanotubes and most of the organic molecules. It can also form sp type hybridization which forms carbon atomic chains. Despite the presence of zero-dimensional (0D) fullerene, one-dimensional (1D) nanotubes and three-dimensional (3D) diamond structures two-dimensional (2D) counterpart of carbon structures were absent until 2004.[3] In fact there was no 2D material synthesized and there were serious doubts about their stability.[36, 37] Synthesis of graphene, the first 2D honeycomb structure of C atoms, revolutionized the physics of 2D materials.

Graphene is the most stiff material due to its strong sp^2 bonds.[38] However, its most exciting properties like planar stability and dashing electronic structure is attained by its p_z orbitals. Graphene structure has high carrier concentration and low impurity scattering which makes it an excellent candidate for ballistic transport devices.[39] Due to the honeycomb symmetry of graphene, its p_z orbitals have a linear band crossing at the Fermi level which makes electrons act as Massless Dirac Fermions.[4, 40] In the vicinity of the Fermi level carriers obey the relativistic Dirac equation and move with a velocity $v_F = c/300 \sim 10^6$ m/s.[41] This properties result in possibility of observation of exciting physics like Klein

Paradox and half-integer Quantum Hall Effect.[4, 42, 43]

In our recent work we have shown that Si atoms arranged in a honeycomb lattice cannot remain in planar geometry like graphene but they gain stability via slight puckering.[44] However, this puckering does not break the symmetry required for the linear crossing of π bands and the electronic structure shows similar behavior as that of graphene. The band structure of 2D honeycomb structures of silicon and germanium, now called silicene and germanene, is presented in Chapter 2, where we also discuss the stability of these structures obtained by calculation of their phonon dispersions. Much recently, silicene was synthesized on silver surface and the Fermi velocity of its Dirac electrons was measured.[45]

We have also shown that other Group IV and binary compounds of Group III-V elements can form a stable 2D honeycomb structure.[46] We have found that these structures remain planar as graphene if one of the binary compounds is a member of the first row (i.e. either B, C or N), while the structure attains stability through puckering otherwise, as in case of silicene.

Quasi-1D counterparts of graphene, called graphene nanoribbons, were also synthesized.[47] Their width can reach down to few nanometers. One can build a ballistic transistor using graphene nanoribbons.[48] They have interesting electronic properties attributed to their edge structure. It was shown that graphene nanoribbons having zigzag shaped edges can behave as a half-metal upon application of an electric field.[49] Graphene nanoribbons having armchair shaped edged have an interesting family behavior in the variation of their band gap versus their width.[50]

We have shown that the family behavior is also present in armchair nanoribbons of silicene and germanium.[51] As in the case of armchair graphene nanoribbons, one can model their band structure in a nearest-neighbor tight-binding scheme of p_z orbitals. In Chapter 2, we also discuss the stability of armchair silicene nanoribbons.

1.3 The Renaissance of Friction

Friction is one of the oldest problems of physics.[20] Early works on the nature of frictional forces were done by giants of science widely known for their contributions in other fields like; the painter of Mona Lisa, Leonardo da Vinci; Charles-Augustin de Coulomb of the Coulomb's law of electrostatics; Leonhard Euler of the Euler's formula $e^{ix} = \cos x + i\sin x$ and others.[21, 22] It is no surprise that friction phenomena attracts so many polymaths from different fields, since here one has to engage complicated microscopic events in an elegant framework to account for generally simpler macroscopic behavior. The ultimate theory of friction involves quantum mechanical treatment of events in the atomic scale combined with statistical mechanics to account for the stochastic nature of the problem.

In early experimental works, the friction force was found to be nearly independent of the apparent area of contacts and sliding velocity. It was also found that, the friction force has a linear dependence on the applied loading force. Even though deviations from these results are rarely observed in everyday life the underlying physics is not at all obvious. In fact, there was no rigorous understanding of them until 1940s. Friction force was also found to depend on the time the surfaces remained in stationary contact (history of sliding) and ambient conditions like temperature, humidity, etc. A detailed historical review of early works on friction can be found elsewhere.[23] Here we would like to point out some important aspects of these works.

Until the work by Prandtl (1928) and Tomlinson (1929) it was not clear why in certain cases friction force had weak dependence on sliding velocity.[24, 25] In the case of a rigid object moving in a viscous fluid, Stokes' law dating back to 1851 established a drag force which was proportional to the velocity of the particle. Prandtl-Tomlinson model showed that when the sliding surfaces have high corrugation or low stiffness the relative motion enters in a stick-slip regime. Here the surfaces first cling to each other and when they reach some critical strain the stored elastic energy is released as rapid atomic movements. Their model shows that for a reasonable range of sliding velocities, friction force undergoes a

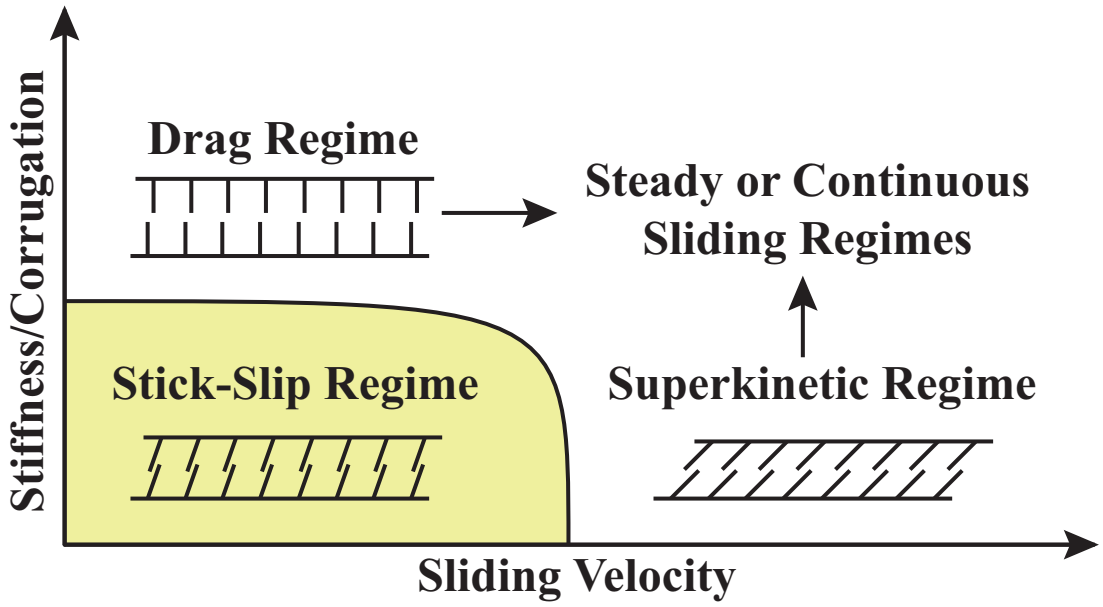

Figure 1.3: General dependence of friction regimes on sliding velocity and ratio of stiffness to the corrugation potential. In the drag regime, friction force is proportional to velocity while in the superkinetic regime it is inversely proportional. In the stick-slip regime friction force has weak dependence on sliding velocity. For each regime, a sketch of surface asperities is presented.

minor change. The details of this model is discussed in Chapter 4.

Another issue was to resolve why the friction force had minor dependence on surface area and why it was proportional to applied loading. In 1940, Bowden and Tabor resolved these issues by introducing the concepts of apparent and real area of contact.[26] They have shown that the microscopic asperities of the surface that were actually in a contact made up much smaller area, called real area of contact, compared to the are that was measured macroscopically or apparent area. They have also shown that the real area of contact was proportional to applied loading force and the friction force was proportional with real are of contact. Here the effect of increasing the loading force was not to increase the area of already present junction (which would lead to a nonlinear dependence of real area on loading force) but to increase the number of junctions.[27] This explained why the friction force was independent of apparent area and why it

was proportional to applied loading force.

In his book,[20] Persson ironically points out an infertile period in friction science from 1960 to 1987 in which surface scientists were attracted by simpler phenomena like adsorption of atoms and molecules on single crystal surfaces. However, one of such debates was resolved with a tool that would revolutionize many fields including the friction science. This debate was the reconstruction nature of Si(111) surface. Experiments were pointing on a (7x7) reconstruction which was very hard to analyse in detail by experimental and computational tools of that time. In 1983, Binnig *et al.* resolved this issue using the scanning tunneling microscope introduced by themselves.[5, 28] In 1986, Binnig *et al.* introduced atomic force microscope which was used in a first atomic scale friction experiment.[6]

The renaissance of friction and emergence of nanotribology was kindled in 1987, by the first experiment on the atomic scale friction.[29] In their seminal paper, Mate *et al.* used an atomic force microscope with a tungsten tip which was slid over a graphite surface.[30] They have shown that the friction force detected by the microscope had atomic-scale features like stick-slip with a periodicity of graphite lattice. They also were able to detect double-slips occurred during sliding of the tip. Results of this experimental work was then investigated in the context of Prandtl-Tomlinson model.[31] These works were followed by vast amount of experimental and theoretical papers on atomic scale friction but here we would like to mention only some of them.

Transition from stick-slip to continuous sliding in atomic scale friction was investigated by Socoliuc *et al.*, using friction force microscope.[32] They have shown that when the loading force is decreased below some critical value the stick-slip regime ends and the system enters in the ultralow friction regime. They give explanation to this transition using the Prandtl-Tomlinson model. Here the corrugation potential is proportional to applied loading and when the curvature of the corrugation potential falls below the stiffness of the tip, it starts to move without making any sudden jumps. Further details of this transition is presented in Chapter 4.

In our study, presented in Chapter 5, we have developed a method for calculation of intrinsic stiffness and corrugation potential between layered structures under constant loading pressure. We have combined the stiffness and the critical curvature derived from the corrugation potential in a single quantity called frictional figure of merit.[33] Analysing this quantity, which is a material property under certain loading pressure, we have shown that the oxidation resistant tungsten oxide structure can be better lubricant than the well established molybdenum disulfide structure.

Transition from stick-slip to steady sliding regime is also observed when sliding velocities exceed certain critical values. In this case the system enters in the super-kinetic regime where the friction force generally decreases when the sliding velocity is increased.[34] This kind of behavior is also observed in our simple model described in Chapter 4. Both of the mentioned transitions can be analysed by plotting a dynamical phase space of the system, as shown in Fig 1.3.[35] The nature of these transitions, like if they are continuous or discontinuous, is one of the fundamental problems of nowadays friction science.

1.4 Organization of the Thesis

This thesis is composed of two main parts. In the first part, stability and vibrational properties of various materials like 2D silicene, quasi-1D silicene nanoribbons and carbon atomic chains are discussed. This part is presented in Chapter 2. In the second part, frictional properties of layered lubricants are presented. Chapters 3 and 4 summarize crucial aspects of friction science like phononic and electronic dissipation, adiabatic and sudden processes, Prandtl-Tomlinson model, and etc. Discussions provided in these chapters are critical for understanding of Chapter 5 which contains our main contribution in the field. In Chapter 5, we introduce the concept of frictional figure of merit and predict the performance potential of new lubricant materials. In Chapter 6, we discuss potential corrugation of multilayer graphene structures. The concluding remarks are presented as an outlook in Chapter 7.

Chapter 2

Phonons and Stability

In this chapter, the basic concept of phonons and the methods for calculation of phonon dispersions is introduced. We also present our recent works, in which we use phonon spectra as stringent test of stability and predict the possibility of materials having interesting electronic properties. Phonon calculation presented here also reveal some interesting physics like fourth acoustical mode in quasi-1D nanoribbons and Friedel oscillations which give rise to long-ranged interactions in 1D atomic chains.

2.1 Introduction

Matter is composed of atoms vibrating around a certain equilibrium position determined by positions of neighboring atoms. This vibrations are resulted by restoring forces that atoms feel when they are displaced from their equilibrium position. This collective motion of atoms can be quantized into an entity which behaves as a particle called phonon. Phonons possess energy and momentum which can be measured, for example, by neutron scattering. Phonons behave as bosonic particles which obey the Bose-Einstein statistics. Observation of a single phonon is very challenging and was achieved only very recently.[52]

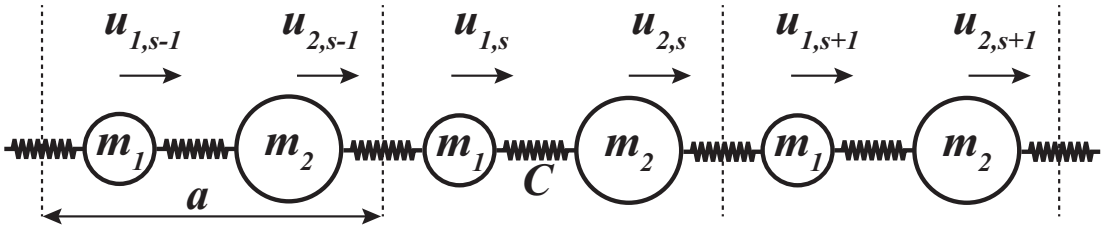

Figure 2.1: Diatom chain with harmonic interactions.

To determine phonon dispersion and phonon-phonon interaction cross-sections one has to know the variation of restoring force with displacement of each atom in a unitcell of a crystal.[53] In the following section we present a formalism for calculation of phonon dispersion in harmonic approximation where the magnitude of the restoring force is assumed to be proportional to the magnitude of displacement.

2.2 Dynamical Matrix Formulation

We start by a simple example of one-dimensional diatomic crystal with harmonic nearest neighbor interactions, as shown in Fig. 2.1.[54] Equations of motion for this system can be written as;

$$\begin{aligned} m_1 \ddot{u}_{1,s} &= C(u_{2,s-1} - u_{1,s}) + C(u_{2,s} - u_{1,s}) \\ m_2 \ddot{u}_{2,s} &= C(u_{1,s+1} - u_{2,s}) + C(u_{1,s} - u_{2,s}) \end{aligned} \tag{2.1}$$

these coupled differential equations have solutions of the form;

$$u_{i,s} = v_i \, e^{i\omega t + iska} \quad \text{with } i = \{1, 2\} \tag{2.2}$$

where v_i is the amplitude of vibration of i^{th} atom and k is the wave-vector. Inserting (2.2) into (2.1) leads to a matrix eigenvalue problem;

$$\begin{bmatrix} 2C/m_1 & C(1+e^{-ika})/m_1 \\ C(1+e^{ika})/m_2 & 2C/m_2 \end{bmatrix} \begin{bmatrix} v_1 \\ v_2 \end{bmatrix} = \omega^2 \begin{bmatrix} v_1 \\ v_2 \end{bmatrix} \tag{2.3}$$

which can be rewritten in a more symmetric way as;

$$\begin{bmatrix} 2C/\sqrt{m_1 m_1} & C(1+e^{-ika})/\sqrt{m_1 m_2} \\ C(1+e^{ika})/\sqrt{m_2 m_1} & 2C/\sqrt{m_2 m_2} \end{bmatrix} \begin{bmatrix} \sqrt{m_1}v_1 \\ \sqrt{m_2}v_2 \end{bmatrix} = \omega^2 \begin{bmatrix} \sqrt{m_1}v_1 \\ \sqrt{m_2}v_2 \end{bmatrix}. \tag{2.4}$$

Here the two by two matrix in the left hand side is called the Dynamical Matrix. Eigenvalues of Dynamical Matrix give dispersions of phonon branches in terms of $\omega(k)^2$. The number of phonon branches is equal to the degrees of freedom which is also the size of the Dynamical Matrix. In this simple case there are two phonon branches. One of these branches is acoustical and one is optical. In general, the number of acoustical branches equals to the number of possible invariant transformation. In the case of diatomic chain the system can be shifted along the axis and stay invariant. Frequencies of acoustical modes are zero at the center of the Brillouin zone, since there is no restoring force acting against an invariant transformation. In the light of equation (2.4), one can generalize the Dynamical Matrix to a 3D crystal with interaction which are not necessarily confined to nearest neighbors, as following;

$$D_{s\alpha,t\beta} = \frac{1}{\sqrt{m_s m_t}} \sum_{n,l} \Phi_{ns\alpha,lt\beta}\ e^{i\vec{k}\cdot(\vec{R}_{lt\beta}-\vec{R}_{ns\alpha})} \tag{2.5}$$

where $D_{s\alpha,t\beta}$ is dynamical matrix element due to the force in cartesian coordinate α felt by s^{th} atoms in the unitcells resulting from the movement of t^{th} atoms in the unitcells in cartesian coordinate β. In similar fashion, $\Phi_{ns\alpha,lt\beta}$ is the force constant which corresponds to the ratio of the felt force to the magnitude of the displacement, where indices n and l denote the unitcells. $\vec{R}_{ns\alpha}$ and $\vec{R}_{lt\beta}$ are position vectors while $\vec{k}$ is the wave-vector. The summation should be performed over all unitcells which possess finite interaction. Derivation of (2.4) from (2.5), which is left to the reader, can be very usefull for understanding the Dynamical Matrix formalism.

2.3 Small Displacement Method

In the following sections we present a recipe for performing phonon dispersion calculation using DFT combined with Dynamical Matrix formalism introduced

in the previous section. The idea is to derive the force constant matrix by displacing atoms in sufficiently large unitcells which include all interacting neighbors and calculate the resulting Hellmann-Feynman forces due to these displacements. Using the symmetry of the system one can reduce the number of displacements needed for this derivation. Throughout the work presented in this thesis we have used the freely available PHON program[55] for calculation of phononic properties from forces calculated by the widely used DFT software VASP.[56]

To obtain a reliable phonon spectra one needs to tune the calculation parameters accordingly. In this respect, we present phonon calculations of several important materials. Besides their interesting electronic properties, phonon analysis of these materials helps to explore interesting phenomena like stability of 2D silicene through puckering, forth acoustical mode in quasi-1D nanoribbons and long-ranged interaction in 1D carbon atomic chains.

2.4 Stability of Silicene

The unusual electronic properties of graphene, which is derived from its planar honeycomb structure leads to charge carriers resembling massless Dirac fermions.[4, 40] Recent synthesis of graphene has demonstrated that this truly two dimensional (2D) structure is stable and has introduced novel concepts.[3, 43, 57, 58, 59] Not only the fundamental properties of 2D graphene, but also interesting size and geometry dependent electronic and magnetic properties of their quasi 1D nanoribbons have been revealed.[47, 48, 49, 50] While the research interest on graphene and its ribbons is growing rapidly, one has started to question whether the other Group IV elements in Periodic Table, such as Si and Ge, have stable honeycomb structure. Even before the synthesis of isolated graphene, ab-initio studies based on the minimization of the total energy has revealed that a buckled honeycomb structure of Si can exists.[60, 61, 62]

In this section, based on the atomic structure optimization and phonon dispersion calculations we show that the low-buckled honeycomb structures of Si and

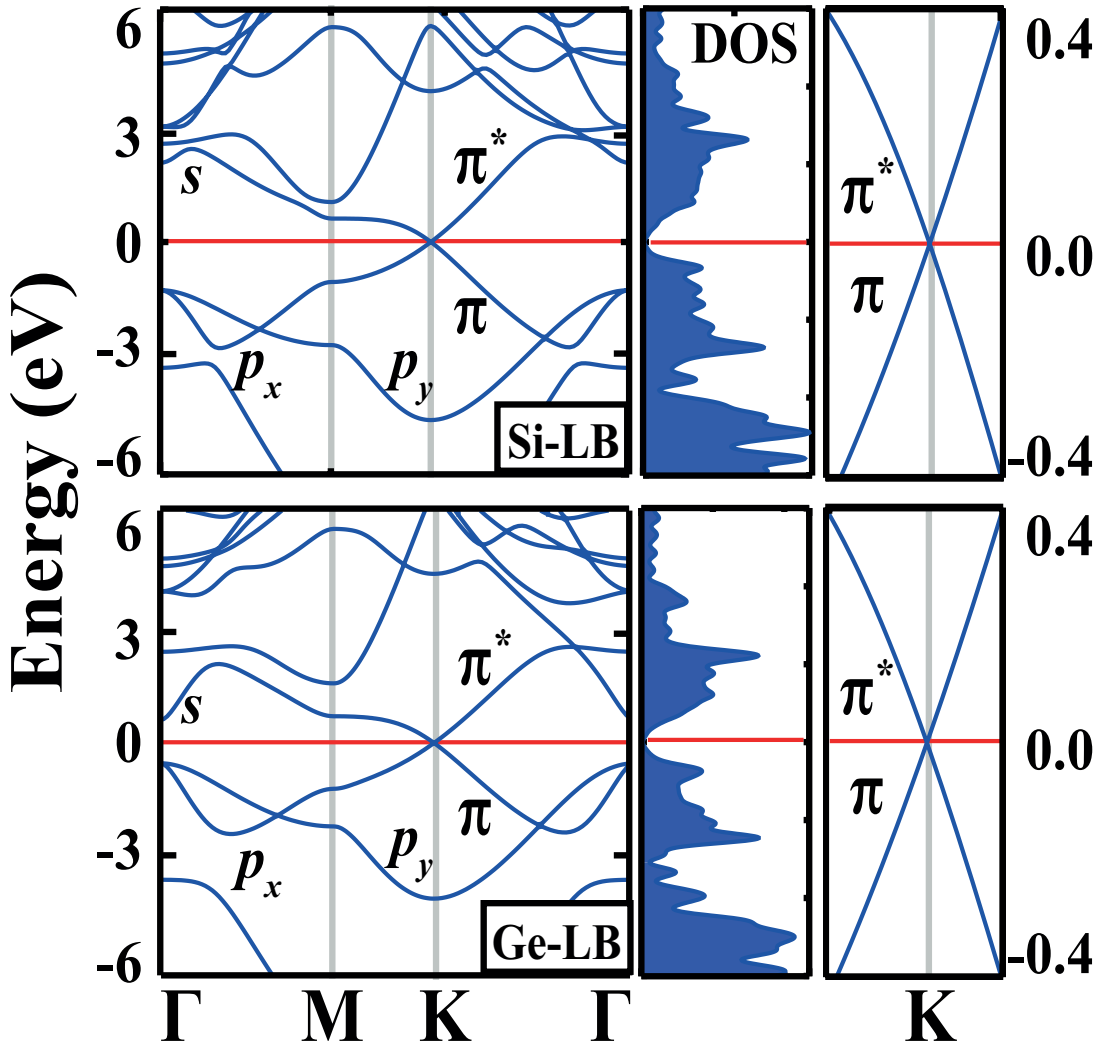

Figure 2.2: Energy band and density of states (DOS) diagrams of low-buckled (LB) 2D honeycomb structures Si and Ge. The crossing of the π and π^* bands at K- and K′-points of BZ is amplified to show that they are linear near the cross section point. Zero of energy is set at the Fermi level, E_F. Orbital character of bands are indicated.

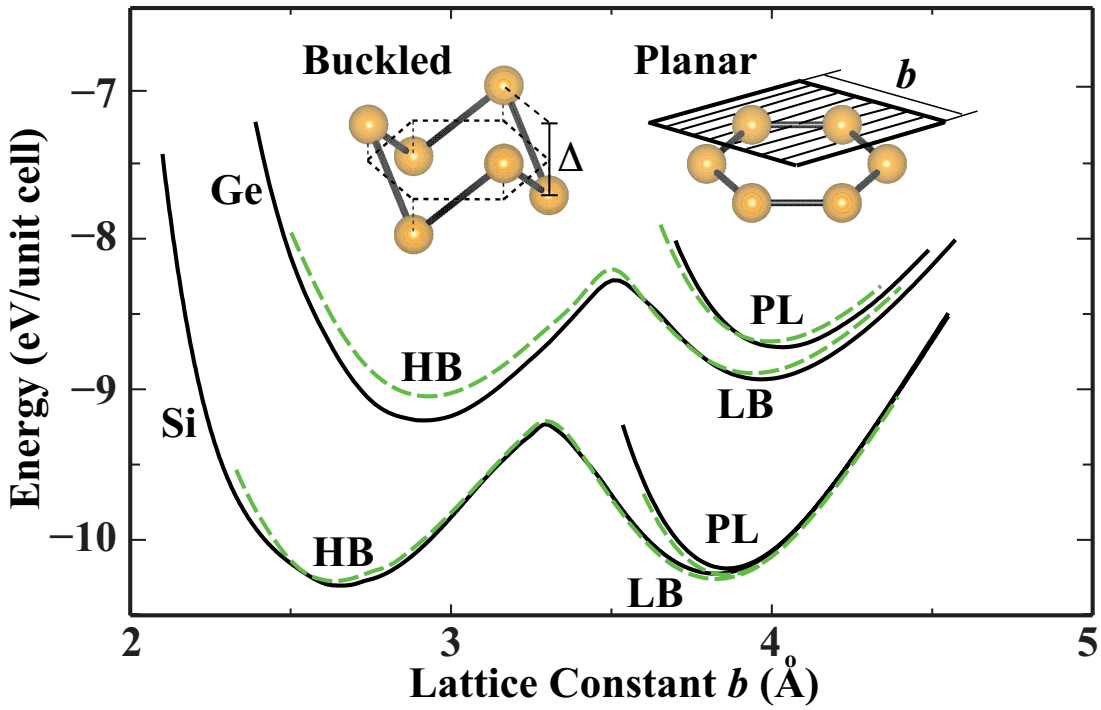

Figure 2.3: Energy versus hexagonal lattice constant of 2D Si and Ge are calculated for various honeycomb structures. Black (dark) and dashed green (dashed light) curves of energy are calculated by LDA using PAW potential and ultrasoft pseudopotentials, respectively. Planar and buckled geometries together with buckling distance Δ and lattice constant of the hexagonal primitive unit cell, b are shown by inset.

Ge are stable. Similar to graphene, their π- and π^*- bands cross linearly at the Fermi level at the K- and K′-(Dirac) points of the hexagonal Brillouin zone (BZ), as seen in Fig.2.2. The bands display an ambipolar character and the charge carriers behave like massless Dirac fermions in a small energy range around the Fermi level, E_F.

Here we have performed first-principles plane wave calculations within Local Density Approximation (LDA)[66] using PAW potentials[67] as well as ultrasoft pseudopotentials.[16] All structures have been treated within supercell geometry using the periodic boundary conditions. A plane-wave basis set with kinetic energy cutoff of 500 eV is used. In the self-consistent potential and total energy calculations the Brillouin zone (BZ) is sampled by (25×25×1) special **k**-points.[15]

This sampling is scaled according to the size of supercells. All atomic positions and lattice constants are optimized by using the conjugate gradient method where total energy and atomic forces are minimized. The convergence for energy is chosen as 10^{-5} eV between two steps, and the maximum force allowed on each atom is less than 10^{-4} eV/Å. Phonon dispersion curves obtained using Small Displacement Method with forces calculated by VASP.[18, 19, 55, 56]

Calculated variation of the binding energy of the relaxed honeycomb structure of Si and Ge as a function of the lattice constant is presented in Fig.2.3. Here planar (PL), low-buckled (LB) and high buckled (HB) honeycomb structures correspond to distinct minima. The PL honeycomb structure is the least energetic configuration. The important question to be addressed is whether these PL, LB and HB geometries correspond to real local minima in the Born-Oppenheimer surface and hence are stable.

We start by calculation of phonon dispersions of planar silicene and germanene structures. Phonon dispersions corresponding to graphene and planar silicene structures are presented in Fig.2.4. Here one can see that the main difference between these two profiles are in their out-of-plane optical modes. As seen in, Fig.2.4 the eigenvector corresponding to this mode is composed of opposite out-of-plane motion of atoms in each sublattice. In graphene structure there is a strong restoring force against this movement which results in oscillation with wavenumber around 900 cm^{-1} at Γ-point. In the case of planar silicene there is no restoring force against such movement and this results in imaginary frequencies with amplitudes more than 100 cm^{-1} at Γ-point. This instability can be cured by letting the silicon atoms move towards directions in which they do not feel a restoring force, i.e., by letting the silicene structure buckle.

The phonon dispersion curves in Fig.2.5 indicate that 2D periodic LB honeycomb structure of Si is stable since imaginary frequencies are absent. With an equilibrium buckling Δ_{LB}=0.44 Å, its optical and acoustical branches are well separated. Two acoustical branches are linear as $\mathbf{k} \to 0$. Whereas the out-of-plane

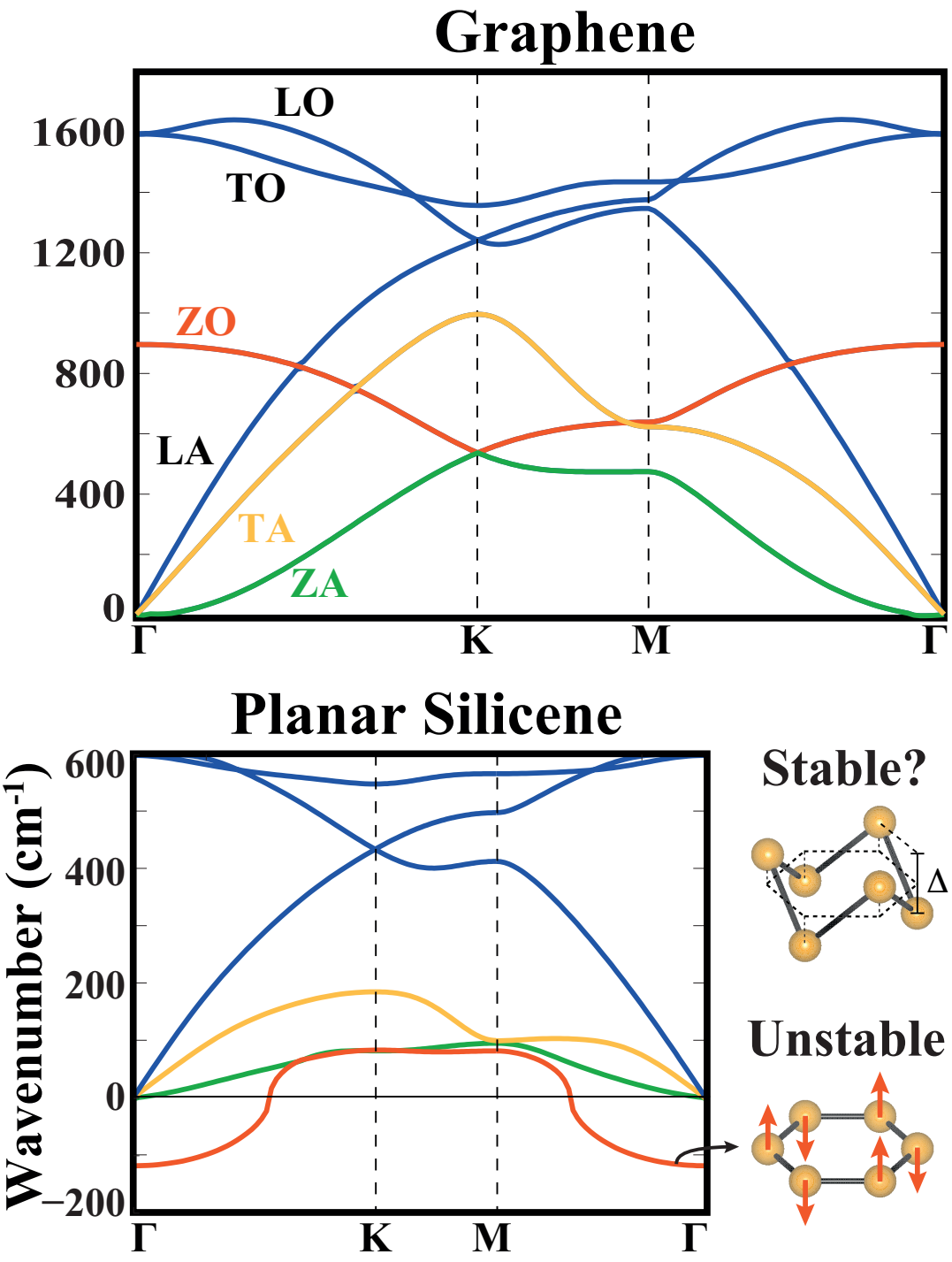

Figure 2.4: Phonon dispersion curves of graphene and planar silicene. The longitudinal, transverse and out-of-plane optical and acoustical modes are abbreviated as LO, TO, ZO, LA, TA and ZA, respectively. Eigenvectors corresponding to the out-of-plane optical mode of planar silicene is shown by arrows.

branch displays a quadratic dispersion near Γ-point, since the force constants related with the out-of-plane motion of atoms decays rapidly.[56] The phonon dispersion curves of 2D periodic LB structure of Ge having a buckling of Δ_{LB}=0.64 Å are similar to those of Si, except the frequencies of Ge are almost halved due to relatively smaller force constants. The out-of-plane acoustical phonon branch has imaginary frequencies near Γ-point. We have shown that these frequencies become positive when the grid size of the real space mesh is reduced. This way the forces are calculated more precisely.

The stability of LB structure of Si and Ge is further tested by extensive ab-initio finite temperature molecular dynamics calculations using time steps of $\delta t = 2 \times 10^{-15}$ seconds. In these calculations the (4×4) supercell is used to lift the constraint of (1×1) cell. Periodic 2D LB structure of Si (Ge) is not destroyed by raising the temperature from T = 0 to 1000 K (800 K) in 100 steps, and holding it at T = 1000 K (800 K) for 10 picoseconds (ps). A finite size, large hexagonal LB flake of Si (Ge) with hydrogen passivated edge atoms is not destroyed upon raising its temperature from 0 to 1000 K (800 K) in 100 steps and holding it for more than 3 ps.

As in the PL case, HB honeycomb structures of Si and Ge, with a buckling of $\Delta_{HB} \approx 2$ Å, also have imaginary phonon frequencies for a large portion of BZ. Moreover, structure optimization of HB structure on the (2×2) supercell results in an instability with a tendency towards clustering. Clearly, the unstable HB structure does not correspond to a real local minimum; it can occur only under the constraint of the (1×1) hexagonal lattice.

We believe that the present analysis provides stringent and comprehensive test for the stability of LB honeycomb structure of both Si and Ge. In this respect, LB structures of Si and Ge appear to be a contrast to 2D C and BN forming only stable planar honeycomb structure.[46] The situation with three different minima corresponding to PL, LB and HB geometries of 2D Si and Ge in Fig.2.3 is reminiscent of those of 1D atomic chains. Earlier, it has been shown that while several elements and III-V compounds form linear, wide-angle (i.e. LB) and low-angle (i.e. HB) atomic chains, only C and BN form stable linear

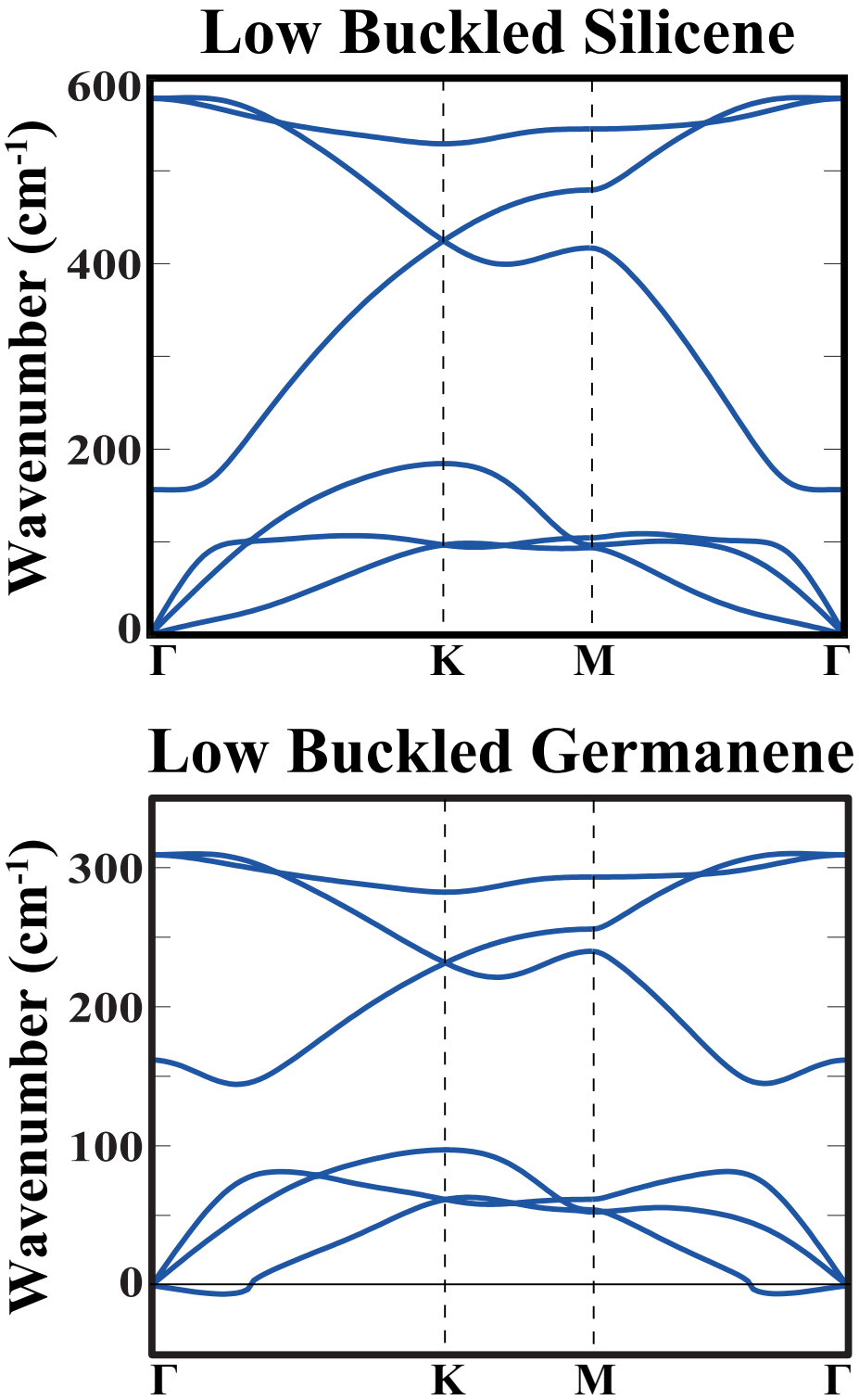

Figure 2.5: Phonon dispersion curves for low buckled silicene and germanene structures.

Table 2.1: Binding energy and structural parameters calculated for the bulk and 2D Si and Ge crystals. a_{bulk} [in Å], $E_{c,bulk}$ [in eV per atom], Δ_{HB} [in Å], Δ_{LB}, b_{LB}, d_{LB} and $E_{c,LB}$ [in eV per atom], respectively, stand for bulk cubic lattice constant, bulk cohesive energy, high-buckling distance, low-buckling distance, hexagonal lattice constant of 2D LB honeycomb structure, corresponding nearest neighbor distance and corresponding cohesive energy.

	a_{bulk}	$E_{c,bulk}$	$\triangle_{HB}$	$\triangle_{LB}$	b_{LB}	d_{LB}	$E_{c,LB}$
Si	5.41	5.92	2.13	0.44	3.83	2.25	5.16
Ge	5.64	5.14	2.23	0.64	3.97	2.38	4.15

atomic chains.[63, 64, 65] That only C and BN form linear 1D atomic chains and 2D planar honeycomb structures arises from the limited size of their $2s$ and $2p$ valance orbitals. Whereas elements from the second and third row of the Periodic Table have $2s$ and $2p$ orbitals as core states and the range of their valance orbitals is large enough to yield significant second nearest neighbor coupling. Relevant lattice parameters and cohesive energies of LB Si and Ge honeycomb structures are given in Table 2.1. Different potentials (PAW or ultrasoft pseudopotential) yielded values which differ only 1%. We note that the cohesive energies of LB structures are smaller than those for the bulk crystal of Si and Ge.

The calculated electronic band structures and corresponding density of states (DOS) of LB Si and Ge are presented in Fig.2.2. The bands of PL and LB structures are similar except that specific degeneracies split due to lowering of point group rotation symmetry from C_6 in PL geometry to C_3 in LB geometry. Similar to graphene, π- and π^*-bands of LB Si and Ge crossing at K- and K'-points at E_F are semimetallic. Around the crossing point, these bands are linear. This behavior of bands, in turn, attributes a massless Dirac fermion character to the charge carriers. Interestingly, by neglecting the second and higher order terms with respect to q^2, the Fermi velocity is estimated to be $v_F \sim 10^6$ m/s for both Si and Ge. We note that v_F calculated for LB honeycomb structures of Si and Ge are rather high and close to that of graphene. In addition, because of the electron-hole symmetry at K- and K'-points of BZ, LB Si and Ge are ambipolar for E($\mathbf{q}$)= $E_F \pm \epsilon$, ϵ being small.

Much recently, a compelling experimental evidence for the synthesis of epitaxial silicene on a silver (111) substrate was provided.[45] Using scanning tunnelling microscopy and angular-resolved photoemission spectroscopy the authors have revealed the structural and electronic properties of silicene, which are in a very good agreement with our predictions.

2.5 Fourth Acoustic Mode in Nanoribbons

Freestanding graphene sheets and nanoribbons can be produced spontaneously, but it is not the case for silicene and germanene. However, there are plenty experimental work on growth of Si nanoribbons especially on Ag surface.[68, 69, 70, 71, 72, 73, 74] These highly metallic nanoribbons are formed by self-organization and have straight, atomically perfect and massively parallel structures. The electronic structure of Si nanoribbons on Ag surface was also investigated theoretically.[75] As mentioned in Chapter 1, similar to armchair graphene nanoribbons, armchair silicene nanoribbons (ASiNR) also possess family behavior (see Fig 2.6) in the variation of their band gap with their width.[50] We have shown that this property of ASiNR can be used to build multiple quantum well structures by periodically modifying their width.[51]

One can model the band structure of armchair silicene nanoribbons in a nearest-neighbor tight-binding scheme of p_z orbitals. Here the hopping parameters, t, is taken to be the same between all nearest-neighbor atoms except the edge atoms in which it should be modified as $t(1+\delta)$. The results of ab initio calculations and parametrized tight-binding calculations are presented in Fig 2.6. It is worth to note here that, the value of δ for silicene nanoribbons was found to be 0.12 which is the same as the value reported for the graphene nanoribbons.[50]

In this section we present stability analysis of ASiNR, based on the calculation of the phonon dispersions. We have performed first-principles plane wave calculations within Local Density Approximation (LDA) using projector augmented

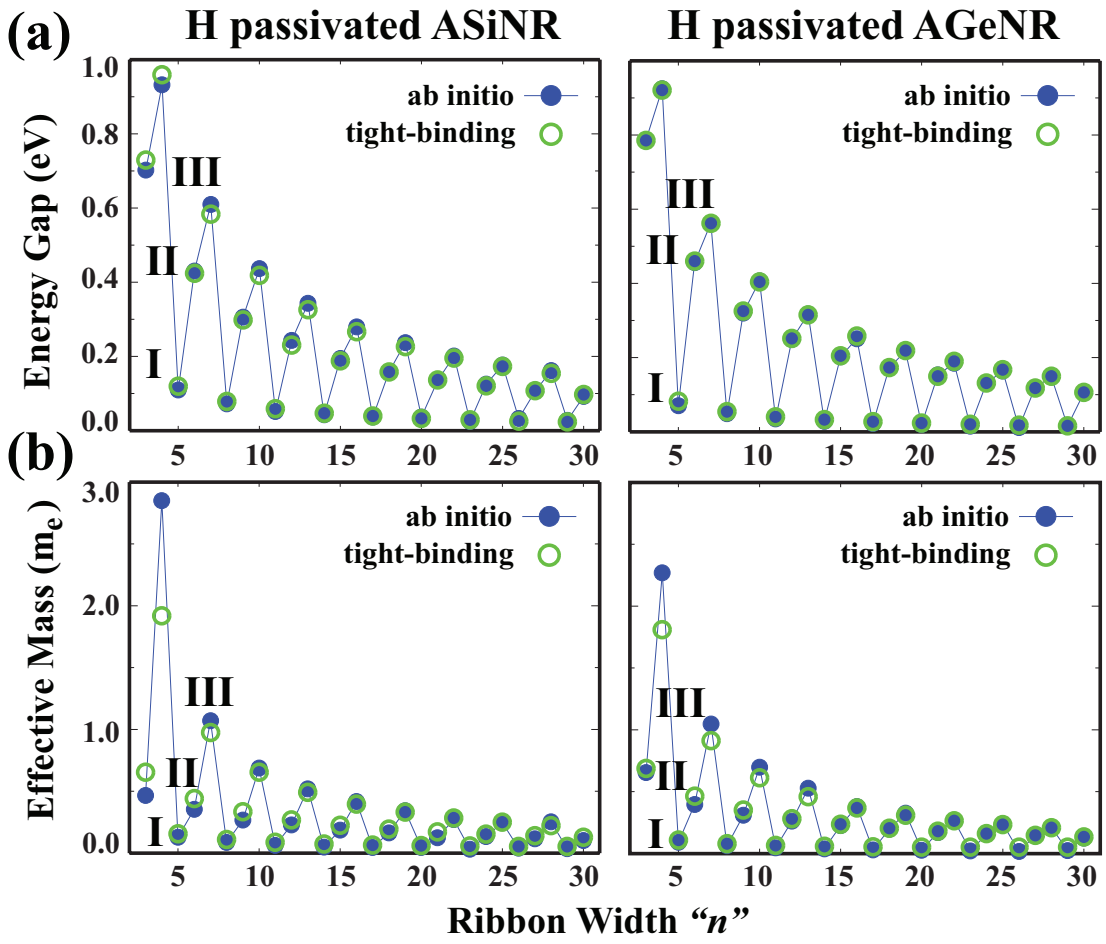

Figure 2.6: Calculated (a) energy gap and (b) effective mass versus ribbon width, n, for hydrogen saturated Si and Ge armchair nanoribbons. Filled circles indicate the ab initio results while empty circles stand for the results of the tight binding fitting. The fitting is performed using only the energy gap data. Parameters found from this fitting was used to generate the tight binding effective mass data. In each panel three branches are observed and named in increasing order of band gaps and effective masses as family I, II, and III.

wave (PAW) potentials.[66, 67] All structures are treated within supercell geometry using the periodic boundary conditions. A plane-wave basis set with kinetic energy cutoff of 300 eV is used. In the self-consistent potential and total energy calculations, the Brillouin zone (BZ) is sampled by $(15 \times 1 \times 1)$ special **k**-points. All atomic positions and lattice constants are optimized by minimization of the total energy and atomic forces. The vacuum separation between the nanoribbons in the adjacent unit cells is taken to be at least 10 Å. The convergence for energy is chosen as 10^{-5} eV between two steps, and the maximum Hellmann-Feynman forces acting on each atom is less than 0.02 eV/Å upon ionic relaxation. Numerical plane wave calculations have been performed by using VASP package.[18, 19] Phonon dispersions were obtained using the small displacement method with forces calculated in a $(5 \times 1 \times 1)$ supercell.[55, 76]

Figure 2.7(a) presents the atomic structure and bond length distribution of a sample hydrogen saturated armchair silicon nanoribbons. In contrast to bare nanoribbons, saturation by hydrogen lifts the (2×1) reconstruction at the edges.[44] In Fig. 2.7(a) there are $n = 9$ Si atoms forming zigzag chain perpendicular to the nanoribbon axis and hence this armchair nanoribbon is classified as ASiNR-9. Accordingly the number of Si (or Ge) atoms in the primitive unit cell is $2n$. Note that the bond length distribution is nearly uniform except a sudden decrease at the edges. This pattern was also observed in armchair graphene nanoribbons.[50]

Figure 2.7(b) presents the phonon dispersion profile for hydrogen saturated ASiNR-9. In the phonon dispersion profile of hydrogen saturated ASiNR-9 all modes are real. Thus, the structure is predicted to be stable. Computational cost of this calculation is very high, so we were not able to calculate the phonon dispersions for other ribbons. Nevertheless, all ASiNRs have very similar atomic configuration, and thus they are also expected to be stable. As seen in Fig 2.5 the phonon dispersion profile of 2D Ge is similar to that of Si. But in Ge structure the acoustic and optic modes are well separated. Also due to softer bonds the wavenumbers of Ge structure is halved compared to Si. Thus AGeNRs are also expected to be stable, whilst exhibiting the mentioned differences.

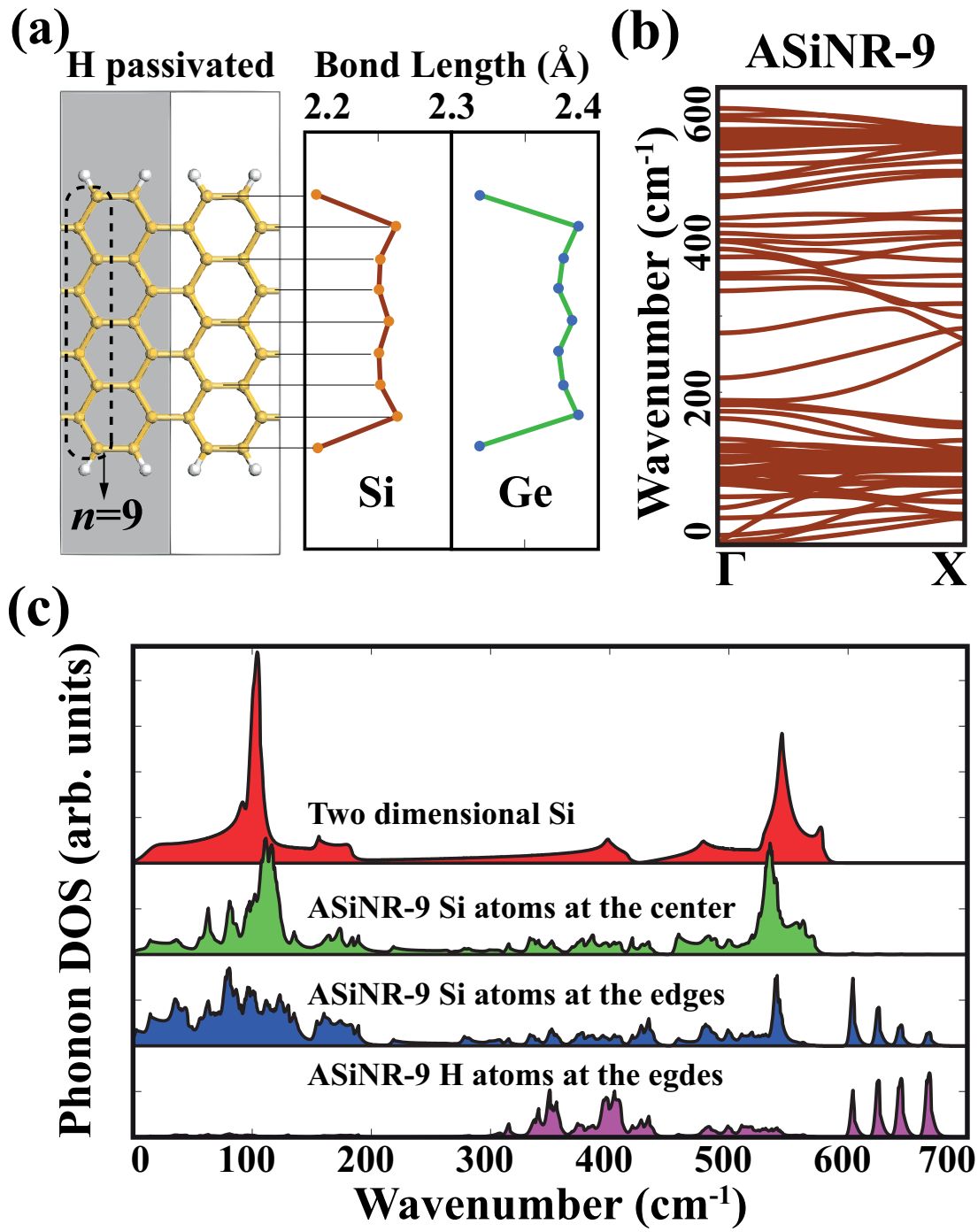

Figure 2.7: (a) Atomic structure and bond length distribution of hydrogen saturated ASiNR-9. (b) Phonon dispersions calculated for hydrogen saturated ASiNR-9. States that appear above 600 cm^{-1} are related to Si-H bonds of hydrogen saturated ASiNR-9 and were not shown. (c) Phonon DOS of the hydrogen saturated ASiNR-9 projected to Si atoms at the center and at the edges and also to H atoms at the edges. DOS of 2D honeycomb structure of Si is also presented for comparison.

Interestingly, in quasi-1D structures like ASiNR there are four acoustical modes, which is in contrast to 2D and 3D structures which possess three acoustical modes. As mentioned before, the number of acoustical modes is equal to the number of invariant transformations. In the case of quasi-1D nanostructures the fourth acoustical mode is originating from the rotational invariance that these materials have. In this respect, four phonon modes of ASiNR have zero frequency as they approach the Γ-point. The acoustic mode corresponding to the rotational invariance is usually called the twisting mode (TW).[77, 78]

Usually, acoustical modes does not converge to exactly zero due to finite numerical precision. In this case one can apply the following recursive procedure to impose the invariant symmetries to dynamical matrix;

$$D_{\text{new}} = D_{\text{old}} - (D_{\text{old}} vv^T + vv^T D_{\text{old}})/2 \tag{2.6}$$

where, D_{old} and D_{new} are old and new value of the dynamical matrix in each iteration and v is the eigenvector corresponding to invariant transformation.[78] In the case of quasi-1D structures there are three such eigenvectors corresponding to translation in Cartesian coordinates and one corresponding to rotation around the axis in which the structure is periodic. Generally sufficient precision is reached by using the recursion formula (2.6) in less than 20 iterations.[55]

Phonon densities of states (DOS) of hydrogen saturated ASiNR-9 projected to atoms at different locations in the nanoribbon are presented in Fig. 2.7(c). DOS of the 2D Si honeycomb structure is also presented for comparison. DOS projected on Si atoms at the center of the nanoribbon is very similar to that of the 2D Si. As the width of the nanoribbon increases, this similarity is expected to be enhanced. However, DOS projected on Si atoms at the edges deviate from that corresponding to 2D Si. Especially, four optical peaks above 600 cm^{-1} are clearly originating from Si-H bonds at the edges. Also modes originating from short Si-Si bonds at the edges cause changes in DOS below 600 cm^{-1}.

2.6 Friedel Oscillations in Carbon Chains

Carbon atomic chains are one-dimensional (1D) allotropic form of carbon atom, which has also allotropic forms in different dimensionalities, such as 3D diamond and graphite, 2D graphene, quasi 1D nanotube and quasi 0D fullerens. sp^D-hybrid orbitals are indigenous to the dimensionality (D=1,2,3) of these allotropic forms. Covalent bonding of $sp^{D=1}$ hybrid orbitals along the chain axis together with π-bonding of perpendicular p_x and p_y orbitals are responsible for the linear stability of the chain. Earlier carbon atomic chains (CACs) and their functionalized forms have been investigated intensively, despite the lack of consensus on whether they can really be synthesized.[79, 80, 81] These studies have predicted a wide range of interesting properties, which can make CACs a potential material for future nanotechnology applications.[82, 83]

Linear CAC structures have either identical double bonds, called cumulene or alternating short "single" and strong "triple" bonds, called polyyne. While cumulene is metallic with a quantum ballistic conductance of $4e^2/h$ due to two degenerate, half-filled p_x and p_y bands crossing the Fermi level, it is vulnerable to Peierls instability.[84] Hence, through the displacement of alternating carbon atoms by $\delta \cong 0.018$ Å the unitcell is doubled and a band gap of 0.32 eV at the edge of Brillouin zone (BZ) is opened to lower the total energy per atom by 2 meV. When the non-local part of the exchange-correlation is taken into account this energy difference is increased to 47 meV, 80 meV and 104 meV for HSE, B3LYP and PBE0 hybrid functionals, respectively.[85, 86, 87]

While segments of polyynes terminated with H atoms at both ends (H-C_n-H), have been produced[88, 89] up to considerable lengths (n=20), cumulene production is relatively difficult due to their frailty. Small cumulene chains terminated by H_2, (H_2-C_n-H_2) groups have been synthesized.[90, 91] Freestanding CACs from graphene flakes were produced by using energetic electron irradiation inside a transmission electron microscope (TEM).[92] Concomitantly, it was demonstrated that not only CACs, but also SiACs and BNACs can be derived from their corresponding honeycomb structure under uniaxial tensile stress in the plastic deformation range.[93] Much recently, polyyne structure consisting of 44

carbon atoms have been produced.[94]

Here we present our work on stability of CACs using phonon dispersion analysis. Here we used the small displacement method, as in previous sections, but this time it led us to a remarkable property of CACs. As shown in Fig 2.8, we have found that the phonon dispersion curves of CACs does not converge until a very long unitcell composed of at least 80 carbon atoms is used. This means that, a local perturbation created through the displacement of a single atom in the chain creates atomic forces which are propagating to long distances in the chain. Due to these long-ranged interactions, finite size CACs attain even-odd disparities in the distributions of bond lengths and atomic magnetic moments depending on the type of saturation of carbon atoms at both ends. Even-odd disparities are also mirrored in the phonon dispersion profile of cumulene, as seen in Fig 2.8. Phonon profiles of cumulene and polyene also provides a stringent test for occurence of Peierls instability in CACs. Note that, the longitudinal acoustic mode of cumulene have imaginary frequencies around the BZ edges. This mode corresponds to the movement of carbon atoms opposite to each other along the axis, which results in stable polyene structure. In contrast to the long-ranged interactions of CACs in longitudinal direction, the transversal force constants decay rapidly, which leads to appearance of quadratic terms in the phonon dispersions of transversal modes near the center of BZ.

Now we present the physical explanation for the aforementioned atomic force and difference charge density oscillations in CACs. To reveal its nature we consider oscillations of bare C_{100}, $B_{50}N_{50}$, B_{100} and Al_{100} chains generated by a slight displacement of the 50^{th} atom. Despite its zigzag metallic ground state,[63] here we consider linear Al-chain for the sake of comparison. After the structural relaxation, all atomic positions are kept fixed except the 50^{th} atom, which was displaced in longitudinal direction by δz taken to be 0.02 Å for C_{100}, $B_{50}N_{50}$, B_{100} and 0.04 Å for Al_{100} chain. Difference charge density is obtained by subtracting the charge density of the perturbed structure from that of the unperturbed one, which is averaged in planes perpendicular to the chain axis. In the left panel of Fig. 2.9, the force and linear charge density perturbations of only three nearest neighbors of the 50^{th} atom is shown. The right panel of the Fig. 2.9 presents the

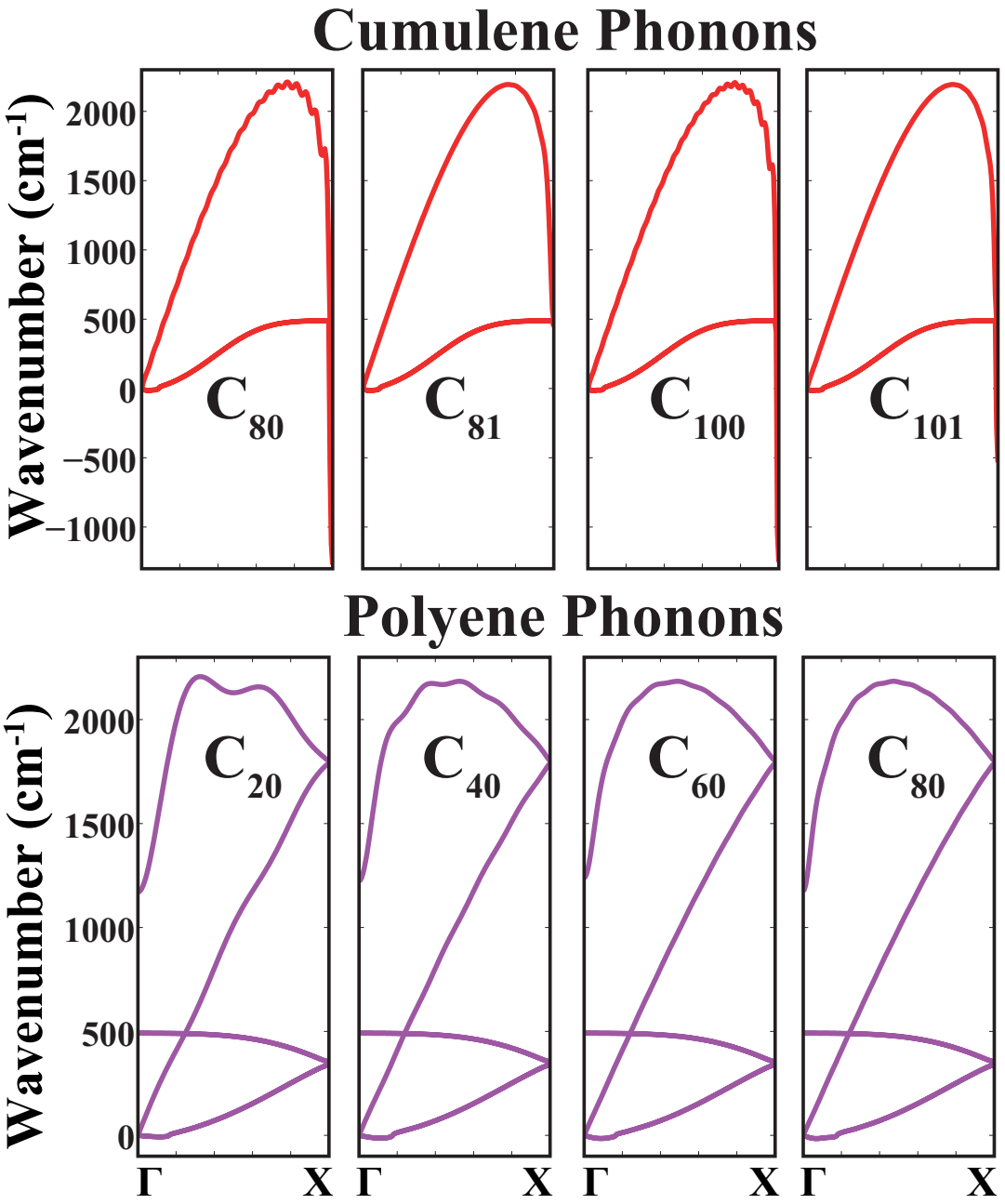

Figure 2.8: Phonon dispersion profiles of cumulene and polyene structures. The number of carbon atoms in the unitcell is given as a subscript.

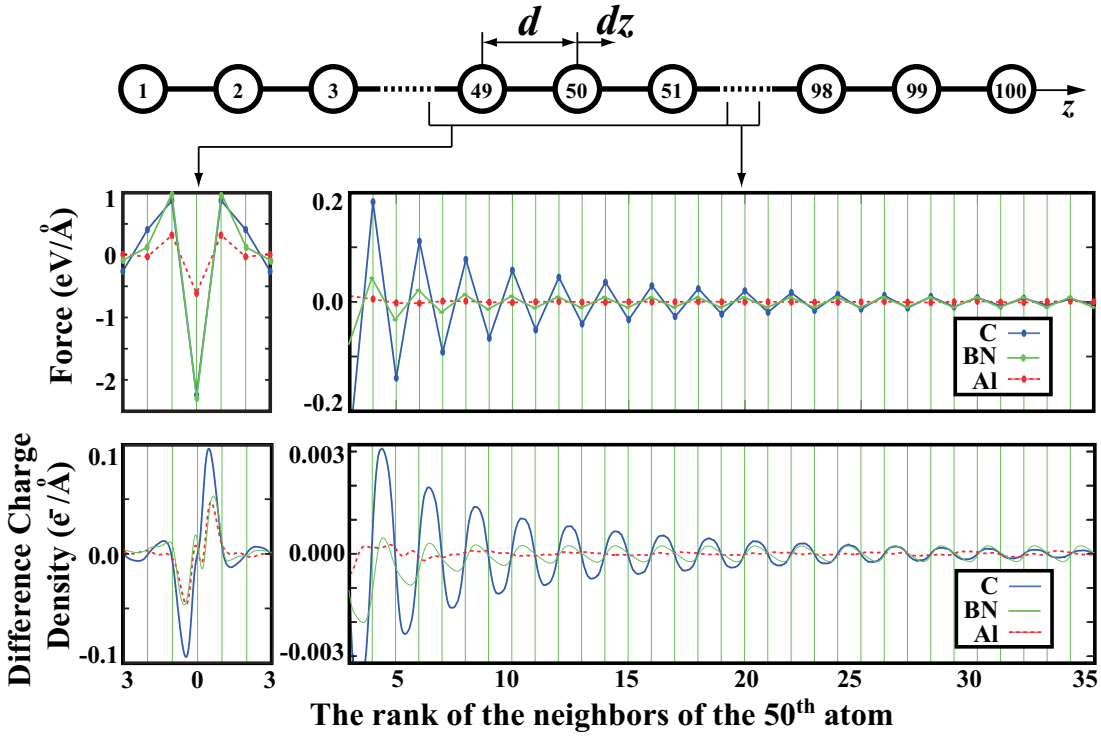

Figure 2.9: Forces and difference charge density perturbations formed in finite C_{100}, $B_{50}N_{50}$ and Al_{100} atomic chains due to a small longitudinal displacement, δz, of the 50^{th} atom near the center of the chain. The upper panel is a schematic representation of the geometry of the system. The middle panel presents force distribution for three nearest neighbors (left) and extensions up to 35^{th} neighbor. In the similar manner the bottom panel presents the difference charge density perturbations. Atomic magnetic moments (which are not shown in the figure) also behave similarly, and have long-ranged oscillations in CAC.

extensions of these perturbations up to the 35^{th} neighbor of the 50^{th} atom. One can see that these extensions are negligible and show no obvious pattern in Al chains. Similar pattern is also seen in Boron atomic chains. In CACs, however, the perturbation extensions are long-ranged and exhibit a decaying-oscillatory behavior. The envelope of these oscillatory extensions fits to a $1/r$ decay rate (r being the distance to the 50^{th} atom) for both force and linear charge density perturbations. Similar pattern is also seen in $B_{50}N_{50}$ chain, but both force and charge density oscillations are weaker compared to that of C_{100}.

The above oscillatory decay in the linear charge density perturbation provokes an association with so called Friedel oscillations.[95] Inserting an impurity charge to an electron gas results in the accumulation of electronic charge, which screens the Coulomb potential introduced by the impurity. Since the wave vector of the electron gas is limited by its density, the accumulated charge acquires decaying Friedel oscillations. For sufficiently large separations, r, from the impurity, the Friedel oscillations are proportional to the function $\sin(2k_F r)/r^D$, where k_F and D stand for the Fermi wave vector and dimensionality of the electron gas system, respectively.[96] Recently it was shown that, upon inclusion of an impurity in a two-dimensional graphene structure, where $D = 2$, the charge density oscillations proportional to $\sin(2k_F r)/r^2$ are obtained.[97] In case of CAC, one can think of the displacement of the 50^{th} atom near the center of the chain as the insertion of two impurity charges having opposite signs.[98] Since the carbon chain system is one dimensional, the Friedel theory can explain the $1/r$ decay rate.[99] In cumulene structure the double degenerate π-bands are half filled, so the Fermi wave vector is $k_F = \pi/2c_c$. In polyyne structure bands are folded and the Brillouin zone is halved and the Fermi wave vector of filled π-bands is $k_F = \pi/c_p$. Thus the periodicity of observed charge density oscillations fits the Friedel theory for both polyyne and cumulene structures (and also for BN chains).

One should note that, Friedel theory holds for free electron like systems. In our case, the π-bands of atomic chains are expected to behave as free electron systems, since their charge density have nodes on the axis where the ions lie. Figure 2.10 presents the band structure of AlAl, BB, BN and polyyne chain structures. All structures are considered in a unitcell having two atoms for the sake of comparison. The left panel presents the whole band profile, while the right panel zooms to the π-bands of chain structures and compare them with free electron dispersion. As seen in the right panel of Fig. 2.10, the π-states of all chain structures considered here have a dispersion profile which is very similar to that of a free electron. In fact the effective masses of π-bands of BB, CC, AlAl and BN chain structures exceed the mass of free electron by only 2%, 7%, 8% and 17%, respectively. Here the effective masses are calculated from the curvature of the $E(k)$ profile around the Γ point.

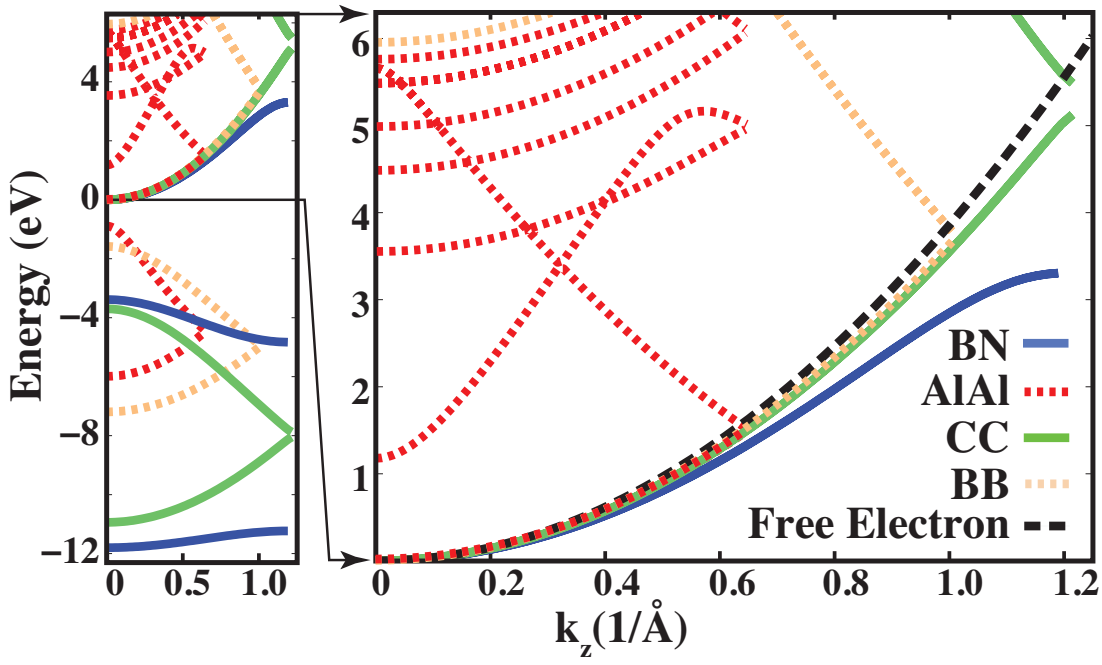

Figure 2.10: Energy band structures of AlAl, BB, BN and polyyne chain structures. A closer view of π-bands together with the dispersion profile of one-dimensional free electron gas system is presented in the right panel. Zero of energy is set to the minima of π-bands for each structure. For the sake of clarity, the bands of the chain structures beyond the first Brillouin zone in the extended scheme are not shown.

BB and AlAl chains both have six valence electrons in a unitcell consisting of two atoms. The folded double degenerate π-bands of these structures are half filled, which result in $k_F = \pi/4c$. Considering that, the π-band dispersion of BB chain is closer to free electron dispersion compared to that of polyyne, one expects the BB and AlAl chains to have Friedel oscillations with a periodicity of $4c$. However, there is no such profile present in force or charge density oscillations of AlAl chains, as seen in Fig. 2.9. We think that, in AlAl and BB chains the Friedel oscillations, which is a feature of a free electron systems, is suppressed by ionic potential. In CC and BN chains the oscillations have a periodicity of $2c$, which resultes in very small charge density perturbations near the atomic sites. In AlAl and BB chains, however, the charge density oscillations with a period of $4c$ are expected to have maxima on atomic sites. This enhances the contribution

of ionic potential, so that, π-bands deviate from free electron like behavior. As a result, the charge density perturbations, being a feature of free electron like system, are suppressed and the system finds a self consistent energy minimum with no Friedel oscillations. Note that, force and charge density oscillations are weaker in BN chains compared to that of CACs. This is because, the π-bands of BN chains considerably deviate from free electron behavior, as seen in Fig. 2.10.

The force distribution observed in Fig. 2.9 can be related to the charge density oscillations; as mentioned before, in the absence of any perturbation, the minimum of energy is met by symmetric charge densities around the atomic sites. As the charges start to move in one direction, the atomic sites start to feel a force in the same direction. To the first order, these two events are directly proportional and this explains the oscillating $1/r$ decay of the atomic forces. Note that, the 50^{th} atom and its neighbors feel the elastic forces generated by displacement. Thus, they are not in the same direction as the charge accumulation.

Chapter 3

Dissipation Phenomena

In this section, the basic concepts of dissipation phenomena is summarized. The dissipation of non-equilibrium phononic and electronic states are discussed. The generation of non-equilibrium states through adiabatic and sudden processes mentioned here is important for understanding of our contributions in the field of friction presented in forthcoming chapters.

3.1 Introduction

Dissipation of nonequilibrium phononic and electronic states have important role in theory of friction. Dissipation arises in systems having large number of interacting degrees of freedom. In sufficiently large systems, the macroscopic behavior of the system is generally irreversible even though the microscopic interactions are governed by reversible dynamics. In such systems, there is a probability distribution of states corresponding to equilibrium which occupies the largest volume in the configurational phase space. Any non-equilibrium distribution of states is less probable and over time such distributions are equilibrated through microscopic interactions. Note that, if interaction between states are absent the system remains in initial non-equilibrium distribution. For example, as shown in Chapter 2 phonons arise from the harmonic interaction between ions. However, their

interaction is governed by anharmonic terms of ionic interactions. In a perfectly harmonic crystal, phononic states would remain in their initial distribution while in a highly anharmonic crystal they are quickly equilibrated through phononic dissipation.

In a system with dissipation the detailed analysis of large number of degrees of freedom has no practical importance and one needs to lump this unnecessary information in few parameters describing the overall behavior. In such systems, integrating out the degrees of freedom leads to Langevin equation [100] which in its simplest form can be written as;

$$m\frac{d^2x}{dt^2} = -m\gamma\frac{dx}{dt} + f(t) \tag{3.1}$$

where $f(t)$ is a random force which obeys the fluctuation-dissipation theorem [101];

$$\langle f(t)f(t^{'})\rangle = 2\gamma m k_B T\delta(t-t^{'}) \tag{3.2}$$

and γ is a measure of dissipation or microscopic friction. One can show that integration of equations (3.1) and (3.2) leads to

$$\langle\frac{1}{2}m(\frac{dx}{dt})^2\rangle = \frac{1}{2}k_B T. \tag{3.3}$$

Usually there are several mechanisms involved in dissipation. In such cases the total microscopic friction can be obtained by summing the contributions from individual mechanisms. For example, if a system possesses both electronic and phononic contribution to dissipation the overall dissipation is written as;

$$\gamma_{\text{total}} = \gamma_{\text{electronic}} + \gamma_{\text{phononic}}. \tag{3.4}$$

In the following sections we discuss simple models of phononic and electronic dissipation.

3.2 Phononic Dissipation

Here we present a model of phonic friction in a simple case where an atom is adsorbed on a crystal surface.[102] We derive the microscopic friction force $-m\gamma v$

felt by atom when it is dragged with velocity v over the crystal. As pointed out by Einstein in one of his miraculous 1905 papers,[103] drag forces felt by objects that are pulled in a certain medium had same origin as the random forces acting on the particle when it is at rest. In a similar manner one can relate the dissipation rate of adsorbate's mechanical energy energy due to its collisions with surface with the force it feels when it is dragged over the surface. Then, noting that $Fv = dE/dt$ and $E = mv^2/2$, one can rewrite the $-m\gamma v$ force as the energy dissipation rate equation;

$$\frac{dE}{dt} = -2\gamma E. \tag{3.5}$$

Now let us assume that the adsorbed atom has a natural vibration frequency of ω due to its interaction with the substrate. Then it can be thought to have a collision with some portion of the crystal in each time interval $\tau \sim 1/\omega$. Since the collision will propagate in the crystal with sound velocity c, the mass of the colliding portion of the crystal can be written as $\rho(c\tau)^3$ where ρ is the density. Upon collision adsorbate will transfer energy proportional to the ratio of its mass to the mass of the crystal portion it has collided. This analysis results in a dissipation rate which can be written as;

$$\frac{dE}{dt} = -\frac{m/\rho(c\tau)^3}{\tau}E \tag{3.6}$$

which leads to

$$\gamma \propto \frac{m\omega^4}{\rho c^3}. \tag{3.7}$$

Here we have consciously dropped the coefficients in front of the right hand side, because the analysis was not done rigorously.

The dependence of phononic dissipation on adsorbate properties as presented in equation (3.6) was confirmed in an elegant experimental study by Cannara *et al.*[104] They have adsorbed hydrogen and deuterium on single-crystal diamond and silicon surfaces. They have used atomic force microscope to reveal the friction force on these surfaces. As predicted by the model discussed above, they have discovered that surfaces terminated by deuterium showed lower friction. Here we would like to point out that, this is one of few experiments in which the friction force is shown to be influenced by phononic dissipation mechanism. Note that, due to stiff C-H and C-D bonds the system is probably in continuous

sliding regime in which no sudden processes occur. Absence of sudden generation mechanisms reveals the importance of phononic dissipation mechanisms.

Another interesting friction experiment was performed on single and bilayer graphene on SiC substrate.[105] Here the friction force on a single layer graphene was found to be two times higher than that of a bilayer graphene surface. The authors attributed this difference to higher electron-phonon coupling in single layer graphene compared to bilayer. They conclude that due to higher electron-phonon coupling in single layer graphene the generated vibrations are dissipated very rapidly while in bilayer case the mechanism for efficient dissipation is absent and thus the layers jump back and forth and as a result the net force is lowered. This experiment was followed by another interesting work which found similar trends for single and bilayer graphene.[106] They have also found the diminishing trend of friction to extend to bulk graphite which was different from result of the former experiment. The latter work attributed the observed trends to completely different mechanism. They claim that, the difference arises from the fact that fewer layers have lower sheet stiffness which results in larger wrinkles while a tip is slid over them.

3.3 Electronic Dissipation

In the case of phonic friction, the moving adsorbate creates a bulk or surface phonon which then dissipates. In the case of electronic friction, interactions between conduction electrons and moving adsorbate result in creation of electron-hole pairs which are dissipated by recombinations. Here we summarize a simple model of electronic friction due to the movement of adsorbates on metallic surfaces.[107]

Consider a metallic slab of thickness d and area A as shown in Fig 3.1(a). Due to interactions of conduction electrons with phonons and impurities the slab will have a resistivity ρ which can be written as;

$$\rho = E/J \tag{3.8}$$

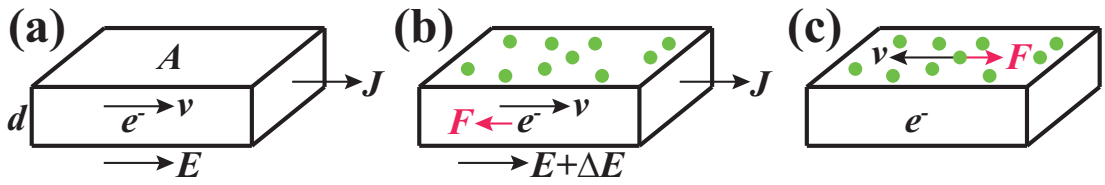

Figure 3.1: Simple model of electronic friction. (a) Electrons of a metallic block move with velocity v and produce a current density J under the influence of applied electric field E. (b) Atoms are adsorbed on the block and the electrons feel a dissipative force due to interactions with adsorbates, as a result electric field has to be increased to produce the same current density J. This can be measured as an increase in the resistivity. (c) In the reference frame of electrons the adsorbates move with velocity v and feel a dissipative force in the opposite direction.

where J is current density and E is applied electric field. Now let us put n_a adsorbates per unit area of metallic surface as shown in Fig 3.1(b). This will increase the resistivity by $\Delta\rho$, which can be expressed as;

$$\Delta\rho = \Delta E/J. \tag{3.9}$$

In this case, the total friction force felt by electrons due to interactions with adsorbates can be written as;

$$F = n_e A d e \Delta E \tag{3.10}$$

where n_e is the number of electrons per unit volume, A is the surface area and d is thickness of the metallic slab. Now let us look at the system from the reference frame of electrons as shown in Fig 3.1(c). Here adsorbates are moving with velocity v and feel a friction force $F = -n_a A m_a \gamma v$. Using equations (3.9) and (3.10), and noting that $J = n_e e v$ one can write the magnitude of electronic friction as;

$$\gamma = \frac{n_e^2 e^2 d}{m_a n_a}\Delta\rho. \tag{3.11}$$

This relation was confirmed by experimental work in which the change in the resistivity was measured with respect to Xe coverage of Xe/Ag adsorption system.[108] In this experiment it was found that, $\Delta\rho$ is proportional to n_a as expected from

(3.11). However, this trend starts to deviate as the monolayer Xe coverage is approached. Another interesting experiment was performed on pn juctions where a higher friction is reported in p part under positive bias.[109] This result is also in accordance with equation (3.11), since under positive bias the p part have higher carrier concentration.

3.4 Adiabatic and Sudden Processes

In sliding friction the non-equilibrium phononic and electronic states can be generated in two ways. The first way is generation through adiabatic processes. This kind of processes are generally not localized in space or time, which means that one can not show a microscopical region where such events start or end. For example, when two identical surfaces with weak interactions are slid over each other with equal but opposite center of mass velocities (which are well below the atomic vibration velocities), the system possesses an adiabatic non-equilibrium. The equilibrium configuration for such system is reached when atoms in both surfaces have same velocity distribution. The system will dissipate until this equilibrium is reached and all mechanical energy is transformed into random atomic vibrations. The surfaces will feel a force opposite and proportional to their center of mass velocity. This is, in general, the case for dissipative systems with adiabatic non-equilibrium generation mechanisms. The phononic and electronic dissipation mechanisms discussed above can be considered as examples in which the generation of non-equilibrium is adiabatic.

The second way is to generate non-equilibrium states through sudden processes. In this case, the process of generation can be traced by looking in a certain microscopical region in a certain time. As an example, consider a surface with asperities which have adhesive interaction with each other. When such surfaces are slid over each other asperities that come close will cling to each other. Then they will be stretched due to the relative motion of surfaces that they are attached to. At some critical strain asperities will suddenly detach from each other and release all energy they have stored during the stretching as a burst of

non-equilibrium phonons. Sliding systems which have this kind of microscopic events are said to be in the stick-slip regime. Systems in the stick-slip regime are discussed in detail in Chapter 4.

Here it is important to point out that, if a non-equilibrium state is generated then it will be certainly dissipated no matter how weak the dissipation mechanisms are. The strength of the dissipation mechanisms only determine the time interval in which the equilibrium is reached. There is no way to regain the energy that comes off during the generation of non-equilibrium states. For this reason, the sudden processes determine the frictional properties of the systems which are in the stick-slip regime. In such systems the microscopic dissipation mechanisms have less importance and are usually lumped in a single coefficient as in equation (3.4).

Chapter 4

Simple Models of Friction

In this chapter, we present widely appreciated models of friction. Models presented here have been subject of many theoretical works because of the rich physics they possess in contrast to their simplicity. These models provided theoretical explanations to various phenomena in sliding friction, like unusual dependence of friction on sliding velocity, temperature and surface mismatch.

4.1 Prandtl-Tomlinson Model

In the late 1920s when Einstein and Bohr were having a debate on philosophical issues brought by the newly developing quantum theory, Prandtl [24] and Tomlinson [25] separately developed concepts which are still at the heart of much older problem of friction. As pointed out in Chapter 1, their model explained the weak dependence of friction on sliding velocity. Here we present the important aspects of this model.

We start by pointing out that, Prandtl-Tomlinson model is one of the simplest yet being one of the most effective models describing the generation mechanism of non-equilibrium phonons. In this model, an elastic spring is dragged over a surface, as shown in Fig 4.1(a). The tip of this spring is interacting with the

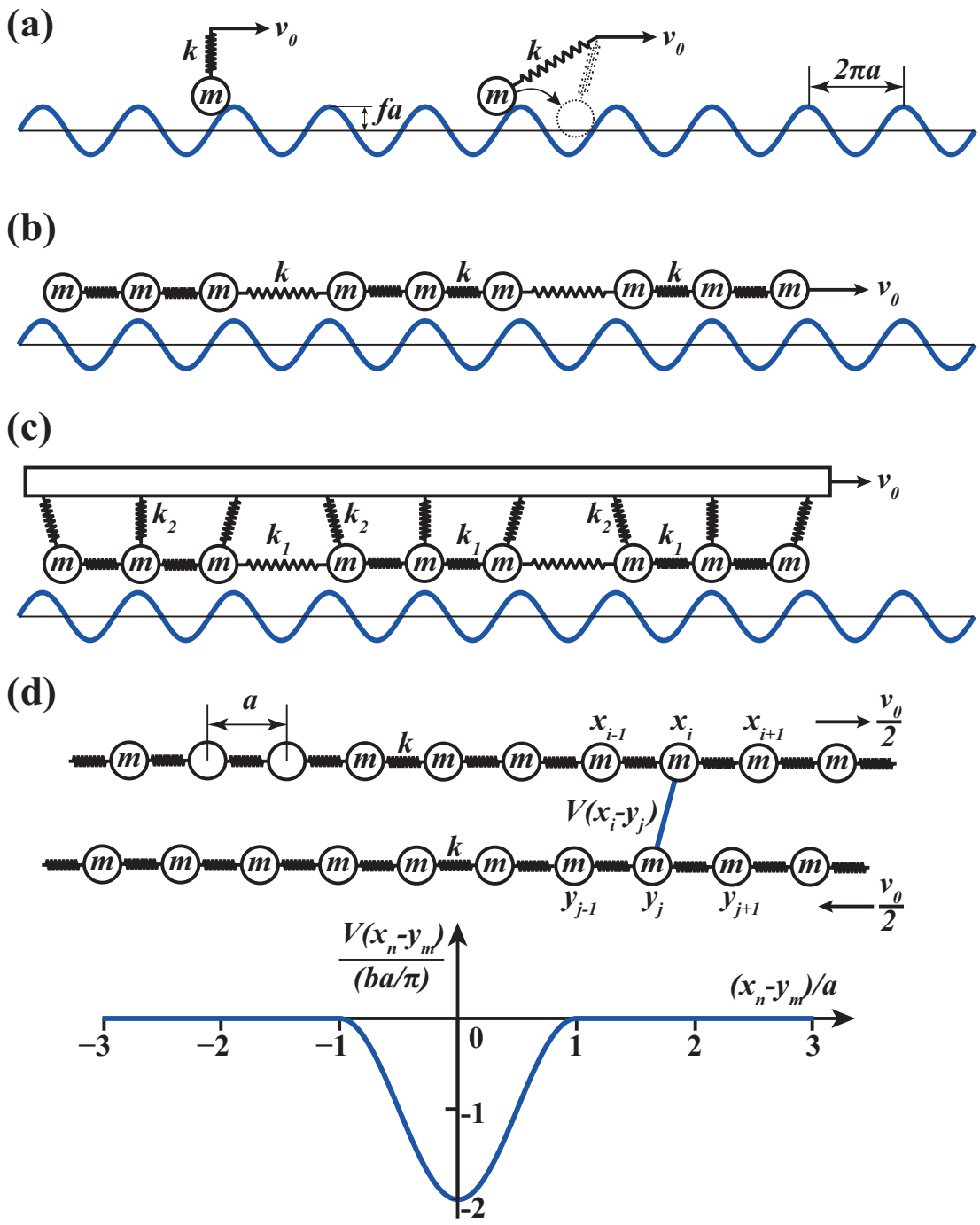

Figure 4.1: Simple models of friction. Schematic representation of (a) Prandt-Tomlinson (b) Frenkel-Kontorova and (c) Frenkel-Kontorova-Tomlinson models. (d) Model of two interacting Frenkel-Kontorova chains. The interaction potential is given below the model.

surface according to some potential energy landscape depending on the position of the tip on the surface. The other end of the spring (or the head of the spring) is pulled with constant velocity in certain direction. The restoring force on the tip is assumed to be directly proportional with the deviation of the tip from its equilibrium position. In the manner described in Chapter 3, the dissipation due to interactions of the tip with surface atoms is lumped in a microscopic friction term proportional to the velocity of the tip. Assuming that the interaction between the tip and the surface has a sinusoidal profile one can write an equation of motion for the tip as following;

$$m\ddot{x} = -m\gamma\dot{x} + k(v_0 t - x) + f sin(x/a) \tag{4.1}$$

which can be written in dimensionless form as;

$$\ddot{\tilde{x}} = \tilde{\gamma}\dot{\tilde{x}} + \tilde{k}(\tilde{v_0}\tilde{t} - \tilde{x}) + sin(\tilde{x}) \tag{4.2}$$

where dimensionless variables are defined as $\tilde{x} = x/a$, $\tilde{\gamma} = \gamma\sqrt{ma/b}$, $\tilde{k} = ka/f$, $\tilde{v_0} = v_0\sqrt{m/ba}$ and $\tilde{t} = t\sqrt{b/ma}$. Here the most important parameter is $\tilde{k}$ which represents the ratio of the stiffness of the tip to the curvature of surface energy at its maximum points. If $\tilde{k} > 1$ the total energy of the tip-surface system always have one minimum. In this case, for small velocities the tip gradually follows this minimum without making any sudden jumps. However when $\tilde{k} < 1$ the system possess multiple local minima and the tip can jump from one to another during sliding. This issue is explored further in Chapter 5. For this simple system transition from stick-slip to continuous sliding regime occurs around $\tilde{k} = 1$. Here another important parameter is $\tilde{\gamma}$. The system shows overdamped and underdamped behavior when $\tilde{\gamma} \ll 1$ and $\tilde{\gamma} \gg 1$, respectively.

One can trace the force needed to slide the tip by calculating $\tilde{k}(\tilde{x_0} - \tilde{x})$ where $\tilde{x_0} = \tilde{v_0}\tilde{t}$ is position of the other end of the tip. The result of such calculation is presented in Fig 4.2. Here the tip is slid forward and backward to complete a friction loop. The are covered by this loop correspond to the dissipated energy. One can see in Fig.4.2(a), (b) and (c) that when $\tilde{k} > 1$ the force loop is smooth which corresponds to continuous sliding. Comparing the area covered by loops presented here one can see that the friction force in continuous sliding regime is proportional to $\tilde{\gamma}\tilde{v_0}$.

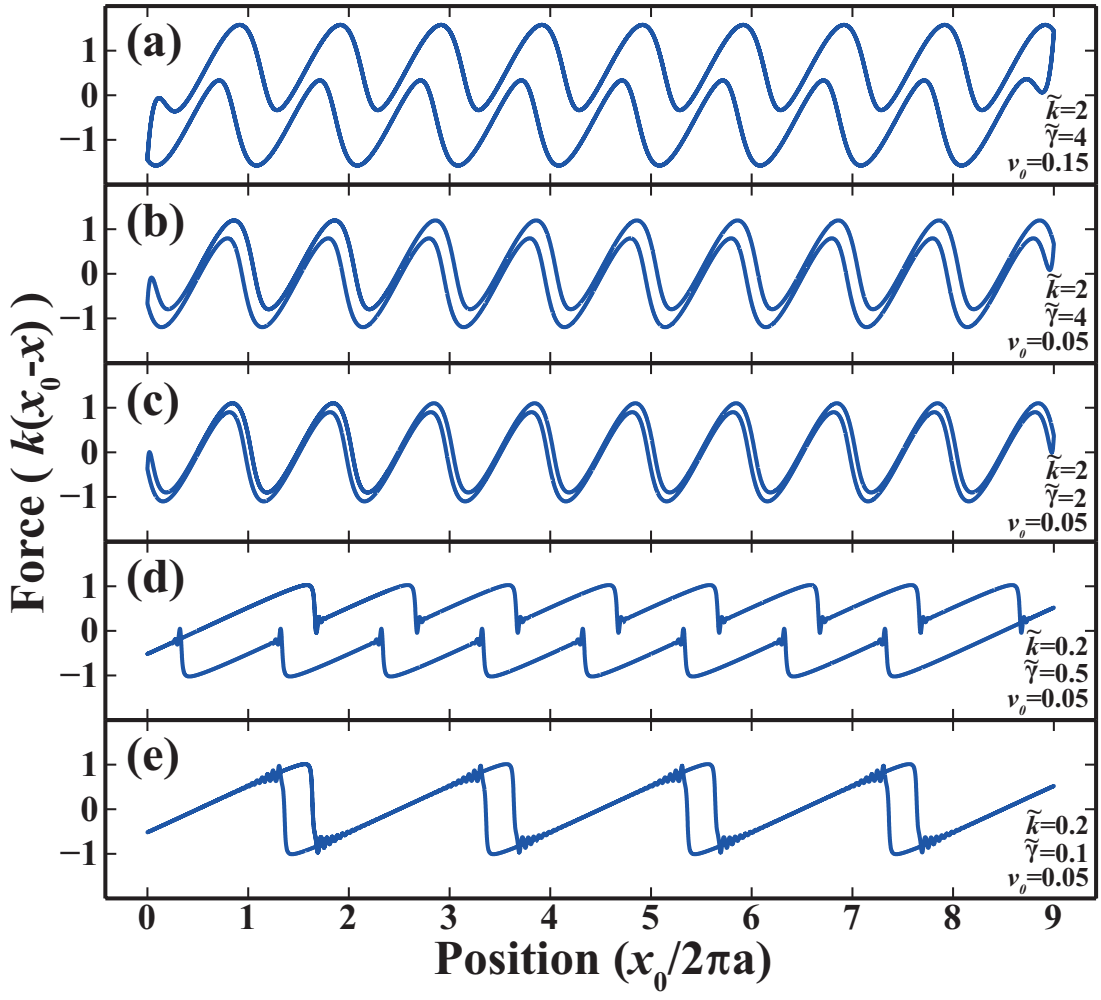

Figure 4.2: Friction force felt by the tip during forward and backward sliding. The model parameters in each case are; (a) $\tilde{\gamma}$=4, $\tilde{k}$=2, $\tilde{v}_0$=0.15 (b) $\tilde{\gamma}$=4, $\tilde{k}$=2, $\tilde{v}_0$=0.05 (c) $\tilde{\gamma}$=2, $\tilde{k}$=2, $\tilde{v}_0$=0.05 (d) $\tilde{\gamma}$=0.5, $\tilde{k}$=0.2, $\tilde{v}_0$=0.05 (e) $\tilde{\gamma}$=0.1, $\tilde{k}$=0.2, $\tilde{v}_0$=0.05

Conversely, force loops having sudden changes can be seen in Fig.4.2(d) and (e) which corresponds to stick-slip regime with $\tilde{k} < 1$. Comparing Fig.4.2(c) and (d) one can see that the area covered by the friction loop is much larger in (d), despite the decrease in $\tilde{\gamma}$. This shows that in stick-slip regime the friction force has much larger contribution from sudden processes compared to $\tilde{\gamma}\tilde{v_0}$ term that appear in continuous sliding regime. Another interesting phenomena is observed when Fig.4.2(d) and (e) are compared. One can see that when $\tilde{\gamma} = 0.1$ the system is in underdamped stick-slip regime where double slips occur.

The trends mentioned above are summarised in Fig. 4.3(a) where the variation of the average friction force $\tilde{F}$ with sliding velocity $\tilde{v_0}$ is presented. Here the blue curves are provided for comparison with friction hysteresis loops presented in Fig. 4.2 which have same parameters. Here it is clearly seen that, when $\tilde{k} > 1$ the average friction force linearly varies with sliding velocity and approaches zero as the velocity goes to zero. However, when $\tilde{k} < 1$ the average friction force converges to some finite value as sliding velocity approaches zero. The linear $\tilde{\gamma}\tilde{v_0}$ dependence is superimposed on this finite value. Note that, when $\tilde{k}$ and $\tilde{\gamma}$ are small while $\tilde{v_0}$ is above some critical value, the system starts to show multiple slips which in turn lowers the average friction force dramatically. The red curves are calculated using parameters from Ref.[110] and agrees very well with results provided there.

4.2 Frenkel-Kontorova-Tomlinson Model

In 1938, Russian physicists Frenkel and Kontorova proposed a simple model[111] which is now used to describe physical phenomena like earthquake dynamics, dislocations, domain walls, Josephson junctions and etc.[112] It is also widely used in investigation of frictional properties. The simplest form of the model is shown in Fig 4.1(b). Here again atoms are dragged over a surface having some potential energy profile, but this time atoms are assumed to have interactions with each other. In friction studies, this model is usually combined with Prandtl-Tomlinson model as shown in Fig 4.2(c), which is named as Frenkel-Kontorova-Tomlinson

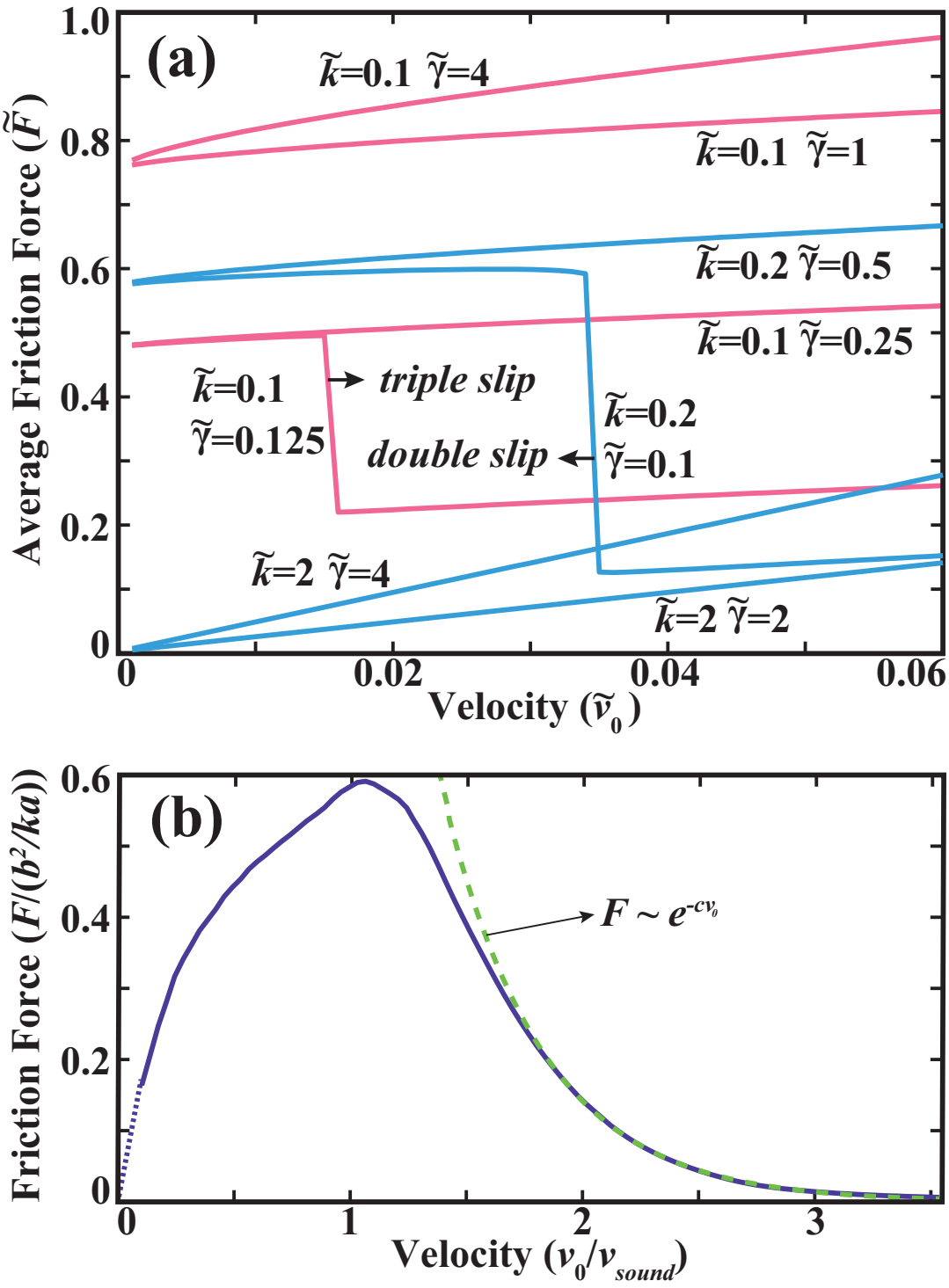

Figure 4.3: Variation of average friction force in (a) Prandtl-Tomlinson and (b) Multichain Frenkel-Kontorova models.

(FKT) model.

FKT model is especially successful in treating the frictional properties between incommensurate surfaces. Weiss *et al.* have investigated static and dynamical properties of dry friction in FKT model.[113, 114] They start by defining the static friction force as the smallest driving force above which no stable stationary state exists. Then they show that depending on how much the surfaces are incommensurate there is a value of interaction strength below which static friction ceases to exist. This value is maximum when the surfaces are ideally incommensurate, i.e., the ratio of lattice constants of two surfaces is equal to the golden ratio $(\sqrt{5}+1)/2$.

4.3 Multichain Frenkel-Kontorova Model

Dynamical properties of multiple Frenkel-Kontorova chains were investigated in the work by Röder *et al.*[115] The work particularly concentrates on the case where there are two Frenkel-Kontorova chains moving in opposite directions in one dimension and interacting with each other. Two dimensional simulations are also performed but the results does not have impact on the conclusions about the early stages of the motion. The main conclusion of the work is that the system shows complicated dependence of friction force on the relative velocity. Interestingly, it was found that the asymptotic dependence of friction force at high relative velocities decreases as $1/v^3$. Our model discussed below is mainly inspired by this work and show similar behavior at high velocities. This kind of cubic dependence was also found in FKT model calculations.[114] In a more realistic model investigating the friction between two thick slabs, Sokoloff has found an asymptotic dependence of the form $1/v$ for the friction force at high velocities.[116]

Our model is described in Fig 4.1(d). Here we have two Frenkel-Kontorova chains which is composed of stiff interatomic springs. Atoms from different springs interact with a weak short ranged potential, as shown below the model. To avoid

sudden processes we assume that $ka \gg b$. Here we would like to reveal the nature of dissipation due to interactions between large number of degrees of freedom. In this respect, we do not use the γ term as in equation (4.1). The equations of motion can be written as;

$$\begin{aligned} m\ddot{x}_i &= k(x_{i+1} + x_{i-1} - 2x_i) - \textstyle\sum_{j=1}^{N} \frac{\partial V(x_i - y_j)}{\partial x_i} \\ m\ddot{y}_j &= k(y_{j+1} + y_{j-1} - 2y_j) - \textstyle\sum_{i=1}^{N} \frac{\partial V(x_i - y_j)}{\partial y_j} \end{aligned} \tag{4.3}$$

with interatomic potential

$$V(d) = \begin{cases} -(ba/\pi)(1 + cos(\frac{\pi d}{a})) & \text{if } d \leq a \\ 0 & \text{otherwise} \end{cases} \tag{4.4}$$

where $d = |x_n - y_m|$ is the distance between the n^{th} atom of the upper layer and m^{th} atom of the lower layer. Here each chain is composed of N atoms and periodic boundary condition is applied by connecting the first and last beads in a unitcell having length $L = aN$. Equation (4.3) can be written in dimensionless form which involves parameter $\tilde{b} = b/ka$. This parameter describes strength of corrugation with respect to stiffness of springs.

In Fig 4.3(b) we present results of our calculations done by using parameters $\tilde{b} = 0.03$ and $N = 500$. To calculate the average friction force we start the system with certain initial center of mass velocity v_0 as shown in Fig 4.1(d). We also give random initial velocities which sum up to zero and obey the Maxwell distribution at dimensionless temperature T=0.5. Initial positions are randomly distributed in the same fashion. For certain values of v_0 we perform simulation of dynamics by integrating equation (4.3) for a short period of time. Then the same calculation is repeated several thousand times with different initial conditions until the average behavior can be described by a well behaving curve. For velocities above $v_0 = 0.1$ this curve is a line with a slope which gives the average friction force. Results of this calculations are shown by solid lines in Fig 4.3(b). For velocities below $v_0 = 0.1$ we find the variation of the average friction force by fitting the curve obtained from multiple simulations to $v_0 e^{-\gamma t}$ where γ determines the slope of the average friction force with respect to relative center of mass velocities. Results of this calculations are shown by dotted lines in Fig 4.3(b). At velocities higher than the sound velocity of atomic chains, the friction force decreases with a rate

which can fitted to an exponential decay function of velocity, as shown by green dashed lines in Fig 4.3(b). To reveal the physical mechanisms underlying the observed trend is left as a future work.

Chapter 5

Frictional Figure of Merit

In this chapter, we present our work on determination of frictional figure of merits for lubricants composed of single layers of graphane, fluorographene, molybdenum disulfide, and tungsten oxide.[33] We show that, due to stiff interlayer bonds and weak intralayer interactions these materials stay in continuous sliding regime even under very high loading pressures. The absence of mechanical instabilities leading to conservative lateral forces is also confirmed directly by the simulations of sliding layers. Remarkably, tungsten dioxide displays much better performance relative to others and heralds a potential superlubricant which is resistant to oxidation.

5.1 Motivation

Advances in atomic scale friction[20, 29, 30] have provided insight on dissipation mechanisms. The stick-slip phenomena is the major process, which contributes to the dissipation of the mechanical energy through sudden or non-adiabatic transitions between bi-stable states of the sliding surfaces.[24, 25, 31, 117] During a sudden transition from one state to another, the velocities of the surface atoms exceed the center of mass velocity sometimes by orders of magnitudes.[110] Local vibrations are created thereof evolve into the non-equilibrium system phonons via anharmonic couplings[53] within picoseconds.[118, 119] In specific cases, even a

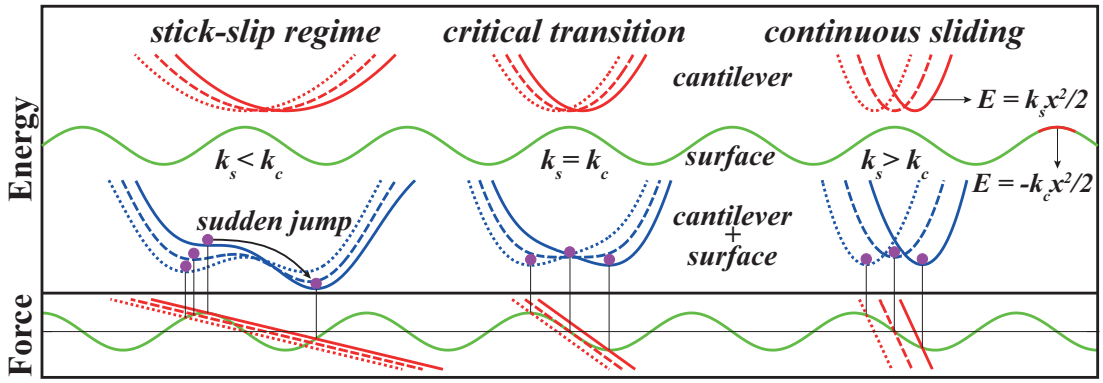

Figure 5.1: Schematic representation of stick-slip regime (left), critical transition (middle) and continuous sliding regime (right) in Prandtl-Tomlinson model. Upper part: the potential energy curves of the surface (green lines) and of the tip(+cantilever) (red lines) ; lower part: force variation of the surface (green lines) and of the tip (red lines). Blue lines represent the potential energy of the tip and surface. The magenta dot shows the position of the tip on the surface, while its other end is positioned at the minimum of the parabola shown with red lines in the upper part. The dotted, dashed and solid lines correspond to three different tip positions moving to the right.

second state in stick-slip can coexist.[117]

In Fig.5.1, two regimes of sliding friction are summarized within the framework of Prandtl-Tomlinson model,[24, 25, 110] where an elastic tip(+cantilever) moves over a sinusoidal surface potential. The curvature of this potential at its maximum gives the value of the critical stiffness k_c. If the intrinsic stiffness of the tip k_s is higher than this critical stiffness *i.e.* $k_s/k_c > 1$, the total energy of the tip-surface system always has one minimum. The sliding tip gradually follows this minimum, which results in the continuous sliding regime. Conversely, if the tip is softer than the critical value, then it is suddenly slipped from one of the bi-stable states to the other. This slip event can be activated by thermal fluctuations even before the local minimum point becomes unstable.[120] Experimentally, using friction force microscope, Socoliuc *et al.*[32] showed that the transition from stick-slip regime to continuous sliding attaining ultralow friction coefficient can be achieved by tuning the loading force on the contact.

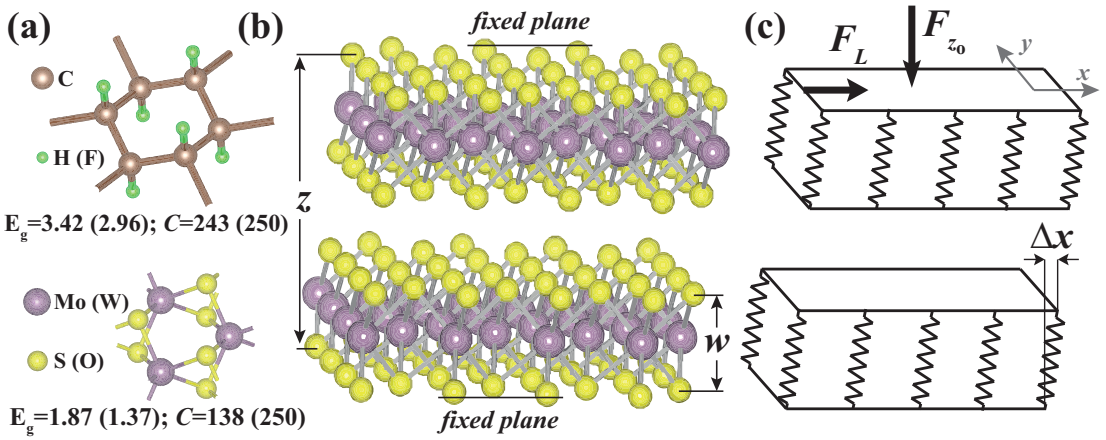

Figure 5.2: (a) Ball and stick model showing the honeycomb structure of graphane CH (fluorographene CF) (top) and MoS_2 (WO_2) (bottom). Calculated values of energy gaps E_g and in-plane stiffness C are also given in units of eV and J/m^2 respectively. (b) Two MoS_2 layers sliding over each other have the distance z between their outermost atomic planes. (c) Each layer is treated as a separate elastic block. Lateral F_L and normal (loading) F_{z_o} forces, the shear of bottom atomic plane relative to top atomic plane in each layer $\Delta x(y)$, and the width of the layer w, are indicated.

5.2 Layered Superlubricants

Here we investigate the sliding friction between two same pristine layers of nanostructures, such as graphane,[121, 122] fluorographene,[123, 124] molybdenum disulfide,[125] and tungsten dioxide,[126] (abbreviated according to their stoichiometry as CH, CF, MoS_2 and WO_2 respectively) using the Density Functional Theory.[1, 2] We find that these nanostructures avoid stick-slip even under high loadings and execute continuous sliding. Consequently, the sliding occurs without friction that would originate from the generation of non-equilibrium phonons. Our approach mimics the realistic situation, where the total energy and forces are calculated from first-principles as two-dimensional (2D) two layers undergo a 3D sliding motion under a constant (normal) loading force. This is the most critical and difficult aspect of our study. In this respect, our results provide a 3D rigorous *quantum mechanical* treatment for the 1D and empirical Prandtl-Tomlinson model.[24, 25]

The nanostructures considered in the present study are recently discovered insulators having honeycomb structure, which can form suspended single layers as well as multilayers. The unusual electronic, magnetic and elastic properties of these layers have been the subject of recent numerous studies. In particular, they have large band gaps to hinder the dissipation of energy through electronic excitation and have high in-plane stiffness ($C = (1/A)\partial^2 E_s/\partial\epsilon^2$, i.e. the second derivative of the strain energy relative to strain per unit area, A being the area of the unit cell).[124, 125, 126, 127] Analysis based on the optimized structure, phonon and finite temperature molecular dynamics calculations demonstrate that each suspended layer of these nanostructures are planarly stable.[122, 124, 125, 126] In graphane, positively charged three hydrogen atoms from the top side and another three from the bottom are bound to the alternating and buckled carbon atoms at the corners of hexagons in graphene to form a uniform hydrogen coverage at both sides (See Fig.5.2(a)). Recently synthesized CF [123] is similar to CH, but F atoms are negatively charged. Tribological properties of carbon based fluorinated structures have been the focus of interest.[128, 129] In the layers of MoS_2 or WO_2, the plane of positively charged transition metal atoms is sandwiched between two negatively charged outer S or O atomic planes. It was shown that MoS_2 structure can have ultralow friction.[130] Theoretically, the static energy surfaces are calculated during sliding at MoS_2(001) surfaces.[131] Apparently, the interaction energy between two single layers of these nanostructures is mainly repulsive due to charged outermost planes except very weak Van der Waals attractive interaction around the equilibrium distance. In Fig.5.2, each layer being a large 2D sheet consisting of three atomic planes mimics one of two sliding surfaces. In practice, sliding surfaces can be coated by these single layer nanostructures as one achieved experimentally.[132]

5.3 Methods

We have performed first-principles plane wave calculations within the Generalized Gradient Approximation (GGA) [133] including van der Waals corrections [134] using PAW potentials [67]. All structures have been treated within supercell

geometry using the periodic boundary conditions. A plane-wave basis set with kinetic energy cutoff of 400 eV and 500 eV is used for transition metal and carbon based structures respectively. In the self-consistent potential and total energy calculations the BZ is sampled by (10×18×1) for graphane and was scaled in this manner for other structures. All atomic positions and lattice constants are optimized by using the conjugate gradient method where total energy and atomic forces are minimized. The convergence for energy is chosen as 10^{-5} eV between two steps, and the maximum force allowed on each atom is less than 10^{-4} eV/Å. Numerical plane wave calculations have been performed by using VASP package.[18, 19]

5.4 Critical Curvature

We consider two layers of the same nanostructures in relative motion, where the spacing z between the bottom atomic plane of the bottom layer and the top atomic plane of the top layer is fixed. Here the frictional behavior of the system is dictated mainly by C-H(F), Mo-S and W-O bonds and their mutual interactions. These layers are represented by periodically repeating rectangular unit cells. We calculate the value of the equilibrium lattice constants, which increase as z decreases. For each value of z the fixed atomic layer at the top is displaced by x and y on a mesh within the quarter of the rectangular unitcell. Then all possible relative positions (displacements) between fixed atomic layers are deduced using symmetry. At each mesh point all atoms of the system except those of fixed top and bottom planes are relaxed and the total energy of the system $E_T(x, y, z)$ (comprising both layers) is calculated. We have also derived $\Delta x(x, y, z)$ and $\Delta y(x, y, z)$ data which correspond to the shear (deflection) from the equilibrium position of the relaxed atomic planes relative to the fixed atomic plane of the same layer as illustrated in Fig.5.2(c). The matrices of these data are arranged for each nanostructure using the mesh spacing of ~ 0.2 $\mathring{A}$ in x and y directions. The forces exerting on the displacing top layer in the course of relative motion of layers are calculated from the gradient of the total energy of the interacting system, namely $\vec{F}(x, y, z) = -\vec{\nabla} E_T(x, y, z)$ at each mesh point (x, y).

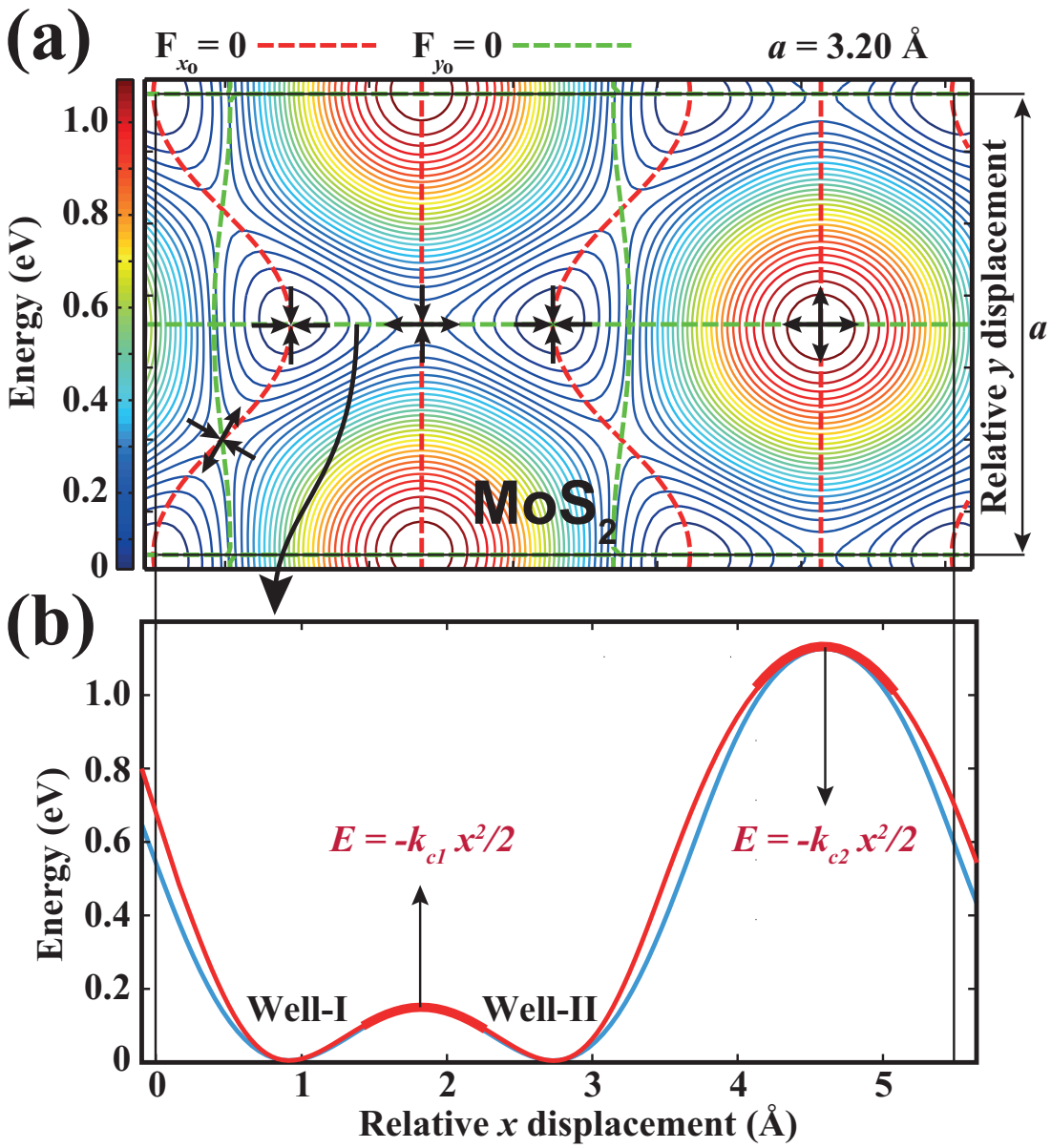

Figure 5.3: (a) The contour plot of interaction energy E_I of two sliding layers of MoS_2. The zero of energy is set to $E_I[0, 0, z_o(0, 0)]$. The energy profile is periodic and here we present the rectangular unitcell of it. The width of this unitcell in y-direction is equal to the lattice constant a of the hexagonal lattice. Forces in x- (y-) direction is zero along the red (green) dashed lines, respectively. There are several points at which the lateral force $\vec{F_L}$, is zero. The arrows at these critical points indicate the directions where the energy decreases. (b) The energy profiles of E_I (blue line) and E_I^o (red line) along the horizontal line with $F_y = 0$ for MoS_2. Loading pressure in all cases is σ_N=15 GPa.

These forces are in agreement with the resultant of the atomic forces calculated for the top layer using Hellman-Feynman theorem. Eventually, the matrices of all data, namely $E_T(x,y,z)$, $\Delta x(x,y,z)$, $\Delta y(x,y,z)$ and $\vec{F}(x,y,z)$ are made finer down to mesh spacing of ~ 0.05 $\mathring{A}$ using spline interpolation.

The properties affecting the friction between layers should be derived under a given constant loading force. First of all we preset the value of applied loading, F_{z_o}, which corresponds to the operation pressure when divided by the cell area A, namely $\sigma_N = F_{z_o}/A$. We obtain the normal force from $F_z(x,y,z) = -\partial E_T(x,y,z)/\partial z$ and for each x and y we calculate the value of z where $F_z(x,y,z) = F_{z_o}$ and abbreviate it as $z_o(x,y)$. Then by using spline interpolation in z direction we calculate the x and y dependence of $F_{x_o}[x,y,z_o(x,y)]$ and $F_{y_o}[x,y,z_o(x,y)]$, as well as $\Delta x_o[x,y,z_o(x,y)]$ and $\Delta y_o[x,y,z_o(x,y)]$ for a given F_{z_o}. The lateral force is then $\vec{F}_L[x,y,z_o(x,y)] = F_{x_o}\hat{i} + F_{y_o}\hat{j}$. Integrating the lateral force over the rectangular unitcell we obtain,

$$E_I[x,y,z_o(x,y)] = \int_0^x \int_0^y \vec{F}_L(x,y,z_o(x,y)) \cdot \mathrm{d}\vec{r} \tag{5.1}$$

where $E_I[x,y,z_o(x,y)]$ is the interaction energy for displacement (x,y) in the cell under applied constant loading force F_{z_o}. It should be noted that E_I is different from $E_T(x,y,z)$ (but $E_I \to E_T$ for $z >> 1$) and is essential to reveal the friction coefficient. Contour plots of E_I of two sliding MoS_2 layers calculated for σ_N=15 GPa are shown in Fig.5.3(a) and those of CH, CF, WO_2 in Fig.5.4(a). The profile of E_I is composed of hills arranged in a triangular lattice. These hills correspond to the relative positions when the charged atoms of adjacent layers have the minimum distance. The hills are surrounded by two kind of wells. The difference between these two wells is enhanced with increasing pressure. The wells form a honeycomb structure and are connected to each other through the saddle points (SP). When the layers are moved over each other they will avoid the relative positions corresponding to the hills. For example, if the layers are pulled in the y-direction they will follow the curved $F_x = 0$ path passing through the wells and SP but not the straight one passing through the hills as shown in the Fig.5.3(b). This makes SP very important because moving from one well to the adjacent one requires to overcome the barriers at these points. We note that the critical stiffness can be calculated from the curvature of E_I^o, which is

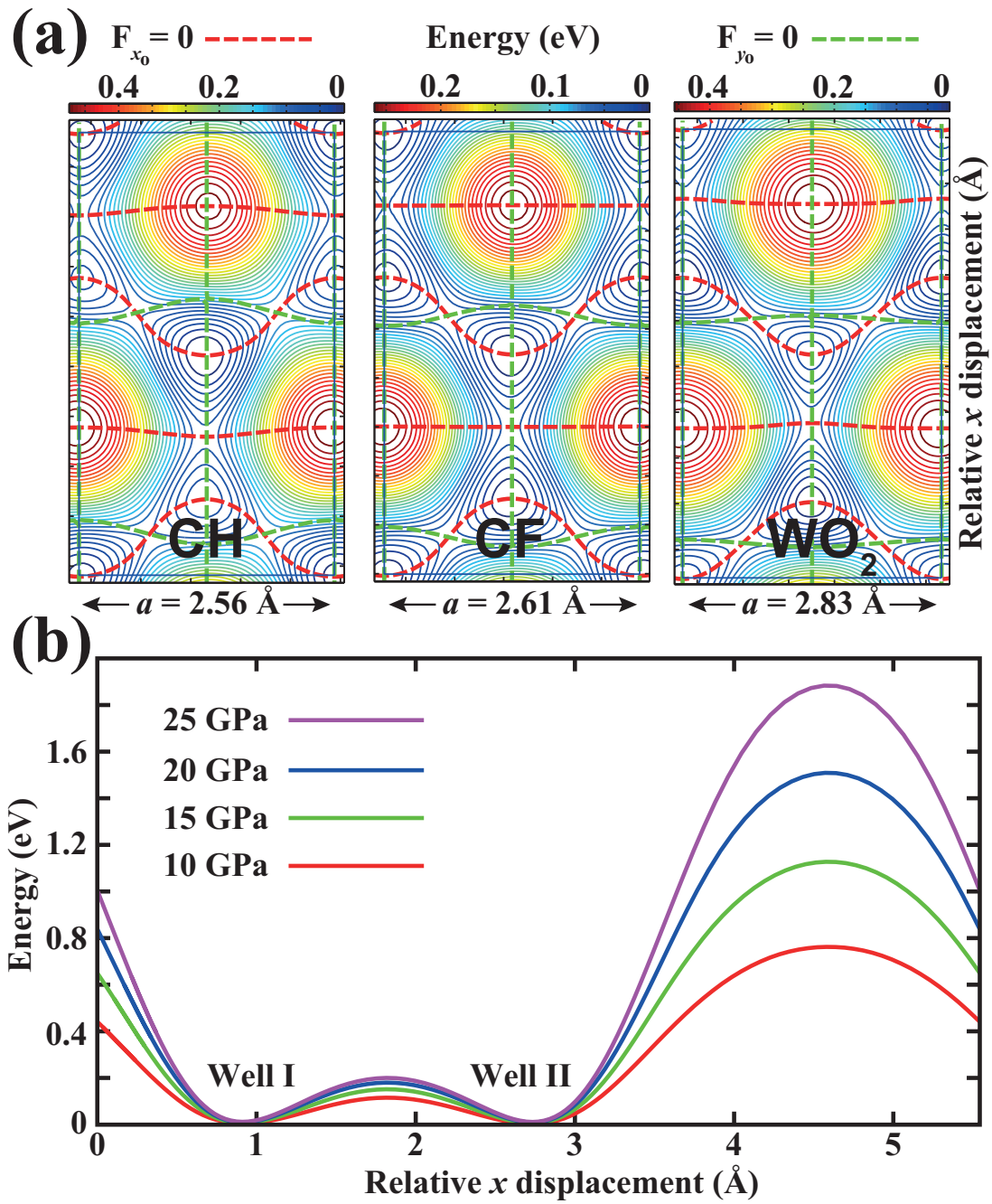

Figure 5.4: (a) Contour plots of interaction energy E_I of two layers of CH, CF, and WO_2 executing sliding motion under constant loading pressure are presented in their rectangular unit cells. The zero of energy is set to $E_I[0, 0, z_o(0, 0)]$. Loading pressure in all cases is σ_N=15 GPa. (b) Variation of interaction energy E_I^0 with applied loading for MoS_2 structure along the straight $F_y = 0$ line passing through two wells, saddle point and one hill.

obtained by subtracting the strain energies of two sliding MoS_2 layers, namely $E_I^o = E_I - k_s(\Delta x_o^2 + \Delta y_o^2)$ and by replacing x by $x - 2\Delta x_o$. While the SP serves as a barrier in the direction joining the nearby wells it acts as a well in the perpendicular direction joining the hills. Since we are interested in the curvature of the SP in the former direction we have made a plot along the $F_y = 0$ line which passes through the hill, the wells and the SP in between as shown in the Fig.5.3(b). We derive two critical stiffness values from E_I^o curve for a given normal loading force; namely k_{c1} at the SP and k_{c2} at the hill by fitting the curve at the maxima of the barriers to a parabola. Although the hills will be avoided during sliding motion the curvature at these points are calculated for completeness. We also present the variation of E_I^0 with applied loading for MoS_2 structure in Fig.5.4(b). Note that, the variation of the amplitude at the saddle point is minute. In Fig.5.5(b) the variation of k_{c1} and k_{c2} of CH, CF, MoS_2 and WO_2 with loading pressure σ_N is presented. Generally, the critical stiffness, in particular k_{c1} is low due to repulsive interaction between sliding layers. This facilitates the transition to continuous sliding.

5.5 Intrinsic Stiffness

Next we calculate the intrinsic stiffness k_s of individual MoS_2 layers using the force and the displacement data. For each x and y the lateral forces $F_{x_o}[x, y, z_o(x, y)]$ and $F_{y_o}[x, y, z_o(x, y)]$ versus the displacements $\Delta x_o[x, y, z_o(x, y)]$ and $\Delta y_o[x, y, z_o(x, y)]$, respectively are plotted. As shown in Fig.5.5(a), this data falls on a straight line having a negative slope as expected from Hook's law of elasticity. We note that the elastic properties of layers having honeycomb structure is uniform and is independent of the direction of displacement and force.[127] The magnitude of the slope, $k_s = -F_{x(y)_o}/\Delta x(y)_o$ gives us the stiffness of the layers. Note that, normally the stiffness is defined as stress over strain and has units of energy per volume. Here we only need the ratio of material stiffness to the critical stiffness and should have the same units. The critical stiffness was calculated as second order spatial derivative of energy in the unitcell and it has units of energy per unitcell per unit area. As defined above, the stiffness of layers, k_s, also has

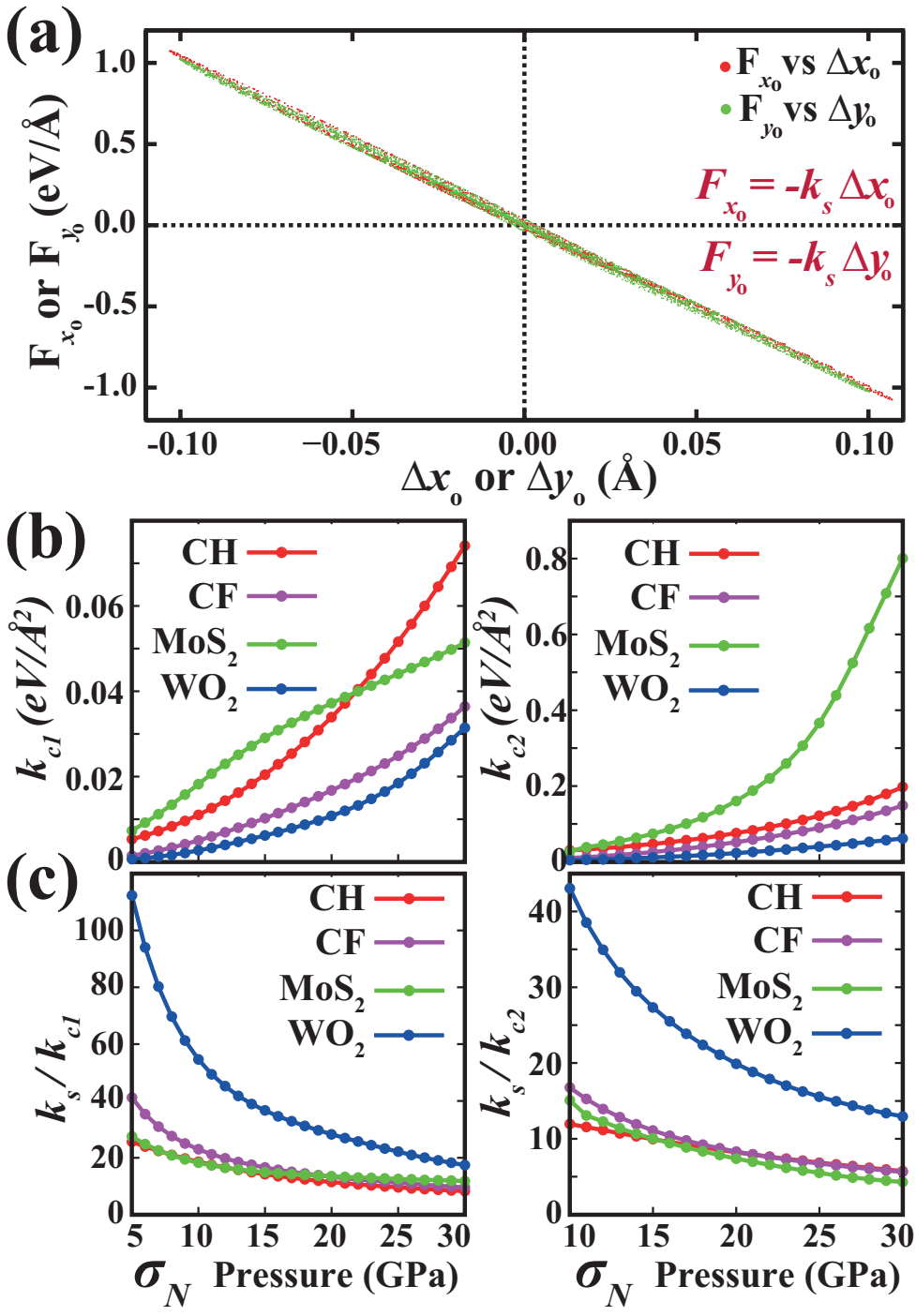

Figure 5.5: (a) The force versus shear values along x- and y-directions for each mesh point by red and green dots, respectively. (b) The variation of k_{c1} and k_{c2} with loading pressure. (c) The variation of the frictional figures of merits k_s/k_{c1} and k_s/k_{c2}, with loading pressure calculated for CH, CF, MoS_2 and WO_2.

units of energy per unitcell per unit area. Calculated intrinsic stiffness values of CH, CF, MoS_2 and WO_2 in the range of σ_N from 5GPa to 30 GPa are found to be 6.15±0.15 eV/Å^2, 4.5 eV/Å^2, 10.0±0.3 eV/Å^2 and 15.2±0.3 eV/Å^2, respectively. Clearly, these values of k_s, in particular those of MoS_2 and WO_2 are rather high.

5.6 Frictional Figure of Merit

Based on the discussion at the beginning, the ratios k_s/k_{c1} and k_s/k_{c2} give us a dimensionless measure of performance of our layered structures in sliding friction. When these ratios are above two (since both layers in relative motion contribute), the stick-slip process is replaced by continuous sliding, whereby the dissipation of mechanical energy through phonons is ended. Under these circumstances the friction coefficient diminish, if other mechanisms of energy dissipation were neglected. For this reason one may call these ratios as a frictional figures of merit of the layered materials. In Fig.5.5(c) we present the variations of the ratios k_s/k_{c1} and k_s/k_{c2} with normal loading forces. Even for very large σ_N, $k_s/k_{c1} > 2$ and $k_s/k_{c2} > 2$. For usual loading pressures, the stiffness of MoS_2, CF and CH is an order of magnitude higher than corresponding critical values. Interestingly, for WO_2 this ratio can reach to two orders of magnitudes at low pressures. The absence of mechanical instabilities has been also tested by performing extensive simulations of the sliding motion of layers in very small displacements. C-H, C-F, Mo-S and W-O bonds in each case of two layers in relative motion under significant loading force did not display the stick-slip motion.

5.7 Stick-Slip in Silicane: A Counter Example

Conversely, we now examine the sliding of two silicane [135, 136] layers (abbreviated as SiH and composed of silicene [44] saturated by hydrogen atoms from both sides, like graphane) with $k_s = 2.1 \pm 0.1$ eV/$\mathring{A}^2$ for 2 GPa $\leq \sigma_N \leq$ 8 GPa. This is an interesting material because the onset of stick-slip occurs already at

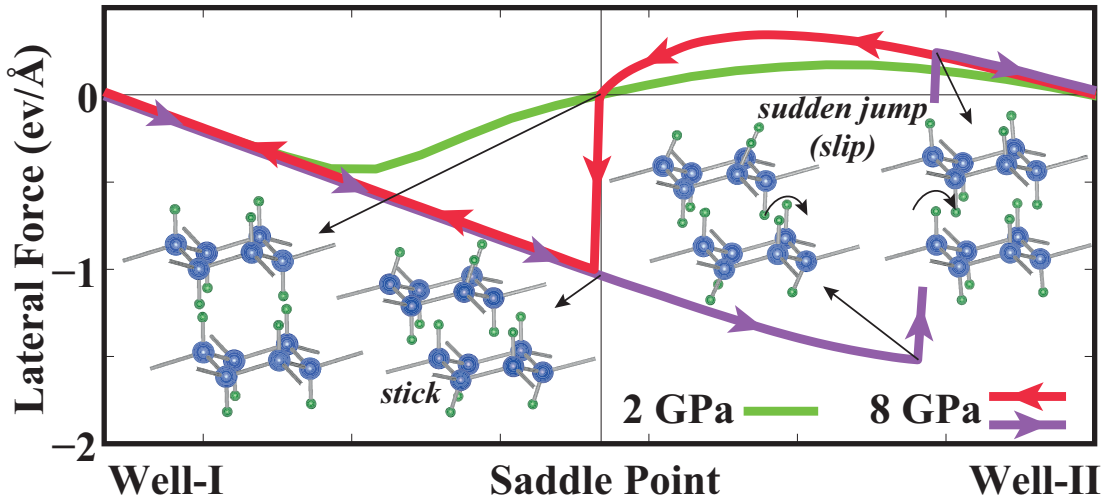

Figure 5.6: Calculated lateral force variation of two single layer SiH under two different σ_N. The top layer is moving to the right or to the left between two wells. Atomic positions of two SiH layers in stick and slip stages are shown by inset. The movement of SiH layers under loading pressure of $\sigma_N = 8$ GPa is presented as a supplemental material of our work.[33]

low loading pressures and exhibits a pronounced asymmetry in the direction of sliding between two wells. In Fig.5.6 we present the lateral force variation calculated for two different loading pressures. For small loading pressure, σ_N=2 GPa the stick-slip is absent since approaching the SP from Well-I, the curvature is $k_{c,I} = 0.28$ eV/$\mathring{A}^2$ and from Well-II it is $k_{c,II} = 0.16$ eV/$\mathring{A}^2$, thus $k_s/k_{c,IorII} > 2$ for both directions. Whereas, once the pressure is raised to σ_N =8 GPa stick-slip already governs the sliding friction, since $k_{c,I}$ reaches 1.38 eV/$\mathring{A}^2$. Interestingly, since $k_{c,II}$ is only 0.28 eV/$\mathring{A}^2$ for σ_N =8 GPa, going from Well-II to Well-I a slip event occurs at SP. Eventually, one sees in Fig.5.6 a hysteresis in the variation of F_L leading to energy dissipation.

5.8 Discussions

Earlier, the sliding motion of the diamond like carbon coatings exposed to hydrogen plasma resulted in a very low friction coefficient.[137] Ultralow friction

was attributed to repulsive Coulomb forces between DLC films facing each other in sliding. However, when exposed to open air in ambient conditions, positively charged H atoms was replaced by negatively charged O and hence the uniformity in the charging was destroyed. In the present study, graphane coating is reminiscent of the hydrogenated DLC and accordingly is found to have ultralow friction, but vulnerable to degradation by oxygen atoms. Unlike graphane coating, WO_2 coating consists of negatively charged oxygens and hence immune to oxidation.

In conclusion, using a criterion for the transition from stick-slip to dissipationless continuous sliding regime, which is calculated from the first-principles, we showed that two sliding layered nanostructures, such as CH, CF, MoS_2 and WO_2, execute continuous sliding with ultralow friction. The minute variation of the amplitude of the interaction potential due to the repulsive interaction, as well as stiff C-H(F), Mo-S and W-O bonds underlie the frictionless sliding predicted in the present study. Our predictions put forward an important field of application as ultralow friction coating for the layered honeycomb structures, which can be achieved easily to hinder energy dissipation and wear in sliding friction.

Chapter 6

Superlubricant Graphene Layers

In this chapter, the frictional properties of structures composed of graphene layers are presented. Two layers of graphene is shown to be enough to screen the strong interaction between Ni(111) surfaces, which have negligible mismatch with graphene structure. The trends observed in the corrugation potential with increasing number of graphene layers are in accordance with recent experiments, however the reason for this observation might be different.

6.1 Motivation

Superlubricant materials composed of weakly interacting two-dimensional (2D) layers have been a central figure of intense studies in tribology. Bulk counterparts of molybdenum disulfide and graphene were used as a solid lubricant in industrial applications long before the 2D layers constituting them were isolated. The key features which make these materials so important in friction science are strong covalent intralayer bonds in contrast to weak van der Walls interlayer interactions. As discussed in Chapter 5, the contrast between these intralayer and interlayer interactions can be quantified in terms of frictional figure of merit.[33]

Experimental and theoretical studies have shown that friction force between

graphite layers can be very small when the layers are slid with a certain angle to each other.[138, 139] In this case the rotated layers are incommensurate with respect to each other and the corrugation potential between such layers is flat. It was shown that, the torque felt by rotated layers can twists them until the layers become commensurate which increases the friction force.[140] Transition between commensurate and incommensurate states of graphene flakes on graphite was investigated in detail by several theoretical studies.[141, 142, 143]

Recently, several experimental works investigated the variation in friction force when the number of 2D layers are varied from single layer to many layers representing the bulk structure.[144, 145, 146] Lee *et al.* used friction force microscope with a SiN tip to investigate atomic friction on graphite and graphene flake prepared on silicon oxide layer.[144] They have found that friction on graphene was lower than on silicon oxide but higher than that on graphite. Their results show that friction force monotonically decreases as the number of graphene layers are increased and approaches the bulk value found for graphite. They have attributed this trend to long ranged van der Walls interactions between layers.

Filleter *et al.* used atomic force microscope with cantilevers coated in a polycrystalline diamond film and found that friction force on single layer graphene epitaxially grown on SiC is lower than that on SiC surface but higher than bilayer graphene on SiC.[145] In contrast to other works, they have found the friction force to be higher on graphite compared to bilayer graphene. They have found the similar trends when oxidized single crystal silicon cantilevers with sharper tips were used. They assert that, the lower friction measured in bilayer graphene is related to suppressed electron-phonon coupling which plays important role in dissipation.

Much recently, the variation of friction force with number of layers was investigated for structures composed of graphene, molybdenum disulfide, niobium diselenide and hexagonal boron nitride layers.[146] Similar to results of Lee *et al.*, it was found that the friction force decreases as the number of layers increase. It was also found that, this trend continues to be observed in suspended layers while

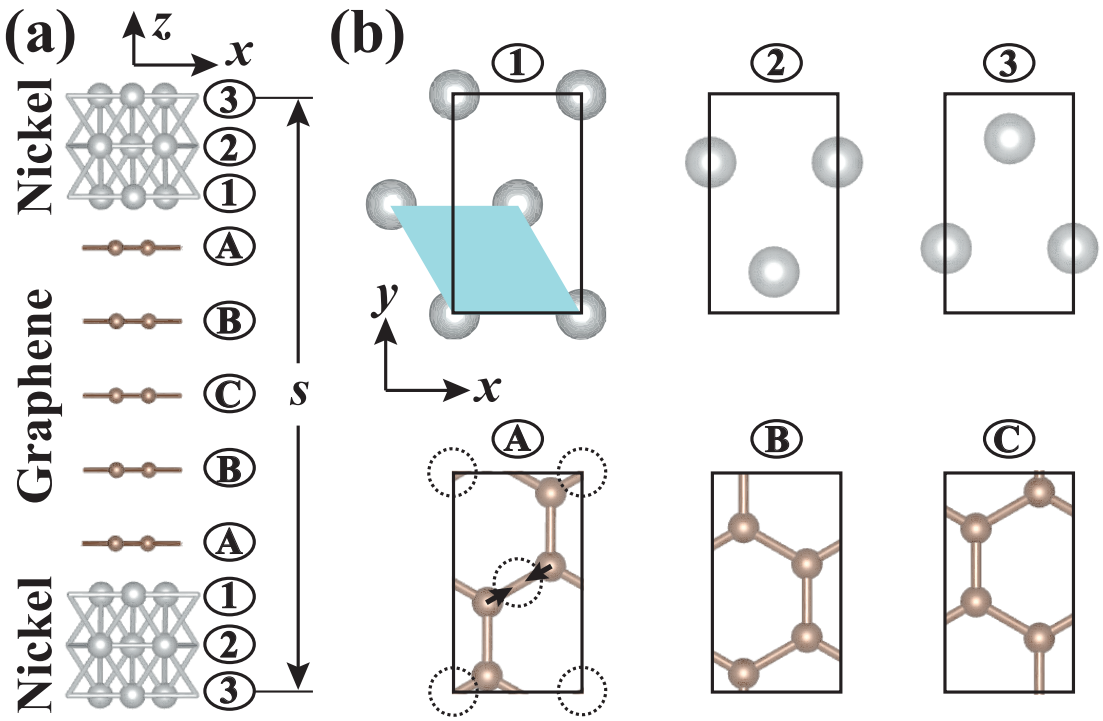

Figure 6.1: (a) Side view of the arrangement of the Ni-ABCBA-Ni structure. The outermost Ni(111) atomic planes are fixed at the separation s. (b) Top view of individual layers constructing the Ni-ABCBA-Ni structure. The primitive unitcell is shown by blue shaded area. Dotted circles represent optimized positions of Ni atoms below the graphene layers in configuration A.

it is suppressed when graphene layers are deposited on highly adherent mica surface. Here the observed trend was attributed to higher compliance of thin layers to perpendicular stress. Together with finite element simulations they show that as the tip is slid over, the layers are puckered and piled up in direction of sliding, which increases the contact area and resistance to sliding. The puckering is more pronounced when the number of layers are decreased. Due to similar reasons, the trend is suppressed in mica because it prevents graphene layers from puckering.

The potential of graphene as a lubricant material can be revealed realistically, when it is placed between two flat sliding surfaces. In this chapter we investigate the energy dissipation and the strength of the potential corrugation between two Ni(111) surfaces having $n = 0-5$ layers of graphene in between. We treat infinite

surfaces using periodic boundary conditions, which also minimizes effects such as puckering or rippling.[146] Our approach mimics a realistic situation where the metallic surfaces are coated by lubricant layers and the radii of asperities are much larger compared with atomic scales. The interaction energy, as well as lateral forces are calculated using quantum mechanical treatments as 2D layers execute a 3D sliding motion under a given constant normal force. We found that strong adhesive forces between Ni(111) surfaces, which lead to strong energy dissipation and wear are substantially suppressed when a single layer of graphene is inserted between the surfaces. However, the system enters into the continuous sliding regime only after the second layer of graphene is inserted, whereby each graphene layer becomes attached to one Ni(111) surface. Even more interesting is that inserting more graphene layers between Ni(111) surfaces decreases the friction gradually. On the other hand, the friction between graphene layers sliding over each other are larger and practically independent of the number of layers n in between, when the supporting Ni surfaces are not present. These results reveal the capacity of graphene as a superlubricant leading to nearly frictionless sliding and are explained by a charge exchange mechanism between graphene and Ni slabs.

6.2 Atomic Structure

The frictional properties of graphene layers sandwiched between Ni(111) surfaces and those of bare graphenes are treated using the models described in Fig. 6.1. In all calculations sliding nickel surfaces are represented by slabs consisting of three atomic layers of bulk Ni. We apply periodic boundary conditions along the plane parallel to the surfaces with a primitive unitcell comprising one Ni and two C atoms in each layer. The interaction between periodic images of Ni slabs is hindered by introducing a vacuum spacing of 15 Å. The structure presented in Fig. 6.1(a) is named as Ni-ABCBA-Ni structure, where A, B, and C correspond to certain in-plane configuration of carbon atoms. To avoid any confusion the atomic layers comprising the Ni slabs are arranged in a mirror symmetry. This arrangement is presented in Fig 6.1(a), while the in-plane configuration of Ni

and C atoms in each plane is shown in Fig. 6.1(b). Nickel atoms positioned at the bridge sites of graphene structure attracts C atoms and slightly breaks the honeycomb symmetry, as shown in Fig. 6.1(b). The nature of this interaction is discussed in forthcoming parts in detail. The equilibrium positions of Ni and C atoms are attained by structure optimization at a given constraint.

6.3 Methods

We have performed first-principles plane wave calculations within the Generalized Gradient Approximation (GGA) [133] including van der Waals corrections [134] using PAW potentials [67]. A plane-wave basis set with kinetic energy cutoff of 500 eV is used. In the self-consistent potential and total energy calculations the BZ is sampled by (13×13×1) k-points. All atomic positions and lattice constants are optimized by using the conjugate gradient method where total energy and atomic forces are minimized. The convergence for energy is chosen as 10^{-5} eV between two steps, and the maximum force allowed on each atom is less than 10^{-4} eV/Å. Numerical plane wave calculations have been performed by using VASP package.[18, 19]

6.4 Adhesion Hysteresis

We start our analyses by calculation of forces on outermost atoms of Ni slabs when they are kept fixed during the relaxation while the separation, s, between them (see Fig. 6.1(a)) is gradually varied. We start by two Ni slabs each composed of three atomic layers with no graphene in between. The dashed green curve shown in Fig. 6.2(a) is obtained when s is gradually decreased. One can observe a slightly attractive region followed by a sudden increase in the attractive force after which the force starts to decrease until the equilibrium distance is reached and the force becomes repulsive. During the sudden increase in attractive force both layers are elongated towards each other and after this stage the distance

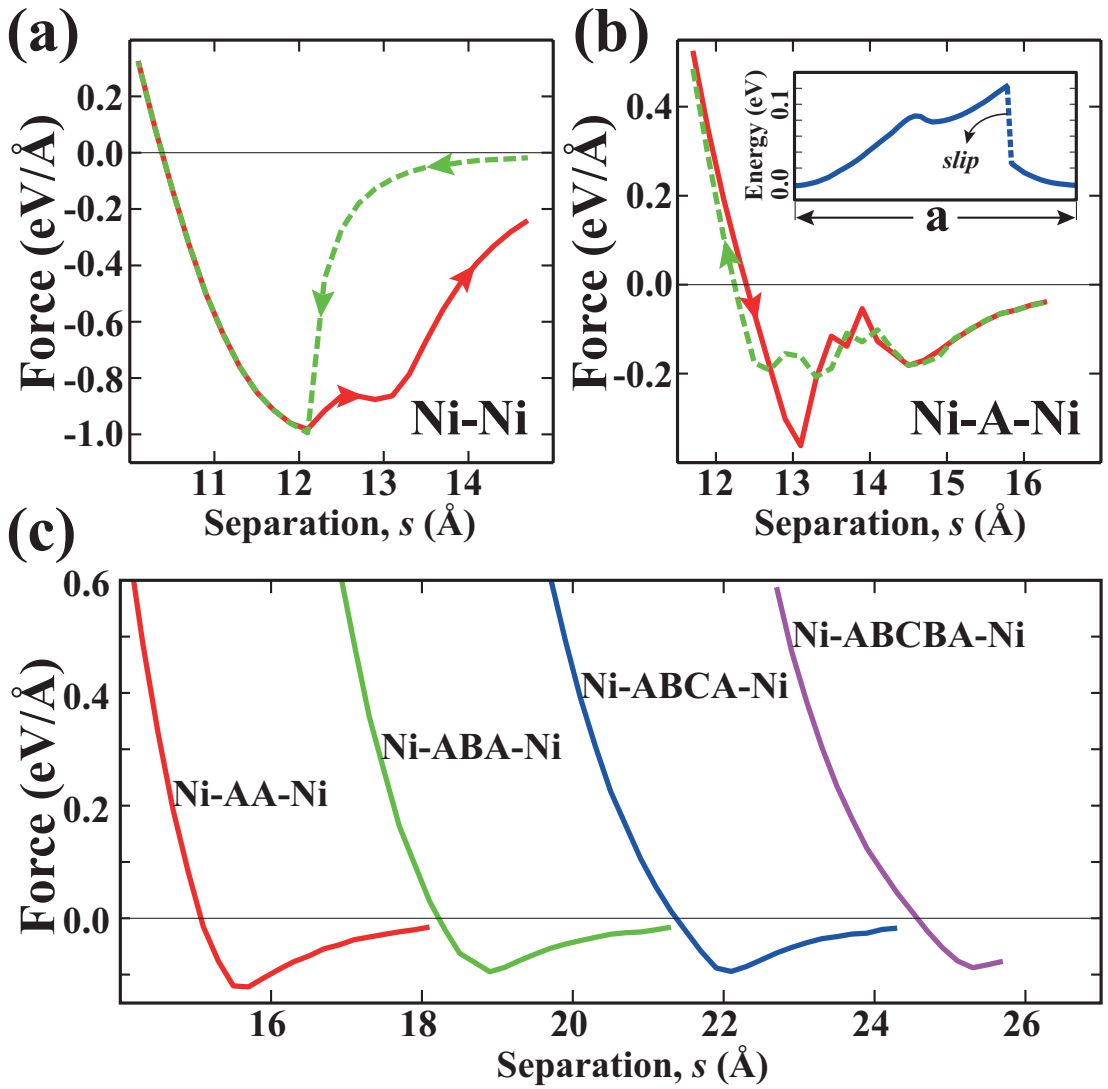

Figure 6.2: Adhesion hysteresis curves for (a) Ni-Ni and (b) Ni-A-Ni structures and its stick-slip behavior shown by inset. (c) Normal force along z axis as a function of separation s for Ni-graphene-Ni structures with 2-5 graphene layers.

between the facing atomic layers remain nearly constant until the equilibrium is reached. The red solid line in Fig. 6.2(a) shows the variation of forces when s is gradually increased. This time, the curve takes a different route right at the point where the sudden increase of the attractive force was observed. When s is increased further the facing two layers detach from the slabs and attach to each other. The observed hysteresis manifests the adhesion and wear phenomena frequently observed between metallic contacts.

Next we insert one graphene layer in the minimum energy configuration A described in Fig. 6.2(b) between two Ni slabs. This graphene layer screens the interaction between Ni surfaces and significantly decreases the attractive potential between them, however the hysteresis is still present, as seen in Fig. 6.2(b). We also observe stick-slip behavior when the Ni slabs are laterally moved relative to each other with one layer graphene in between making sudden jumps. As illustrated by inset in Fig. 6.2(b), the sudden variation of energy in constant height mode demonstrates the presence of stick-slip motion causing the dissipation of mechanical energy.

When the second graphene layer is inserted, each layer becomes attached to Ni(111) surface. Under these circumstances the hysteresis is completely removed and the attractive forces are weakened. Further increasing the number of layers shows minor changes as seen in Fig. 6.2(c). From these observations we deduce that, inserting single layer graphene can protect the Ni layer from wear during sliding, however one layer is not enough for the onset of the continuous sliding regime. It becomes possible only by including a second layer of graphene whereby each Ni slab is coated by graphene.

6.5 Trends and Discussions

To investigate the effect of including more layers on the potential corrugation during the sliding of the layers under constant pressure, we first calculate the total energies E_T when outermost Ni layers are kept fixed at various relative lateral

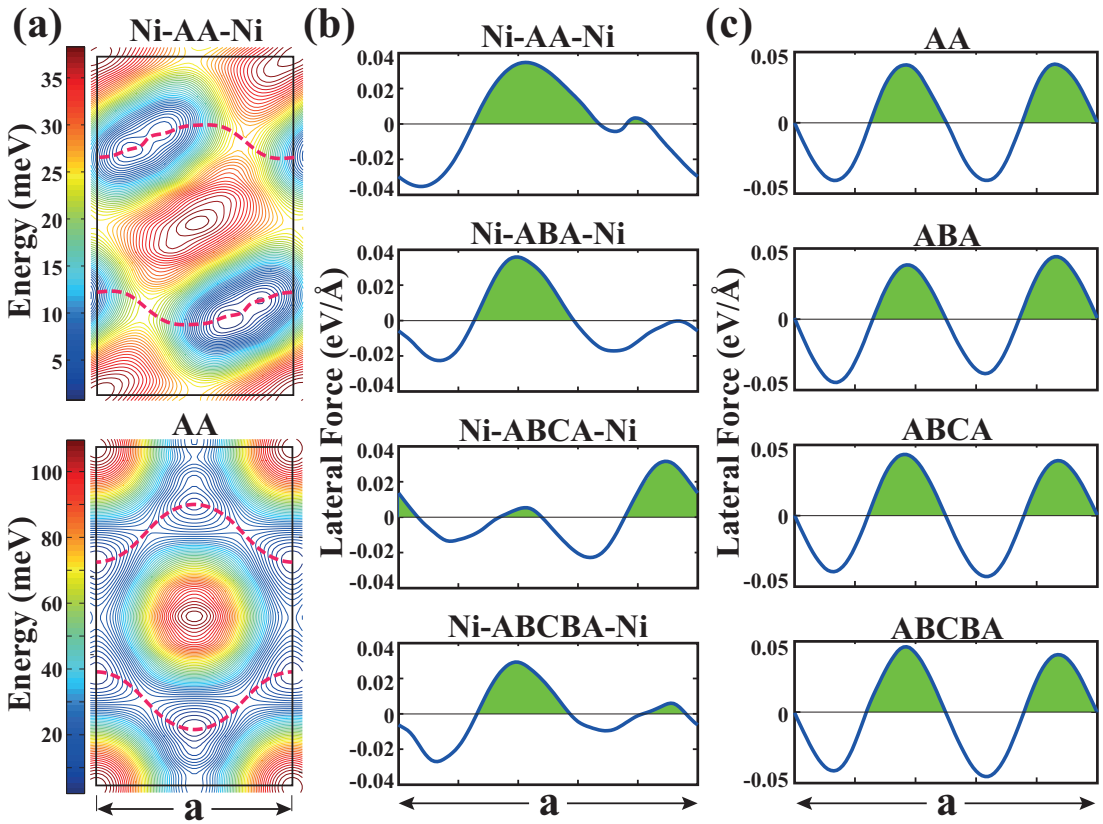

Figure 6.3: (a) Profiles (contour plots) of potential corrugation for Ni-AA-Ni and AA [without Ni(111) slabs] structures calculated for constant pressure of 7 GPa. The paths along which one slab moves in the course of sliding when pulled along x axis are shown by red dashed lines. The lattice constant of the unit cell is indicated by **a**. (b) Variation of lateral force F_x along x-axis during sliding of Ni-AA-Ni structures over the path shown in (a). The sum of areas shaded in green is defined as the corrugation strength W_D (see text). (c) Same as (b) for sliding AA structures without Ni(111) slabs.

(x, y) positions and at fixed separation s.[33] These calculations are performed in a 3D grid of x, y, s. The distances between the data points were taken to be $\sim$ 0.2 Å in the lateral plane and 0.2 Å in perpendicular axis *i.e* s, which is then made finer down to ~ 0.05 Å by spline interpolation. We also generate F_x, F_y and F_z matrices from the gradient of the total energy $F_{x,y,z} = -\partial E_T(x, y, z)/\partial x, y, z$, which is consistent with Hellmann-Feynman forces calculated on fixed atoms of outermost planes. We then retrieve F_x and F_y corresponding to a given F_z (normal pressure) at each (x, y) in the unit cell and generate the profiles of potential corrugation from $\int F_x dx + F_y dy$, where the minimum of total energy is set to zero. The profiles (contour plots) of potential corrugation calculated for Ni-AA-Ni and AA i.e. two flat graphene layers without Ni(111) are shown in the top and bottom panels of Fig. 6.3(a), respectively. We note that the amplitude of the potential corrugation (i.e. the difference between the minimum and maximum of energy) is an order of magnitude smaller compared to single-layer honeycomb structures of graphane CH, fluorographene CF, MoS_2 and WO_2 discussed in Chapter 5. On the other hand, the intrinsic stiffness of the present case, which is related to the interaction between Ni and graphene layers is also substantially lower ($k_s = 0.8$ eV/A^2) compared to the intrinsic stiffness of those honeycomb structures.[33] The lower intrinsic stiffness accompanied by low potential corrugation curvature results in a frictional figure of merit of ~ 10, at constant pressure of 7 GPa, which is enough to keep the system in continuous sliding regime. Comparing the profiles of the potential corrugation of Ni-AA-Ni and AA structures, one can see how the interaction between graphene layers is affected by their interaction with Ni surfaces. The effect of distortion presented in Fig. 6.1(b) is reflected to the potential corrugation of Ni-AA-Ni, since its symmetry is changed from hexagonal to rectangular. Also note that, the amplitude of the potential corrugation is substantially lowered when Ni slabs are present, which reveals an important effect of substrate (i.e. Ni(111) surface).

To set a measure for the corrugation strength we first derive the path at which the upper slab would slide if it was pulled along x-axis. This path is shown by dashed lines in Fig. 6.3(a) for the case of Ni-AA-Ni. In the case of structures having more than two graphene layers the path is found directly by starting from

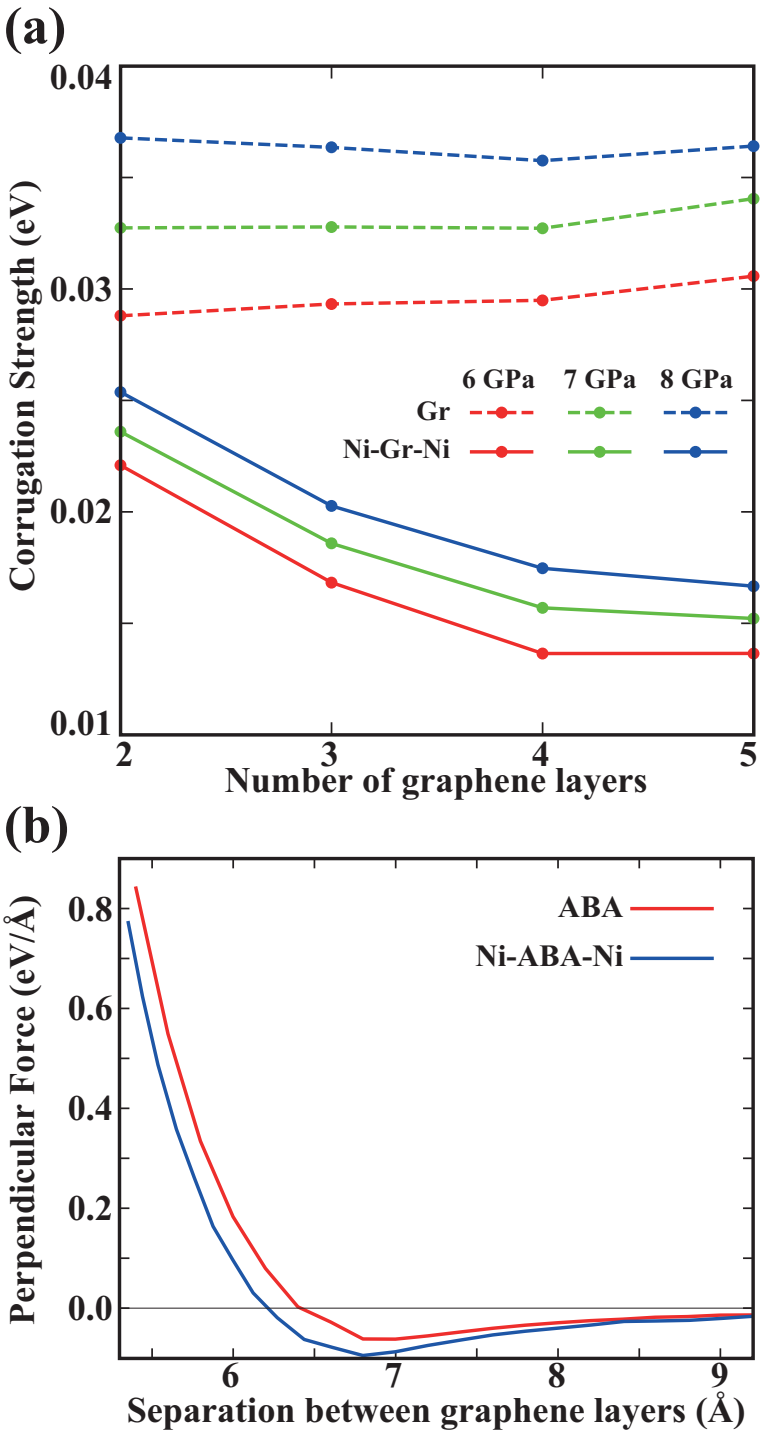

Figure 6.4: (a) Variation of the corrugation strength with number of layers as a function of applied loading pressure for n number of graphene layers (with and without Ni(111) substrates). (b) Perpendicular force F_z versus the separation distance between outermost graphene layers for Ni-ABA-Ni and ABA structures (n=3). In the repulsive range, the perpendicular force and hence the potential corrugation is larger in the absence of Ni(111) slabs.

the Ni slab positions presented in Fig. 6.1 and moving along the x-axis while minimizing the total energy along y axis. Then we calculate the lateral force F_x along x-axis felt by the slab, as shown in Fig. 6.3(b). Here we note that in the sliding of Ni(111) slabs having n graphene layers the dissipation of energy through non-equilibrium phonons generated by sudden processes is hindered for $n \geq 2$ and hence $W = \int_0^a F_x dx$ vanishes. This, however, does not precludes energy dissipation through other mechanisms. With a premise that the maximum of the energy to be dissipated by any mechanism should be smaller than $W_D = \int_0^a F_x^> dx$ i.e the integral of all positive work done during sliding of one slab over one unitcell shown by the green shaded region in Fig. 6.3(b), we took W_D as a measure for the corrugation strength. The result of these calculations are presented in Fig. 6.3(b). Note that W_D (is also related to kinetic friction coefficient $\mu_k = (W_D/a)/F_z$) is already very small. To check the effect of the type of stacking we have also calculated the force variation for Ni-ABABA-Ni structure and the result was very close to that of Ni-ABCBA-Ni structure. For comparison, we have performed the same calculations for graphene layers in the same stacking but without Ni slabs above. The results of these calculations are presented in Fig. 6.3(c).

Various important trends in the corrugation strength W_D, obtained from above calculations are presented in Fig. 6.4 (a). As expexted the corrugation strength increases with increasing normal force. Also the corrugation strength is higher in structures composed of only graphene layers (like ABA) compared to the ones having Ni slabs (like Ni-ABA-Ni). This effect is mirrored in the repulsive interaction of graphene layers in the presence and absence of Ni slabs, as shown in Fig. 6.4 (b). Here one can see that introducing Ni slabs decreases the repulsive interaction between graphene layers, which is consistent with decrease in the corrugation strength discussed above. Another important finding is that corrugation strength of the structures solely composed of graphene layers has minor variation with the number of layers. On the other hand, the corrugation strength is significantly decreased when the number of graphene layers in Ni-graphene-Ni structures are increased. This trend is seemingly in accordance with experimental observations.[144, 146] However, as mentioned above, the system at hand is very different from those considered in the experiments and the trends revealed

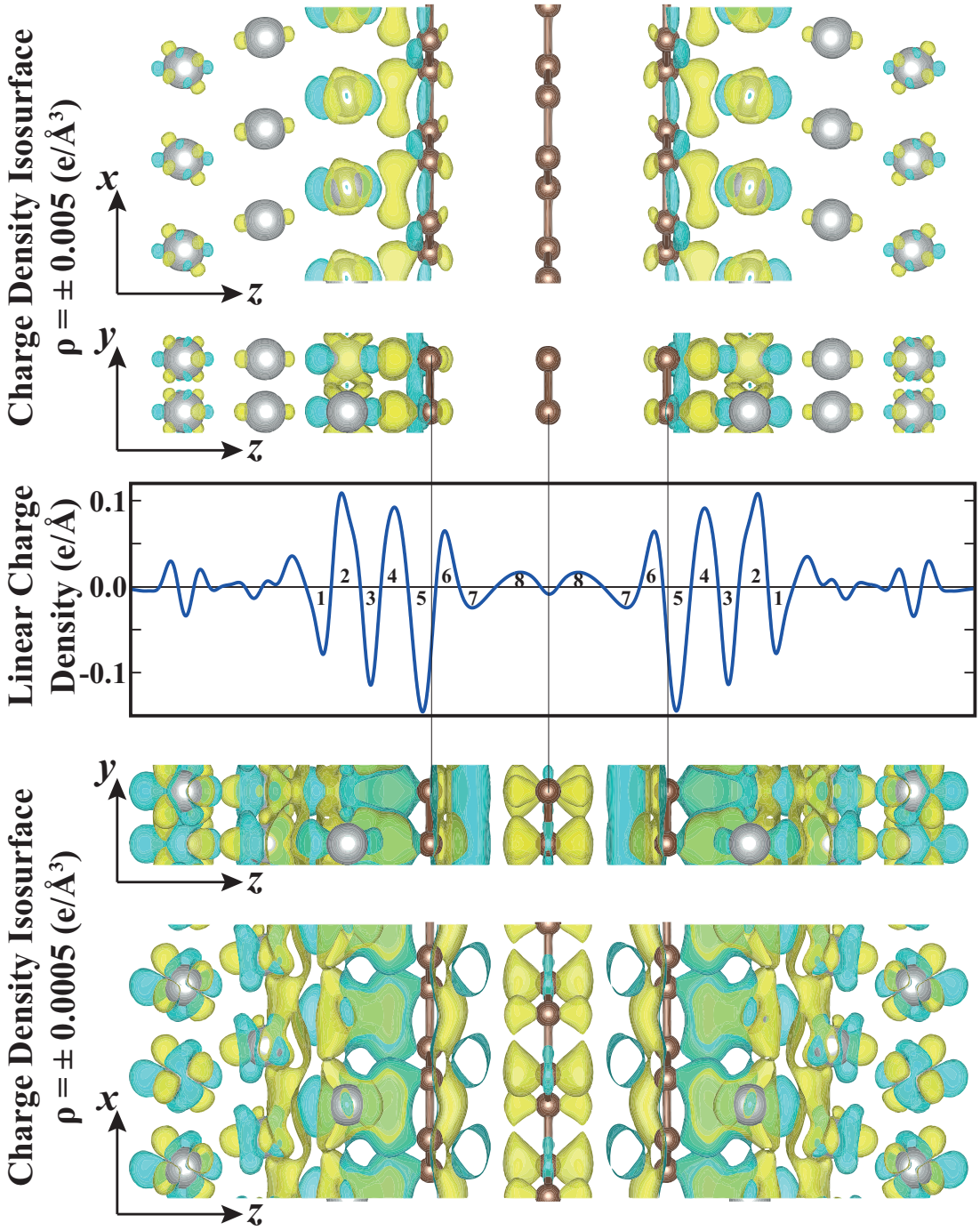

Figure 6.5: Isosurfaces and variation of linear density of charge density difference along z-axis. The difference charge density is obtained by subtracting the charge densities of Ni slabs and ABA structures from the charge density of Ni-ABA-Ni structure at $\sim$ 6 GPa. Yellow (blue) isosurface plots correspond to the charge density accumulation (depletion). Specific regions of depletion and accumulation is denoted by numerals on the linear density of charge density difference plot.

by Fig. 6.4 (a) heralds another important effect.

To explain these trends we first examine the effect of Ni slabs on the electronic structure of graphene layers. The self-consistent difference charge density $\Delta\rho$, is obtained by subtracting the charge density of ABA structure and two Ni(111) slabs from that of Ni-ABC-Ni structure. The isosurfaces of $\Delta\rho$ and the variation of its value averaged over (x, y)-planes parallel to graphene layers (called linear density) are presented in Fig. 6.5. The major charge transfer is between Ni and graphene layers attached to each other as seen in top and middle panels of Fig. 6.5. The dangling Ni-d_{z^2} orbitals at the surface of the slab change their character upon coating of graphene layers. This is resulted in the charge depletion denoted by the numerals 1 and 3 in the linear charge density plot. Analysis of the band structure show significant contribution to C-p_z states from s, d_{xz} and d_{yz} orbitals of Ni atoms, while C-p_z orbitals by themselves contribute to d_{xy} and d_{x^2} states of Ni atoms. As a result of these complex mechanism of charge transfer the charge density around the graphene layer is shifted towards Ni slab resulting in charge density accumulations (depletions) denoted by numerals 4 and 6 (5 and 7).

The charge density depletion denoted by numeral 7 in the linear density of charge difference may be the key feature to explain the decrease in the corrugation strength between graphene layers due to Ni slabs. The isosurface of charge depletion corresponding to this region can be seen in the bottom panel of Fig. 6.5. This charge depletion lowers the chemical interaction between graphene layers and results in lowering of corrugation strength as seen in Fig. 6.3 and Fig. 6.4. Moreover, similar charge depletions are also observed in Ni-AB-Ni, Ni-ABCA-Ni and Ni-ABCBA-Ni structures and their amplitude asymptotically increases by going from two to five layers. This is in accordance with the decrease in the corrugation strength with increasing number of layers, shown in Fig. 6.4(b).

In conclusion, we find that even in the present model, where graphene layers have negligible puckering, the corrugation strength is decreased upon coating of the sliding Ni surfaces and increasing the number of layers. This is attributed to a complex charge transfer between graphene layers and Ni(111) surfaces, each coated by these graphenes. This transfer results in charge depletion between

graphene layers thereby decreasing the corrugation strength. In the absence of Ni slabs each coated by a graphene layer, the corrugation strength is relatively higher and practically independent of the number of graphene layers. Our results demonstrate that graphene attached to sliding surfaces operate as superlubricant by suppressing energy dissipation dramatically.

Chapter 7

Outlook

In this thesis, the frictional and vibrational properties of various nanostructures were investigated. Interesting physics arising in low-dimensional materials ranging from 2D graphene-like honeycomb structures to quasi-1D nanoribbons and 1D atomic chains were explored. Vibrational properties of these materials were investigated using the state-of-the-art phonon dispersion calculations within the density functional theory. To explore the frictional properties of layered nanostructures like molybdenum disulfide, a new method for calculation of corrugation potential under constant loading force was introduced.

A stringent theoretical evidence for stability of 2D honeycomb structure of Si atoms called silicene was provided. It was shown that, silicene acquires stability through puckering which still preserves the linearly crossing bands at the Fermi level, despite the lowered symmetry. Silicene is expected to become an important material for future electronics because of its similarity to graphene and its convenience in silicon dominated industry. Much recently, silicene was epitaxially grown on silver substrate. The structural and electronic properties reported by this experiment is in a very good agreement with our predictions.

The armchair nanoribbons of silicon and germanium honeycomb structures were also found stable with electronic properties similar to that of graphene nanoribbons like family behaviour in the variation of band gap with respect to

their width. The phonon dispersion calculations revealed the fourth acoustical mode of the nanoribbons which is a unique property of quasi-1D nanostructures.

The stability analyses of carbon atomic chains have revealed new physics arising in these 1D nanostructures having fundamental importance. The interactions between carbon atoms were found to extend to very long distances over the chain. These long-ranged forces have $1/r$ decay rate with oscillatory behavior. The origins of this phenomena was explained in the framework of Friedel oscillations. This also explained why similar interactions are observed in BN atomic chains but not in B or Al atomic chains.

To understand fundamental processes involved in friction between nanostructures, basic mechanisms of dissipation were outlined. The importance of sudden processes in generation of nonequilibrium phononic states were highlighted. Transition between different regimes of friction were analysed by simple models.

A new method for calculation of intrinsic stiffness and corrugation potential of layered lubricants under constant loading pressure was developed. Frictional figure of merit, which is a material property corresponding to the ratio between the stiffness and critical curvature derived from corrugation potential, was introduced as a quantitative measure of frictional properties. Using this measure it was shown that, tungsten oxide can outperform molybdenum disulfide structure, which is frequently used as a lubricant in industrial applications. Another advantage of tungsten oxide is its resistance to oxidation, which is the main problem faced in superlubricants like hydrogenated diamond like carbon films.

Finally, the frictional properties of Ni slabs having graphene layers in between have been investigated. It was shown that, to enter the continuous sliding regime at least two graphene layers should be used. The corrugation strength between Ni slabs is found to be decreased as the number of graphene layers are increased. This trend is not present in structures composed of only graphene layers. The observed trends are explained in terms of charge transfer between graphene layers and Ni slabs.

Bibliography

[1] P. Hohenberg and W. Kohn, Phys. Rev. **136**, B864 (1964).

[2] W. Kohn and L. J. Sham, Phys. Rev. **140**, A1133 (1965).

[3] K. S. Novoselov, A. K. Geim, S. V. Morozov, D. Jiang, Y. Zhang, S. V. Dubonos, I. V. Grigorieva, A. A. Firsov, Science **306**, 666 (2004).

[4] K. S. Novoselov, A. K. Geim, S. V. Morozov, D. Jiang, M. I. Katsnelson, I. V. Grigorieva, S. V. Dubonos, A. A. Firsov, Nature **438**, 197 (2005).

[5] G. Binnig, H. Rohrer, Ch. Gerber, and E. Weibel, Phys. Rev. Lett. **49**, 57 (1982).

[6] G. Binnig, C. F. Quate, and Ch. Gerber Phys. Rev. Lett. **56**, 930 (1986).

[7] E. Schrödinger, Phys. Rev. **28**, 1049 (1926).

[8] D. R. Hartree, Proc. Cambridge. Philos. Soc. **24**, 89 (1928).

[9] J. C. Slater, Phys. Rev. **35**, 210 (1930).

[10] V. Fock, Z. Phys. **61**, 126 (1930).

[11] L. H. Thomas, Proc. Cambridge. Philos. Soc. **23**, 542 (1927).

[12] E. Fermi, Z. Phys. **48**, 73 (1928).

[13] R. O. Jones and O. Gunnarson, Rev. Mod. Phys. **61**, 689 (1989).

[14] J. P. Perdew and Y. Wang, Phys. Rev. B, **45**, 13244 (1991).

[15] H.J. Monkhorst and J.D. Pack, Phys. Rev. B**13**, 5188, (1976).

[16] D. Vanderbilt, Phys. Rev. B **41**, 7892 (1990).

[17] G. Kresse and D. Joubert, Phys. Rev. B **59**, 1758 (1999).

[18] G. Kresse and J. Hafner, Phys. Rev. B **47**, 558 (1993).

[19] G. Kresse and J. Furthmuller, Phys. Rev. B **54**, 11169 (1996).

[20] B. N. J. Persson, *Sliding Friction: Physical Principles and Applications* (Springer, Berlin, 1998).

[21] L. da Vinci, *Codex Atlanticus*, Biblioteca Ambrosiana, Milan (1478).

[22] G. A. Coulomb. *Théorie des machines simples, en ayant égard au frotemant de leurs parties, et a la roideur des cordages*, Mem. Math. Phys., 161 Paris (1785).

[23] D. Dowson, *History of Tribology* (Longman, New York, 1979).

[24] L. Prandtl, Z. Angew. Math. Mech. **8**, 85 (1928).

[25] G. A. Tomlinson, Philos. Mag., **7**, 905 (1929).

[26] F. P. Bowden and D. Tabor *Friction and lubrication* (Methuen, London, 1967).

[27] J. A. Greenwood, *Fundamentals of Friction: Macroscopic and Microscopic Processes* (Kluwer, Dordrecht, 1992).

[28] G. Binnig, H. Rohrer, Ch. Gerber, and E. Weibel, Phys. Rev. Lett. **50**, 120 (1983).

[29] M. Urbakh and E. Meyer, Nature Mat. **9**, 8 (2010).

[30] C. M. Mate, G. M. McClelland, R. Erlandsson, and S. Chiang , Phys. Rev. Lett. **59**, 1942 (1987).

[31] D. Tomanék, W. Zhong, and H. Thomas, Europhys. Lett. **15**, 887 (1991).

[32] A. Socoliuc, R. Bennewitz, E. Gnecco, and E. Meyer, Phys. Rev. Lett. **92**, 134301 (2004).

[33] S. Cahangirov, C. Ataca, M. Topsakal, H. Şahin, and S. Ciraci, Phys. Rev. Lett. **108**, 126103 (2012).

[34] H. Yoshizawa, P. McGuiggan and J. Israelachvili, Science **259**, 1305 (1993).

[35] B. N. J. Persson, Surf. Sci. Reports **33**, 83 (1999).

[36] R. E. Peierls, Ann. I. H. Poincare **5**, 177 (1935).

[37] L. D. Landau, Phys. Z. Sowjetunion **11**, 26 (1937).

[38] C. Lee, X. Wei, J. W. Kysar, and J. Hone, Science **321**, 385 (2008).

[39] K. Saito, J. Nakamura, and A. Natori, Phys. Rev. B **76**, 115409 (2007).

[40] P. R. Wallace, Phys. Rev. **71**, 622 (1947).

[41] P. Avouris, Z. Chen, and V. Perebeinos, Nature Nanotech. **2**, 605 (2007).

[42] O. Klein, Zeitschrift für Physik **53**, 157 (1929).

[43] M. I. Katsnelson, K. S. Novoselov, and A. K. Geim, Nature Phys. **2**, 620 (2006).

[44] S. Cahangirov, E. Aktürk, M. Topsakal, H. Şahin and S. Ciraci, Phys. Rev. Lett. **102**, 236804 (2009).

[45] P. Vogt, P. De Padova, C. Quaresima, J. Avila, E. Frantzeskakis, M. C. Asensio, A. Resta, B. Ealet, and G. Le Lay, Phys. Rev. Lett. **108**, 155501 (2012).

[46] H. Şahin, S. Cahangirov, M. Topsakal, E. Bekaroglu, E. Aktürk, R. T. Senger, and S. Ciraci, Phys. Rev. B **80**, 155453 (2009).

[47] M. Y. Han, B. Özyilmaz, Y. Zhang, and P. Kim, Phys. Rev. Lett. **98**, 206805 (2007).

[48] X. Wang, Y. Ouyang, X. Li, H. Wang, J. Guo, and H. Dai, Phys. Rev. Lett. **100**, 206803 (2008).

[49] Y-W. Son, M. L. Cohen, and S. G. Louie, Nature **444**, 347 (2006).

[50] Y-W. Son, M. L. Cohen, and S. G. Louie, Phys. Rev. Lett. **97**, 216803 (2006).

[51] S. Cahangirov, M. Topsakal, and S. Ciraci, Phys. Rev. B **81**, 195120 (2010).

[52] A. D. OConnell, M. Hofheinz, M. Ansmann, R. C. Bialczak, M. Lenander, E. Lucero, M. Neeley, D. Sank, H. Wang, M. Weides, J. Wenner, J. M. Martinis, and A. N. Cleland, Nature **464**, 697 (2010).

[53] V. L. Gurevich, *Transport in phonon systems* (North-Holland, Amsterdam, 1986).

[54] C. Kittel, *Introduction to Solid State Physics* (John Wiley & Sons, New Jersey, 1996).

[55] D. Alfé, Comput. Phys. Commun. 180, 2622 (2009).

[56] O. Dubay and G. Kresse, Phys. Rev. B **67**, 035401 (2003).

[57] Y. Zhang, Y.-W. Tan, H. L. Stormer, and P. Kim, Nature **438**, 201 (2005).

[58] C. Berger, Z. Song, X. Li, X. Wu, N. Brown, C. Naud, D. Mayou, T. Li, J. Hass, A. N. Marchenkov, E. H. Conrad, P. N. First, and W. A. de Heer, Science **312**, 1191 (2006).

[59] A.K. Geim and K.S. Novoselov, Nature Materials, **6**, 183 (2007).

[60] K. Takeda and K. Shiraishi, Phys. Rev. B **50**, 14916 (1994).

[61] M. Zhang, Y. H. Kan, Q. J. Zang, Z. M. Su, and R. S. Wang, Chem. Phys. Lett. **379**, 81 (2003).

[62] E. Durgun, S. Tongay and S. Ciraci, Phys. Rev. B **72**, 075420 (2005).

[63] P. Sen, S. Ciraci, A. Buldum, and I. P. Batra, Phys. Rev. B **64**, 195420 (2001).

[64] R. T. Senger, S. Tongay, E. Durgun, and S. Ciraci, Phys. Rev. B **72**, 075419 (2005).

[65] S. Tongay, R. T. Senger, S. Dag, and S. Ciraci, Phys. Rev. Lett. **93**, 136404 (2004).

[66] D. M. Ceperley and B. J. Alder, Phys. Rev. Lett. **45**, 566, (1980).

[67] P. E. Blochl, Phys. Rev. B **50**, 17953 (1994).

[68] H. Nakano, T. Mitsuoka, M. Harada, K. Horibuchi, H. Nozaki, N. Takahashi, T. Nonaka, Y. Seno, and H. Nakamura, Angew. Chem. **118**, 6451 (2006).

[69] C. Lèandri, G. Le Lay, B. Aufray, C. Girardeaux, J. Avila, M.E. Dàvila, M.C. Asensio, C. Ottaviani, A. Cricenti, Surf. Sci. Lett. **574**, L9 (2005).

[70] C. Lèandri, H. Oughaddou, B. Aufray, J.M. Gay, G. Le Lay, A. Ranguis, Y. Garreau, Surf. Sci. **601**, 262 (2007);

[71] P. De Padova, C. Quaresima, P. Perfetti, B. Olivieri, C. Lèandri, B. Aufray, S. Vizzini, and G. Le Lay, Nano Lett. **8**, 271 (2008);

[72] P. De Padova, C. Lèandri, S. Vizzini, C. Quaresima, P. Perfetti, B. Olivieri, H. Oughaddou, B. Aufray, and G. Le Lay, Nano Lett. **8**, 2299 (2008);

[73] A. Kara, C. Lèandri, M. E. Dàvila, P. De Padova, B. Ealet, H. Oughaddou, B. Aufray and G. Le Lay, J. Supercond. Nov. Magn., **22**, 259 (2009);

[74] G. Le Lay, B. Aufray, C. Lèandri, H. Oughaddou, J. P. Biberian, P. De Padova, M. E. Dàvila, B. Ealet, A. Kara, Applied Surface Science, **256**, 524 (2009).

[75] A. Kara, S. Vizzini, C. Lèandri, B. Ealet, H. Oughaddou, B. Aufray, and G. Le Lay, J. Phys. Condens. Matter **22**, 045004 (2010).

[76] G. Kresse, J. Furthmuller and J. Hafner, Europhys. Lett. **32**, 729 (1995).

[77] A. De Martino and R. Egger, Phys. Rev. B **67**, 235418 (2003).

[78] M. Topsakal, S. Cahangirov, E. Bekaroglu, and S. Ciraci Phys. Rev. B **80**, 235119 (2009).

[79] E. J. Bylaska, J. H. Weare, and R. Kawai, Phys. Rev. B **58**, R7488 (1998).

[80] A. Abdurahman, A. Shukla, M. Dolg, Phys. Rev. B **65**, 115106 (2002).

[81] S. Tongay, R. T. Senger, S. Dag, and S. Ciraci, Phys. Rev. Lett. **93**, 136404 (2004).

[82] S. Tongay, S. Dag, E. Durgun, R. T. Senger, and S. Ciraci, J. Phys. Cond. Matt. **17**, 3823 (2005).

[83] S. Dag, S. Tongay, T. Yildirim, R. T. Senger, C. Y. Fong, and S. Ciraci, Phys. Rev. B **72**, 155444 (2005).

[84] R. E. Peierls, *Quantum Theory of Solids* (Oxford University Press, New York, 1955), p. 108.

[85] J. Heyd, G. E. Scuseria and M. Ernzerhof, J. Chem. Phys. **118**, 8207 (2003).

[86] J. Paier, M. Marsman, K. Hummer, G. Kresse, I. C. Gerber and J. G. Ángyán, J. Chem. Phys. **124**, 154709 (2006); **125**, 249901(E) (2006).

[87] J. Paier, M. Marsman, and G. Kresse, J. Chem. Phys. **127**, 024103 (2007).

[88] T. Pino, H. Ding, F. Guthe, and J. P. Maier, J. Chem. Phys. **114**, 2208 (2001).

[89] S. Eisler, A. D. Slepkov, E. Elliott, T. Luu, R. McDonald, F. A. Hegmann, and R. R. Tykwinski, J. Am. Chem. Soc. **127**, 2666 (2005).

[90] X. Gu, R. I. Kaiser, and A. M. Mebel, Chem. Phys. Chem. **9**, 350 (2008).

[91] S. Hino, Y. Okada, K. Iwasaki, M. Kijima, and H. Shirakawa, Chem. Phys. Lett. **372**, 59 (2003).

[92] C. H. Jin, H. P. Lan, L. M. Peng, K. Suenaga, and S. Iijima, Phys. Rev. Lett. **102**, 205501 (2009).

[93] M. Topsakal and S. Ciraci, Phys. Rev. B **81**, 024107 (2010).

[94] W. A. Chalifoux and R. R. Tykwinski, Nature Chem. **2**, 967 (2010).

[95] J. Friedel, Phil. Mag. **43**, 153 (1952).

[96] G. F. Giuliani and G. Vignale, *Quantum Theory of the Electron Liquid* (Cambridge University Press, Cambridge, England, 2005).

[97] Á. Bácsi and A. Virosztek, Phys. Rev. B **82**, 193405 (2010).

[98] I. Grosu and L. Tugulan, J. Supercond. Nov. Magn. **21**, 65 (2008).

[99] G.F. Giuliani, G.Vignale, T. Datta, Phys. Rev. B **72**, 033411 (2005).

[100] P. Langevin, C. R. Acad. Sci. **146**, 530 (1908).

[101] R. Kubo, Rep. Prog. Phys. **29**, 255 (1966).

[102] B. N. J. Persson and R. Rydberg, Phys. Rev. B **32**, 3586 (1985).

[103] A. Einstein, Annalen der Physik **17**, 549 (1905).

[104] R. J. Cannara, M. J. Brukman, K. Cimatu, A. V. Sumant, S. Baldelli, and R. W. Carpick, Science **318**, 780 (2007).

[105] T. Filleter, J. L. McChesney, A. Bostwick, E. Rotenberg, K.V. Emtsev, Th. Seyller, K. Horn, and R. Bennewitz, Phys. Rev. Lett. **102**, 086102 (2009).

[106] C. Lee, Q. Li, W. Kalb, X. Liu, H. Berger, R. W. Carpick, and J. Hone, Science **328**, 76 (2010).

[107] B. N. J. Persson, Phys. Rev. B **44**, 3277 (1991).

[108] G. Wedler, H. Reichenberger, and H. Wenzel, Z. Naturforsch. **26a**, 1444 (1971).

[109] J. Y. Park, D. F. Ogletree, P. A. Thiel, and M. Salmeron, Science **313**, 186 (2006).

[110] M. H. Mueser, M. Urbakh, and M. O. Robbins, Advances in Chem. Phys. **126**, 187 (2003).

[111] Y. I. Frenkel and T. Kontorova, Zh. Eksp. Teor. Fiz. **8**, 1340 (1938).

[112] O. M. Braun and Y. S. Kivshar, *The Frenkel-Kontorova Model: Concepts, Methods, and Applications* (Springer, Berlin, 2004).

[113] M. Weiss and F. J. Elmer, Phys. Rev. B **53**, 7539 (1996).

[114] M. Weiss and F. J. Elmer, Zeitschrift Fur Physik B-Condensed Matter **104**, 55 (1997).

[115] J. Röder, J. E. Hammerberg, B. L. Holian and A. R. Bishop, Phys. Rev. B **57**, 2759 (1998).

[116] J. B. Sokoloff, Surf. Sci. **144**, 267 (1984); Phys. Rev. B **42**, 760 (1990).

[117] A. Buldum and S. Ciraci, Phys. Rev. B **55**, 2606 (1997).

[118] A. Buldum, D.M. Leitner and S. Ciraci, Phys. Rev. B **59**, 16042 (1999).

[119] H. Sevincli, S. Mukhopadhyay, R. T. Senger, and S. Ciraci, Phys. Rev. B **76**, 205430 (2007).

[120] E. Gnecco, R. Bennewitz, T. Gyalog, Ch. Loppacher, M. Bammerlin, E. Meyer, and H.-J. Gntherodt, Phys. Rev. Lett. **84**, 1172 (2000).

[121] D. C. Elias, R. R. Nair, T. M. G. Mohiuddin, S. V. Morozov, P. Blake, M. P. Halsall, A. C. Ferrari, D. W. Boukhvalov, M. I. Katsnelson, A. K. Geim, and K. S. Novoselov, Science **323**, 610 (2009).

[122] H. Şahin, C. Ataca, and S. Ciraci, Phys. Rev. B **81**, 205417 (2010).

[123] R. R. Nair, W. Ren, R. Jalil, I. Riaz, V. G. Kravets, L. Britnell, P. Blake, F. Schedin, A. S. Mayorov, S. Yuan, M. I. Katsnelson, H.-M. Cheng, W. Strupinski, L. G. Bulusheva, A. V. Okotrub, I. V. Grigorieva, A. N. Grigorenko, K. S. Novoselov, and A. K. Geim, Small **6**, 2877 (2010).

[124] H. Şahin, M. Topsakal, and S. Ciraci, Phys. Rev. B **83**, 115432 (2011).

[125] C. Ataca, M. Topsakal, E. Aktürk, and S. Ciraci, J. Phys. Chem. C **115**, 16354 (2011).

[126] C. Ataca, H. Sahin, E. Aktürk, and S. Ciraci, J. Phys. Chem. C **116**, 8983 (2011).

[127] M. Topsakal, S. Cahangirov, and S. Ciraci, App. Phys. Lett. **96**, 091912 (2010).

[128] S. Miyake, R. Kaneko, Y. Kikuya, I. Sugimoto, J. Tribol. **113**, 384 (1991).

[129] P. Thomas, K. Delbe, D. Himmel, J. L. Mansot, F. Cadore, K. Guerin, M. Dubois, C. Delabarre, A. Hamwi, J. Phys. Chem. Solids **67**, 1095 (2006).

[130] J. M. Martin, C. Donnet, Th. Le Mogne, and Th. Epicier, Phys. Rev. B **48**, 10583 (1993).

[131] T. Liang, W. G. Sawyer, S. S. Perry, S. B. Sinnott, and S. R. Phillpot, Phys. Rev. B **77**, 104105 (2008).

[132] S. Chen, L. Brown, M. Levendorf, W. Cai, S.-Y. Ju, J. Edgeworth, X. Li, C. W. Magnuson, A. Velamakanni, R. D. Piner, J. Kang, J. Park, and R. S. Ruoff, ACS Nano **5**, 1321 (2011).

[133] J. P. Perdew, K. Burke, and M. Ernzerhof, Phys. Rev. Lett. **77**, 3865 (1996).

[134] S. Grimme, J. Comp. Chem. **27**, 1787 (2006).

[135] L. C. Lew Yan Voon, E. Sandberg, R. S. Aga, A. A. Farajian, Appl. Phys. Lett. **97**, 163114 (2010).

[136] M. Houssa, E. Scalise, K. Sankaran, G. Pourtois, V. V. Afanas'ev, and A. Stesmans, Appl. Phys. Lett. **98**, 223107 (2011).

[137] A. Erdemir, Surface and Coatings Technology **146**, 292 (2001).

[138] M. Dienwiebel, G. S. Verhoeven, N. Pradeep, and J. W. M. Frenken, Phys. Rev. Lett. **92**, 126101 (2004).

[139] J. S. Choi, J. S. Kim, I. S. Byun, D. H. Lee, M. J. Lee, B. H. Park, C. Lee, D. Yoon, H. Cheong, K. H. Lee, Y. W. Son, J. Y. Park, and M. Salmeron, Science **333**, 607 (2011)

[140] A. E. Filippov, M. Dienwiebel, J. W. M. Frenken, J. Klafter, and M. Urbakh, Phys. Rev. Lett. **100**, 046102 (2008).

[141] A. S. de Wijn, C. Fusco, and A. Fasolino, Phys. Rev. E **81**, 046105 (2010).

[142] I. V. Lebedeva, A. A. Knizhnik, A. M. Popov, O. V. Ershova, Y. E. Lozovik, and B. V. Potapkin, Phys. Rev. B **82**, 155460 (2010).

[143] A. M. Popov, I. V. Lebedeva, A. A. Knizhnik, Y. E. Lozovik, and B. V. Potapkin, Phys. Rev. B **84**, 045404 (2011).

[144] H. Lee, N. Lee, Y. Seo, J. Eom and S. W. Lee, Nanotechnology **20**, 325701 (2009).

[145] T. Filleter, J. L. McChesney, A. Bostwick, E. Rotenberg, K.V. Emtsev, Th. Seyller, K. Horn, and R. Bennewitz, Phys. Rev. Lett. **102**, 086102 (2009).

[146] C. Lee, Q. Li, W. Kalb, X. Z. Liu, H. Berger, R. W. Carpick, and J. Hone, Science **328**, 76 (2010).